^{88}Sr^{+} ion trapping techniques and technologies for quantum information processing

Thesis submitted in partial fulfilment
of the requirements of the degree of
Doctor of Philosophy
of
Imperial College London

Michael Brownnutt

Imperial College London

Experimental work carried out at the
National Physical Laboratory

September 2007

Declaration

I declare that this thesis and the work presented within it are my own work except where explicitly stated or referenced otherwise in the text.

....

September 21, 2007

Michael Brownnutt

Abstract

This thesis describes techniques used in trapping and cooling a single $^{88}\mathrm{Sr}^+$ ion. It also presents the development of a novel technological approach for fabricating a scalable trapped-ion quantum information processor.

A single $^{88}\mathrm{Sr}^+$ ion is loaded into a radio-frequency endcap trap. To facilitate this a clean, efficient method of photoionising Sr via a two-step resonant process has been developed, using all diode-based laser systems. This method of trap loading is quantitatively compared to the previously-used electron-bombardment loading method, and shown to reduce the Sr vapour pressure required to load by four orders of magnitude. It also provides more than an order of magnitude reduction in the day-to-day variation of the voltages required to compensate micromotion.

A single trapped $^{88}\mathrm{Sr}^+$ ion is then cooled to the zero point of its axial motion. A ground-state occupation probability of 98.6(8)% was achieved using resolved-sideband laser cooling on the 674 nm $^2\mathrm{S}_{1/2}$–$^2\mathrm{D}_{5/2}$ quadrupole transition. The ion's heating rate was measured to be 0.054(4) quanta/ms, implying a spectral density of electric-field noise comparable to the other values reported in the literature.

Finally a design for a novel microfabricated ion trap is proposed. By using a process based on planar silica-on-silicon techniques, the trap electrodes are made of gold-coated silica and are spaced by highly-doped silicon in a monolithic structure. The trapping potential is modelled and the operating parameters required to achieve experimentally useful motional frequencies are calculated. Practical concerns—including RF heating of the substrate, and electrical- and mechanical- breakdown—are investigated and are not expected to limit the operation of the trap. Progress towards the fabrication of such a trap is also presented.

Acknowledgements

Before starting at NPL I was told, in no uncertain terms, that Alastair Sinclair was an excellent experimentalist who would go to great lengths to instil rigour and quality into my work, and from whom I could learn much. I have not been disappointed. Thank you, Alastair. You have made this Ph.D. all that it was [1 Thes 5:12-13]. Thanks is also due to my predecessor, Valliappan Letchumanan, with whom I worked during my first year, who taught me a lot, and who passed on *The Monastic Rules.* For the last few years it has been a pleasure to work with Guido Wilpers, whom I thank for his time, his attention to detail, and his cocktail stick. I must also thank Patrick Gill for giving me the opportunity to work in such an establishment as NPL.

At Imperial, Richard Thompson has provided tremendous support on academic issues, non-academic issues, and a whole variety of things that fall in between. I am indebted to you [Prov 15:22-23].

At NPL it is right to acknowledge the support of the wider team with whom I have worked, particularly the late Dick Rowley, for his knowledge of electronics and heatsinks, and his willingness to pass such knowledge on. Also Stephen Webster for general input on lasers, cavities and the cricket; Geoff Barwood, for his eternal, unique optimism; and Thomas Byrne, always helpful.

Beyond the walls of NPL there stand family and friends who require recognition for their invaluable contributions that support this work. Phil: you helped keep me sane. Thanks for the bivy trips [Prov 13:20]. Jen:

thanks for the years of friendship, even when it was tricky. And thanks for being able to spell [Lk 1:45]. Chris, Andy, James: for the years in Barnes. I never took your advice, but it was reassuring to know that the advice existed [Job 26:3]. To the many inhabitants of Kenway Road: your friendship has been incomparable. I thank you all [Prov 6:22].

Wes and Faye: thanks for your council, insight, love and hospitality. You have given me a lot [1 Pet 4:8-11]. Frans and Debs: of all I have learned in the last 8 years, the things you have taught me are most important. It has been an honour walking with you [Heb 12:10-11]. Mum and Dad: the guys responsible for so much of me, in so many ways. Thank you for showing me how to walk [2 Chron 34:2]. 若婷，你教懂了我房屋錢財是祖宗所遺留的。我很感謝你的耐心和鼓勵。神將會繼續塑造你成為他所設計的。我為你因此而得來的喜樂心懷感激。 Finally, to the mentor, co-worker, councillor, friend, parent and lover who tops the lot. The One who makes it all worth doing: Thank You [Eccl 12:12-13].

Contents

List of Figures

List of Tables

CHAPTER 1

Introduction

Quantum systems can simultaneously exist in two states which would be classically mutually exclusive. One of the most famous thought experiments to illustrate this is that of Schrödinger's Cat, in which a cat is simultaneously alive and dead. Quantum systems also have the property that such "superposition" states can be dependent on—entangled with—other superposition states. In Schrödinger's case a vial of poison is both broken and unbroken, *and* perfectly correlated with the cat being dead and alive. Such complexity means that quantum systems can rapidly become too difficult to model on a classical computer.

In 1982 Richard Feynman pointed out that while a computer using classical bits of information could not keep up with such involved behaviour, a quantum computer, using quantum bits (qubits), could utilise that very behaviour to efficiently simulate another quantum system [1]. A quantum computer can thus be seen to be capable of performing calculations that a classical computer cannot. This left the realm of a mere scientific curiosity when, in 1994, Peter Shor observed that one such computation is that of efficient factorisation [2]. This is significant, as the difficulty of factorising large numbers is the basis of much modern cryptography [3]; if a quantum computer can be realised physically, such cryptographic systems could be compromised. Several further algorithms have also been proposed and implemented which can carry out calculations more efficiently than their classical counterparts. Notable among these are the Deutsch-Jozsa algorithm [4, 5] which evaluates whether or not a function is balanced, and Grover's search algorithm [6] which can search unsorted databases quadratically faster than a classical search. Mechanisms for dealing with errors and imperfections in the manipulation of quantum states have also been proposed [7, 8] to allow fault-tolerant computing. Beyond computing specifically, quantum states can be manipulated to allow new or improved processes to be carried out, including teleportation of quantum states [9], and unconditionally secure cryptography [10]. Finally, quantum correlations between particles can allow additional precision in metrological applications [11]. All of these processes are collectively termed quantum information processing and communication (QIPC).

There is a variety of physical systems in which a quantum computer might be realised. Much progress was initially made using nuclear magnetic resonance (NMR) techniques, and even Shor's algorithm has been realised for small numbers (factorising the number 15, on a 7-qubit register) [12]. There are, however, significant problems with scaling the processes involved to large numbers of qubits [13]. The very small energy level spacings involved ($\lesssim \mu$eV) mean that the system cannot practically be initialised by cooling to the ground state. Instead a "pseudo-pure" ground state is used, where only a fraction of the qubits are in the correct state, and then the incorrect answers are averaged out by measuring a bulk system. Unfortunately, the amplitude of the averaged "correct" signal decreases exponentially with the number of qubits, thereby negating the potential speed-up of a quantum system. Other possible candidate systems include [14]: photons, cavity QED, solid-state systems, neutral atoms, and ion traps. Currently ion traps offer one of the most promising systems for realising a scalable quantum computer [15–17]. It is such systems which are of interest to the work at hand: the methods and technologies developed in this thesis work are directly applicable to the further development of trapped-ion quantum computing.

Shor's full algorithm has yet to be realised with trapped-ion systems, though steps have been taken towards realising parts of it [18, 19]. Several algorithms have been realised, however, including the Deutsch-Jozsa algorithm [20], Grover's search algorithm [21], and error correction [22]. Deterministic teleportation of the quantum state of an atom has also been demonstrated [23, 24]. Following Feynman's original line of thinking, work has also been carried out into using trapped ions to simulate the behaviour of other quantum systems [25]. Of particular interest to metrological institutes, such as the National Physical Laboratory (NPL), is quantum-enhanced metrology in trapped-ion systems. In this kind of metrology, entanglement of the particles being measured allows a measurement precision which is not possible using classical means. For example the entanglement of particles' spins allows the spin rotation angle to be measured with enhanced precision, which can be used to increase the precision of Ramsey spectroscopy experiments [26]. Three [27] and six [28] particle entangled states have also been produced and demonstrated to allow spectroscopic measurements with better signal-to-noise than classically possible. While each of the operations listed above can out-perform a classical computer of the same sized register, they have not been experimentally demonstrated for more than a few qubits; the state of the art stands at entangled states of only six [28] or eight [29] ions. To become useful, systems must be extended to many, many qubits.

While Schrödinger's cat provides an interesting thought experiment, its very strangeness illustrates the fact that quantum states are not generally observed in macroscopic systems; quantum systems do not trivially scale up. In order to achieve a quantum computer in practice, certain stringent requirements must be met [30]. These are called the DiVincenzo Criteria and are now outlined, with the salient features for ion traps being discussed.

1) *A scalable physical system with well-characterised qubits.*

   Even within the field of trapped-ion quantum computing, there is a number of ways to realise an good approximation to the ideal two-level system required for a qubit [15]. These include: two hyperfine components of an ion's electronic ground state; the electronic ground state and a metastable excited state of an ion; and two states of a trapped ion's quantised motion. The system considered in this thesis is a trapped $^{88}\mathrm{Sr}^{+}$ ion, and utilises the second and third of these qubits; specifically the optical quadrupole $^{2}\mathrm{S}_{1/2}$–$^{2}\mathrm{D}_{5/2}$ transition; and the transition between the motional ground state ($n = 0$) and the first excited state ($n = 1$). Such qubits (here in $^{88}\mathrm{Sr}^{+}$ and elsewhere in $^{40}\mathrm{Ca}^{+}$) are well characterised [31–33]. The significant outstanding challenge is that of making the system scalable to larger numbers of qubits.

There are several proposed ways to scale processing from a single ion to many (thousands of) ions. These include arrays of microtraps where ions are moved between different trap segments [34], or where a single "head" ion carries quantum information between traps [35]; coupling ions via photons [36–38]; and using hybrid trapped-ion / solid-state systems [39]. A geometry which could in principle realise the first of these proposals for a scalable architecture—specifically a silicon-based, segmented microtrap where ions can be moved between segments—is discussed in chapters 6–7.

2) *The ability to initialise the state of the qubits to a simple fiducial state.*

   The qubits used in this experiment consist of two electronic levels and two vibrational levels of a bound $^{88}\text{Sr}^+$ ion. Initialisation of these qubits corresponds to preparing the ion in the ground electronic state, and cooling the ion to its motional ground state respectively. The former is simply achieved by optical pumping. The latter forms the subject of chapter 5.

3) *Long relevant decoherence times, much longer than the gate operation time.*

   For trapped-ion systems, typical gate times are of order a few hundred microseconds, *e.g.* [20, 21, 23, 40, 41]. The natural lifetime for the electronic qubit used in $^{88}\text{Sr}^+$ is 390 ms [31]. To ensure that the decoherence time of the motional qubit is long compared to the gate operation time, the heating rate must be sufficiently small that the vibrational number does not change significantly during an operation. Many factors exist which affect the ion-heating rate [15], and the implementation of techniques to overcome some of these are discussed in chapter 4. A measurement of the heating rate of a single trapped $^{88}\mathrm{Sr}^{+}$ ion is presented in chapter 5.

4) *A universal set of quantum gates.*

   If an arbitrary interaction between any number of qubits can be broken down into a certain set of operations, this set is called "universal". A classical example would be that of a NAND gate: all binary operations can be performed by different combinations of NAND logic gates. Quantum mechanically, all qubit interactions can be decomposed into one-qubit and two-qubit operations [42], and all two-qubit operations can be decomposed into controlled-NOT (C-NOT) operations [43]. It is possible to implement a C-NOT operation using trapped ions [44, 45], and together with single-qubit operations this comprises a universal set of gates.

5) *A qubit specific measurement capability.*

   In the experiment described here, the electronic state of the ion can be measured using Dehmelt's electron shelving technique [46, 47]. When several ions are held in a linear trap, their states can be read out simultaneously by illuminating the entire string with the read-out laser, and imaging the ions onto a charge-coupled device (CCD) camera so that the image of each ion can be spatially resolved [48]. Individual qubit read-out without disturbing the state of neighbouring qubits can be achieved for each ion either by focusing the read-out laser onto different ions, *e.g.* [23, 41, 49], or by moving different ions into the focus of the read-out laser, *e.g.* [19, 22, 24, 50]. The latter method offers greater versatility, and can reduce the amount of stray light seen by non-target ions. This method of addressing will be facilitated by the segmented trap design discussed in chapters 6–7.

This thesis is organised as follows. The theoretical background behind the work presented is laid out in chapter 2. Chapter 3 details the experimental setup required for this work, highlighting the new apparatus which was designed and built. Chapter 4 describes the resonant photoionisation of strontium, and compares the subsequent stability of the ion trap's potential with that of a trap loaded via electron-bombardment ionisation. Cooling of a single $^{88}\mathrm{Sr}^{+}$ ion to the motional ground state is described in chapter 5, along with a measurement of the ion's subsequent heating rate. Chapters 6–7 present the progress towards realising a microfabricated, silicon-based ion trap: chapter 6 details the modelling of the trap structure; chapter 7 outlines the work which has been carried out in cooperation with the Centre for Integrated Photonics (CIP, Ipswich) towards fabricating such a device.

CHAPTER 2

Theoretical background

2.1 Introduction

In the work described in this thesis a Sr atom is photoionised, trapped in a radio-frequency (RF) trap, and cooled to the ground state of its motion. The design of a novel linear RF ion trap is also presented. This chapter outlines some of the background concepts for this work. Specifically, a summary of the electronic structure of strontium (Sr I and Sr II) is given in section 2.2; an overview of the physics of RF traps is given in section 2.3; section 2.4 introduces the principles of laser cooling.

2.2 Energy levels of strontium

Strontium (${}^{88}_{38}\mathrm{Sr}$) is a group II metal situated between ${}_{20}\mathrm{Ca}$ and ${}_{56}\mathrm{Ba}$ in the periodic table. Selected energy levels of Sr I (atomic strontium) are shown in figure 2.1a. The transitions shown are those used in this work to photoionise Sr. The radiation wavelengths associated with these transitions, along with

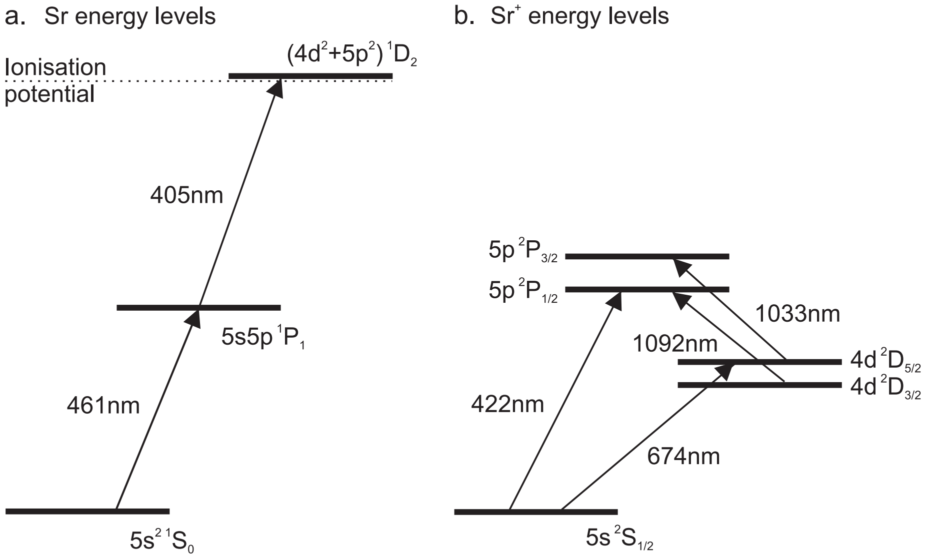

Figure 2.1: (a) Selected energy levels of Sr (Sr I). (b) Lowest lying energy levels of Sr^+ (Sr II). The arrows are labelled with the wavelength of light associated with a particular transition.

transition linewidths, are specified in table 2.1. The ($4\mathrm{d}^2$+$5\mathrm{p}^2$) $^1\mathrm{D}_2$ level is autoionising. This state is doubly excited, so that each excited electron is bound, but their combined energy is greater than the first ionisation potential. From here, one electron returns to the ground state and the other is ejected into the continuum of unbound states above the ionisation potential. The rapidity of this process means that the transition has a broad linewidth. Both the $^1\mathrm{S}_0$—$^1\mathrm{P}_1$ and $^1\mathrm{P}_1$—$^1\mathrm{D}_2$ transitions can be driven using radiations produced by diode-laser-based systems.

Sr^+ has an alkali-like electronic structure, with a single valence electron, and a term scheme which is the same as that of atomic $_{37}\mathrm{Rb}$. The lowest lying energy levels of $^{88}\mathrm{Sr}^+$ are shown in figure 2.1b. The radiation wavelengths and transition linewidths associated with these transitions are listed in table 2.1.

Transition	Wavelength		$\Gamma/2\pi$	$\tau = 1/\Gamma$	
Sr I					
$^1S_0$ — $^1P_1$	460.8620 nm	[51]	32 MHz	5.0 ns	[52]
$^1P_1$ — $^1D_2$	405.2 nm	[53]	260 GHz	0.6 ps	[53]
Sr II					
$^2S_{1/2}$ — $^2P_{1/2}$	421.6706 nm	[51]	20.22 MHz	7.87 ns	[54]
$^2S_{1/2}$ — $^2P_{3/2}$	407.886 nm	[51]	22.77 MHz	6.99 ns	[54]
$^2S_{1/2}$ — $^2D_{3/2}$	687.0066 nm	[51]	0.37 Hz	435 ms	[54]
$^2S_{1/2}$ — $^2D_{5/2}$	674.02559 nm	[55]	0.41 Hz	390 ms	[31]
$^2D_{3/2}$ — $^2P_{1/2}$	1091.7860 nm	[51]	1.52 MHz	105 ns	[54]
$^2D_{5/2}$ — $^2P_{3/2}$	1033.01 nm	[51]	1.38 MHz	115 ns	[54]

Table 2.1: Wavelengths, linewidths and decay times of selected transitions in Sr I and Sr II. A historical summary of measurements of the $^1P_1$—$^1D_2$ transition is given in [56].

All of the interaction wavelengths required can be produced using diode-laser-based systems.

The $^2S_{1/2}$—$^2P_{1/2}$ dipole transition has a 20 MHz linewidth. This means that Doppler cooling to low vibrational quantum numbers is feasible using this transition (as outlined in section 2.4.1). This transition is also used to measure the state of the atom after it has been prepared in a superposition of $^2S_{1/2}$ and $^2D_{5/2}$ states. When illuminated by 422 nm light, an ion in the $^2D_{5/2}$ state remains dark, while an ion initially in the $^2S_{1/2}$ state will cycle on the $^2S_{1/2}$—$^2P_{1/2}$ transition and scatter many photons, which can then be detected. Rather than always returning to the ground state, the $^2P_{1/2}$ state decays to the metastable $^2D_{3/2}$ state with a branching ratio of 1:13. This would prevent efficient cooling on the $^2S_{1/2}$—$^2P_{1/2}$ transition. Radiation at 1092 nm is required to return the ion from the $^2D_{3/2}$ state to the cooling cycle.

The two lowest-lying excited states ($^2D_{3/2}$ and $^2D_{5/2}$) can decay only via dipole-forbidden transitions, and consequently have long lifetimes. The $^2S_{1/2}$—$^2D_{5/2}$ transition is used to realise sub-Doppler cooling of the ion, using a resolved-sideband-cooling method (as outlined in section 2.4.2). To allow many cooling cycles to be performed rapidly on this long-lived transition, radiation at 1033 nm is used to mix the $^2D_{5/2}$ state with the $^2P_{3/2}$ state [57], from where the ion quickly returns to the electronic ground-state. It should be noted that the levels shown in figure 2.1 are somewhat simplified, and each level shown has two or more Zeeman components. These components are degenerate only when the magnetic field is zero, but are non-degenerate in an applied magnetic field.

In addition to being used for ground-state cooling, the long lifetime of the $^2S_{1/2}$—$^2D_{5/2}$ transition makes it a qubit candidate for trapped-ion quantum computing [31, 58]. Quantum gates and algorithms have been proposed which use such long-lived (high-Q) optical transitions [5, 44], and these have been realised using the $^2S_{1/2}$—$^2D_{5/2}$ quadrupole transition in $^{40}Ca^+$ [20, 45], analogous to that in $^{88}Sr^+$.

Throughout this thesis the $^2S_{1/2}$—$^2P_{1/2}$ transition at 422 nm is referred to as the "Doppler-cooling" transition. The $^2D_{3/2}$—$^2P_{1/2}$ transition at 1092 nm is referred to as the "repumper" transition. In general, the $^2S_{1/2}$—$^2D_{5/2}$ transition at 674 nm is referred to as the "probe" transition. Certain specific Zeeman components ($m_j = -1/2$—$m_j = -5/2$ and $m_j = -1/2$—$m_j = -1/2$

respectively) are termed the “sideband-cooling” and “spectroscopy” transitions. The $^2\mathrm{D}_{5/2}$—$^2\mathrm{P}_{3/2}$ transition at 1033 nm is referred to as the “quencher” transition in the context of sideband cooling, and as the “clearout” transition at all other times.

2.3 Radio-frequency traps

In this work, a single $^{88}\mathrm{Sr}^+$ ion is held in a radio-frequency endcap trap. Additionally a novel linear RF trap design is proposed. RF traps confine charged particles using time-varying inhomogeneous electric fields. The physics of RF ion traps is well established, and there exist several extensive reviews in the literature [15–17]. This section introduces the salient trapping concepts. In particular, it describes two basic types of trap geometry, some of the restrictions placed upon trapping fields to ensure stable ion confinement, and some of the issues concerning a type of motion in the trap termed “micromotion”.

A charged particle cannot be trapped in three dimensions by a static electric field. Specifically, for a harmonic potential:

$$\Phi = \Phi_0(\alpha X^2 + \beta Y^2 + \gamma Z^2), \tag{2.1}$$

the Laplace condition, $\nabla^2\Phi = 0$, dictates that:

$$\alpha + \beta + \gamma = 0. \tag{2.2}$$

This requires that the field is anti-trapping in at least one direction. Nonetheless, if this quadrupole field is varied periodically in time, then there is a

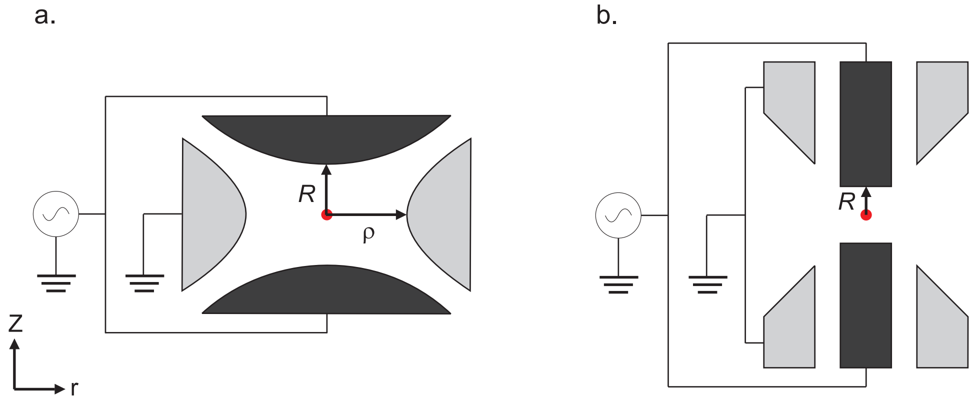

Figure 2.2: Realisations of a spherical RF trap. These show cross sections through the trap, where the full electrodes are solids of rotation about the Z-axis. In each case an RF voltage, $V(t) = V_0 \cos(\Omega_{\mathrm{T}} t)$, is applied to the electrodes shaded black, while the grey electrodes are grounded. The circle marks the position of the trap centre. (a) An ideal hyperbolic trap. (b) An endcap trap provides an example of an non-ideal trap. See text for details.

small, time-averaged resultant force which acts towards the centre of the trap [59, 60]. There are two common ways to realise the solution of eq. 2.2. One is where $\alpha = \beta = 1$; $\gamma = -2$. The second is where $\alpha = 1 = -\beta$; $\gamma = 0$. The electrode structures required to realise these solutions are called spherical traps and linear traps respectively. The physics of these two types of traps is now addressed in turn.

2.3.1 Spherical traps

The first solution to eq. 2.2 can be realised physically in a spherical Paul trap (often simply called a Paul trap) which is illustrated in figure 2.2a. This consists of a ring of hyperbolic cross section, with a pair of hyperboloid endcaps above and below. The entire trap has rotational symmetry about the Z-axis. From eq. 2.1 this provides a potential:

$$\Phi = \frac{\Phi_0}{2R^2}\left(\frac{r^2}{2} - Z^2\right) \tag{2.3}$$

where R is the distance between the ion and the nearest electrode, ρ is the distance from the ion to the ring and, by convention, $\rho^2 = 2R^2$. The alternating trapping potential at the boundary, Φ_0, is provided by applying an RF voltage, $V(t) = V_0 \cos(\Omega_{\mathrm{T}} t)$, to the endcaps and grounding the ring. The physics of trapping is exactly equivalent if the RF voltage is applied to the ring, and the endcaps are grounded.

Rather than considering a time-varying potential, it is convenient to consider the effective, time-averaged confining potential, or pseudopotential, ψ [59]:

$$\psi = \frac{e^2}{4M\Omega_{\mathrm{T}}^2}|\nabla\Phi(X,Y,Z)|^2 \tag{2.4}$$

where e is the charge on the ion, M is the ion's mass, and $\Phi(X,Y,Z)$ is the instantaneous potential when $\Phi_0 = V_0$. It may be noted that $\nabla\Phi$ is the electric field. The component of the motion due to the pseudopotential is called the secular motion ("secular" meaning "slow". The pseudopotential approximation neglects a rapid component of the motion at the trap drive frequency, called the micromotion. This is considered in section 2.3.4). For an idealised Paul trap the pseudopotential causes the ion to oscillate in the axial and radial directions with secular frequencies, ω_{Z}, ω_{r}, which (to first order) are given by [60]:

$$\begin{aligned}\omega_{\mathrm{Z}} &= \frac{eV_0}{\sqrt{2}M\Omega_{\mathrm{T}}R} \quad , \\ \omega_{\mathrm{r}} &= \frac{eV_0}{2\sqrt{2}M\Omega_{\mathrm{T}}R} \; .\end{aligned} \tag{2.5}$$

Higher order corrections can be found in reference [61], though for the present work eq. 2.5 is sufficient.

The hyperbolic electrode surfaces depicted in figure 2.2a are not easy to accurately machine on small scales. Additionally, the optical access for such a geometry is not great, as the ring largely obscures an ion at the centre of the trap. It is, however, possible to depart significantly from such an idealised geometry, and still retain a harmonic potential near the trap centre [62–66]. One such trap—an endcap trap [64]—is illustrated in figure 2.2b. In this realisation it can be imagined that the grounded ring of the ideal case has essentially been split in two, and moved to the sides of the endcap electrodes. Having deformed the trap in such a manner, the basic physics of trapping remains the same. However, not all of the applied voltage contributes to the harmonic potential as, in addition to the quadrupole potential of the idealised trap, the potential now also has higher-order terms. The harmonic oscillations which the ion undergoes near the centre of the trap are therefore effectively driven by a smaller RF voltage. The effect of the driving voltage is therefore reduced by a factor η, called the trap efficiency. This is defined as the ratio of the quadrupole component of a given trap to that of a hyperbolic trap of the same characteristic dimension, R. The motional frequencies in a general spherical trap therefore become:

$$\begin{aligned} \omega_{\mathrm{Z}} &= \frac{e\eta V_0}{\sqrt{2}M\Omega_{\mathrm{T}}R} \quad , \\ \omega_{\mathrm{r}} &= \frac{e\eta V_0}{2\sqrt{2}M\Omega_{\mathrm{T}}R} \quad . \end{aligned} \tag{2.6}$$

In general, the efficiency cannot be calculated analytically, but requires a numerical approach. This is explained fully in chapter 6.

2.3.2 Linear traps

The second solution to eq. 2.2 can be realised physically in a linear Paul trap, illustrated in figure 2.3a. This consists of four long rods, each of hyperbolic cross section. By applying an RF voltage, $V(t) = V_0 \cos(\Omega_{\mathrm{T}} t)$, to one diagonal pair of electrodes and grounding the remaining pair, this trap provides a potential:

$$\Phi = \frac{\Phi_0}{2R^2}(X^2 - Y^2). \tag{2.7}$$

The expression for the pseudopotential in eq. 2.4 is entirely general, and is therefore applicable to this linear geometry. From eq. 2.7 it is clear that the pseudopotential in this case is planar; it has no axial (Z) component. This can easily be understood from the axial symmetry of the design. Unlike a spherical trap, which has an RF null at a single point at the centre, a linear trap has an RF null which extends along the length of the trap axis. The trap can be made to be confining in the axial direction by the addition of DC electrodes at either end.

As with the spherical Paul trap, the hyperbolic electrodes are not easy to

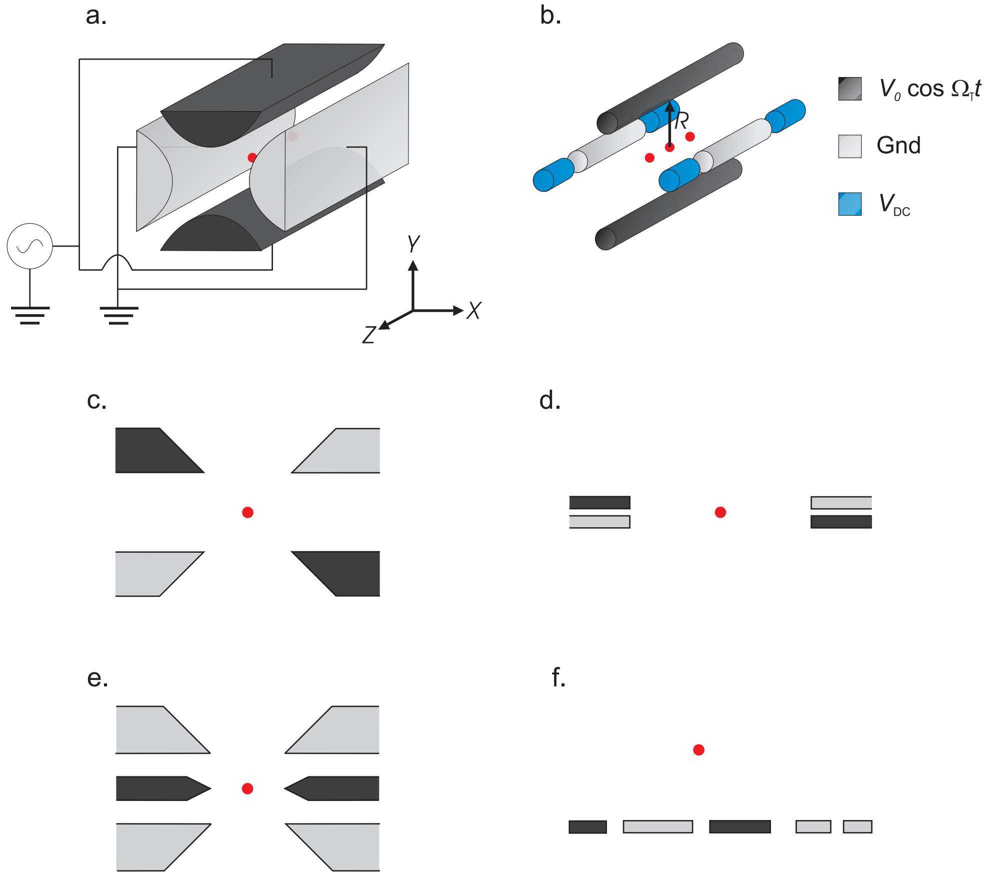

Figure 2.3: Realisations of a linear RF trap. In each case an RF voltage, $V(t) = V_0 \cos(\Omega_{\mathrm{T}} t)$, is applied to the electrodes shaded black, while the grey electrodes are held at RF ground. (a) Hyperbolic electrodes realise the ideal potential of eq. 2.7. By symmetry it can be seen that the RF potential is not axially confining. (b) Typically, the ideal case is approximated by four circular rods, instead of hyperbolae. Endcap electrodes are held at a small, positive DC voltage to axially confine ions. (c)–(f) Cross sections through the XY-plane of various linear traps in the literature (see text for details). In each case, the circle marks the position of the trap axis.

machine accurately. However, hyperbolic electrodes are also not necessary, and a wide range of geometries can be made which approximate the ideal potential, and which retain a harmonic potential at the trap centre. Typically, the four hyperbolic electrodes can be replaced with four wires of circular cross section, *e.g.* [67–69]. Figure 2.3b shows a typical design, including the endcap electrodes, held at a small, positive DC voltage to provide axial confinement. For a variety of reasons, generally related to fabrication, and particularly to microfabrication, it may be desirable to deform the geometry further. For example, traps have been designed and made where the electrodes consist of four flat planes (figure 2.3c) [11, 50]; four planes arranged with a very high aspect ratio (figure 2.3d) [70, 71]; six electrodes arranged in three layers (figure 2.3e) [72–75]; or even with all the electrodes in a single plane (figure 2.3f) [76, 77]. In each case, the physics of trapping remains essentially unchanged, though the trap efficiencies can vary significantly (to as low as $\eta = 0.3$ in the case of the trap in figure 2.3f).

The motional frequencies in linear traps are given by [70]:

$$\begin{aligned} \omega_{\mathrm{Z}} &= \sqrt{\frac{2\kappa e V_{\mathrm{DC}}}{M f}} \quad , \\ \omega_{\mathrm{r}} &= \frac{e\ V_0\ \eta}{\sqrt{2}\ M\ \Omega_{\mathrm{T}}\ R^2}\ , \end{aligned} \tag{2.8}$$

where κ is a geometrical factor related to the placement of the endcap electrodes, and f is the distance from the ion to the nearest endcap electrode. It should be noted that in addition to providing axial confinement, the use of endcap electrodes may lift the degeneracy of ω_{r}, depending on the geometry of the endcaps. This is discussed in more detail in chapter 6.

For a given fidelity of operation, the speed of a Cirac-Zoller type ion-trap quantum processor scales as the geometrical mean of the ions' motional frequency and the photon recoil frequency associated with the ion string [78]. Any practical ion trap for quantum information processing (QIP) applications should therefore have as high a motional frequency as possible. Frequencies currently realised are in the range of several megahertz, *e.g.* an axial centre of mass (COM) mode of $\omega_{\mathrm{ZCOM}}/2\pi = 3.4$ MHz has been used when creating a 6-ion entangled state [28], and a breathing mode for 2 ions of $\omega_{\mathrm{Zb}}/2\pi = 2.1$ MHz was used in a C-NOT gate [45]. (For comparison, this implies $\omega_{\mathrm{ZCOM}}/2\pi = 1.2$ MHz.) It should be noted that the axial centre of mass (COM) motional frequency on a string of N ions is independent of N [44, 67].

2.3.3 Stability requirements

For an ion trap to provide a stable trapping potential it is not sufficient to simply apply a general RF voltage to the electrodes; the equations of motion for a trapped ion only have sinusoidal (*i.e.* stably trapped) solutions for certain values of the applied voltage and drive frequency [60, 79]. These dependencies are summed up in a set of dimensionless stability parameters, a and q. In introducing these it must be first noted that, to be entirely general, the electrodes held at RF ground need not also be maintained at DC ground, and for a variety of reasons, it is often useful to hold them at some small DC voltage, U_0. If S and L denote spherical and linear traps respectively, and r

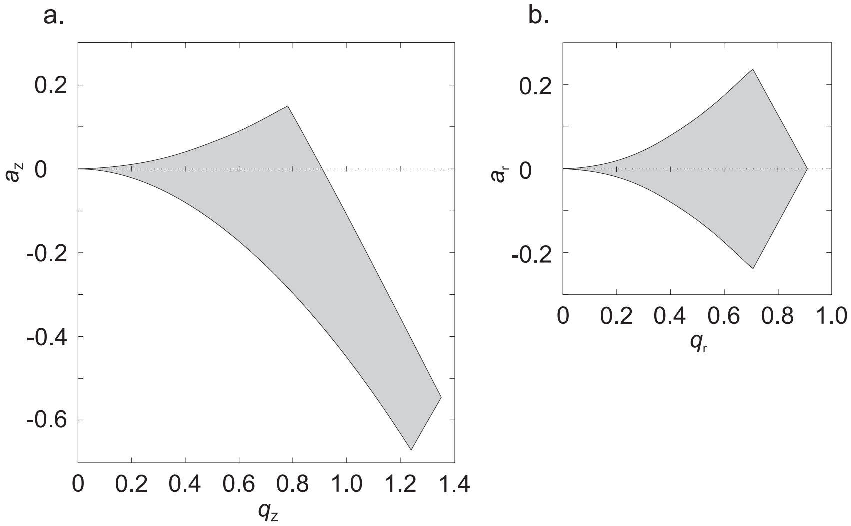

Figure 2.4: Stability conditions for spherical and linear traps. In order to provide a stable trapping potential, the parameters a and q (defined in the text) must be kept within certain bounds. The shaded regions show the stable values for (a) a spherical trap, and (b) a linear trap.

and Z denote axial and radial directions, the a and q parameters are defined as [60]:

$$\begin{aligned} a_{\mathrm{r}}^{L} = \quad a_{\mathrm{Z}}^{S} = -2a_{\mathrm{r}}^{S} \quad &= \frac{4e\eta U_0}{MR^2\Omega_{\mathrm{T}}^2} \ , \\ q_{\mathrm{r}}^{L} = -q_{\mathrm{Z}}^{S} = \quad 2q_{\mathrm{r}}^{S} \quad &= \frac{2e\eta V_0}{MR^2\Omega_{\mathrm{T}}^2} \ . \end{aligned} \tag{2.9}$$

The q parameter provides stability constraints on the amplitude of the RF voltage, and the a parameter constrains the DC offset. In a linear trap, even with DC endcap electrodes, there is no axial RF field and so $q_Z^L = 0$. In order for the ion's trajectory to remain stable these parameters must be kept within certain bounds, as illustrated in figure 2.4 [17, 60, 79, 80]. Outside of these values the oscillations in the ion's motion grow exponentially and the ion is ejected from the trap.

It must additionally be noted that a linear trap of the type shown in figure 2.3b also has endcap electrodes held at a voltage V_{DC}. There are therefore further stability conditions to be met, which depend on these endcap voltages. The relevant parameters are combined in the dimensionless parameters a_{r}^{DC} and a_{Z}^{DC}, defined as [81]:

$$a_{\mathrm{Z}}^{DC} = -2a_{\mathrm{r}}^{DC} = -\frac{8e\kappa V_{\mathrm{DC}}}{Mf^2\Omega_{\mathrm{T}}^2}. \tag{2.10}$$

The stability requirements—that a and q fall within certain values—apply to harmonic potentials. If the potential is not perfectly harmonic, then the ion can be driven by higher-order-harmonic terms and areas of instability can occur within an otherwise stable region of parameter space. [80]. These problems are more frequent towards higher values of q, and so traps are typically operated in the region $q \simeq 0.6$, *e.g.*[50, 71, 82]. From eqs. 2.8 and 2.9 for a given, fixed q, an ion's radial motional frequency, ω_{r}, is proportional to the drive frequency, Ω_{T}. Provided $q^2 \ll 2$, and neglecting perturbations from the endcap voltages, this can be approximated as [15, 61]:

$$\omega_{\mathrm{r}} \simeq \frac{q}{2\sqrt{2}}\,\Omega_{\mathrm{T}}. \tag{2.11}$$

Many applications of linear RF ion traps (including trapped-ion quantum computing, as planned for the linear trap described in chapters 6 and 7) require a one-dimensional string of ions, aligned along the trap axis. If the axial confinement of a 1D string of N ions is too strong compared to the radial confinement, then the string undergoes a phase transition from one to two dimensions. The strength of the confinement is characterised by the ions' motional frequencies, and it has been found numerically that to maintain a linear string, the motional frequencies must obey the inequality [83][1]:

$$\omega_{\mathrm{ZCOM}} < 1.57 N^{-0.87} \omega_{\mathrm{r}-} \tag{2.12}$$

where $\omega_{\mathrm{r}-}$ is the lower radial motional frequency, in the general case where the radial frequencies are non-degenerate. To achieve a linear string of 4 ions with $\omega_{\mathrm{ZCOM}}/2\pi = 2$ MHz therefore requires $\omega_{\mathrm{r}}/2\pi > 4.3$ MHz.

2.3.4 Micromotion

So far, the description of the ions' motion within a trap has assumed that the potential an ion sees can be well described by the pseudopotential approximation (eq. 2.4). Exactly at the centre of the trap there is an RF null at the nodal position of the RF field, and the approximation holds well. However, when the ion departs from this position (as an oscillating ion must) it also experiences a driven motion at the trap drive frequency, called micromotion. In a linear trap this only occurs in the radial direction, as the RF field has no axial component (*c.f.* eq. 2.7), while in a spherical trap micromotion occurs in all directions. In as much as an ion can never be confined at rest at the trap centre, micromotion is ubiquitous. However, if stray DC fields displace the

---

[1] Note: eq. 2.12 is derived from figure 4 of this reference. The figure requires that the scaling constant for the power law given is $c = 10^{0.395}$, rather than $c = 0.395$ as given in the text of the paper.

average position of the ion from the RF null, then the ion undergoes excess micromotion [81]. Depending on the degree to which the ion is displaced, this driven motion can have several significant, detrimental effects.

Whereas secular motion is thermal in nature, micromotion is driven and cannot be significantly reduced by cooling the ion. Conversely, if more than one ion is confined in the trap, the micromotion of one ion can be coupled to the secular motion of another and lead to ion heating [84]. Furthermore, the modulation of the atomic transition due to micromotion adds RF sidebands to the usual components of the ion's transition spectrum. This reduces the strength of laser-ion interactions involving the carrier. It can also lead to laser heating of the ion, if a laser which would otherwise cool the ion is blue-detuned of a micromotion sideband [81, 84]. Methods of minimising excess micromotion are discussed in chapters 3–4.

2.4 Laser cooling

Due to the uncertainty relationship between position and momentum an ion held in a finite volume of space cannot also be completely at rest. Even in its motional ground state it still has some energy, simply due to being confined. This is termed the zero-point energy. For many QIP applications an ion must be cooled to (or very close to) this energy. This is termed "ground-state cooling" or "zero-point cooling". Laser cooling was used to achieve the zero-point cooling presented in chapter 5. The two laser cooling methods required are now described.

2.4.1 Doppler cooling

Doppler cooling is a commonly used technique for cooling trapped ions, and there are numerous reviews on the subject [85–88]. In outline, Doppler cooling works as follows. An ion is excited by absorbing a photon (and the associated momentum) which is incident upon it from a particular direction. The ion then spontaneously decays back to the ground state, emitting a photon in a randomised direction, and by so doing receives a randomised momentum kick. Averaged over many absorption-emission cycles, this process results in a net reduction in the velocity of the ion towards the incident light source. By detuning the laser wavelength below the transition resonance, the motion of the ion Doppler shifts the light into resonance when moving towards the source, and out of resonance when moving away from it. A bound ion can be cooled in three dimensions by a single laser which is incident at an angle oblique to all three principal axes of the ion's motion. At some point the heating effect from the randomised momentum kicks exactly balances the cooling effect, and no further net cooling occurs. By setting the laser detuning to $-\Gamma/2$ from resonance the Doppler limit—the lowest motional state achievable by Doppler cooling—can be obtained. This has a mean vibrational quantum number of [88]:

$$\bar{n}_{\mathrm{min}} = \frac{1}{2}\left(\frac{\Gamma}{\omega} - 1\right). \tag{2.13}$$

With typical linewidths of dipole transitions, Γ, being several tens of MHz, and typical trap frequencies, ω, of a few MHz, this process can cool an ion to only a few vibrational quanta, but is generally insufficient to cool an ion to the ground state ($n = 0$).

2.4.2 Sideband cooling

A cold ion can be cooled to the ground state using the technique of resolved-sideband cooling [86, 89–91]. The principle of this process is outlined here, along with a description of the way the atomic spectrum is modified for very cold ions, and how this can be used to measure the ground-state occupation probability. The experimental procedure used for sideband cooling is explained in further detail in chapter 5.

The degree of confinement of a bound ion interacting with light of wavelength λ, incident at an angle θ, with the ion's motional mode is quantified by the Lamb-Dicke parameter [17, 92]:

$$\eta = \frac{2\pi}{\lambda} \cos\theta \sqrt{\frac{\hbar}{2M\omega}}. \tag{2.14}$$

The ion is said to be in the Lamb-Dicke regime if $\eta\sqrt{2\bar{n}+1} \ll 1$. This is easily achievable by Doppler cooling. In the Lamb-Dicke regime the narrow $^2\mathrm{S}_{1/2}$—$^2\mathrm{D}_{5/2}$ transition in $^{88}\mathrm{Sr}^+$ has well-resolved motional sidebands spaced by $\pm\omega$ from the carrier [17], as required for resolved-sideband cooling. In this method the transition is excited on the red (lower) motional sideband, though it decays predominantly on the carrier. This reduces the phonon number of the ion by one for each cooling cycle until a high ground-state-occupation probability is reached.

In the Lamb-Dicke regime the coupling strengths of the carrier, and blue and red sidebands respectively are [15]:

$$\begin{aligned}\Omega_{n,n} &= \Omega_0 \\ \Omega_{n,n+1} &= \Omega_0 \eta \sqrt{n+1} \\ \Omega_{n,n-1} &= \Omega_0 \eta \sqrt{n}.\end{aligned} \tag{2.15}$$

From this it can also be seen that the coupling strength of the red sideband goes to zero as $n \to 0$. It can be seen from eq. 2.15 that the mean vibrational quantum number can be calculated from the ratio of the red and blue sideband coupling strengths as:

$$\bar{n} = \frac{1}{\left(\frac{\Omega_{n,n+1}}{\Omega_{n,n-1}}\right)^2 - 1}. \tag{2.16}$$

By assuming a thermal superposition of states, the occupation probability for any particular state, n, given a mean phonon number, $\bar{n}$, is [17]:

$$P(n|\bar{n}) = \frac{\bar{n}^n}{(1+\bar{n})^{1+n}}. \tag{2.17}$$

In practice, an occupation probability of unity cannot be obtained for the ground state by sideband cooling, as the sideband cooling process also induces heating effects due to off-resonant excitations.

CHAPTER 3

Experimental setup

3.1 Introduction

In this experiment a Sr atom is efficiently photoionised and trapped in an RF endcap trap. This single $^{88}\mathrm{Sr}^{+}$ ion is then cooled to the ground state of its axial motion. Such a motional state is a prerequisite for many QIP applications. This chapter describes the experimental apparatus required to achieve such ground-state cooling.

With reference to figure 2.1, atoms from a Sr source are photoionised via a two-step resonant process by excitation of the atom on the $^1\mathrm{S}_0$—$^1\mathrm{P}_1$ transition with 461 nm radiation, followed by excitation with 405 nm radiation to the autoionising ($4\mathrm{d}^2$+$5\mathrm{p}^2$) $^1\mathrm{D}_2$ state [93]. A single ion so produced is then trapped in an RF endcap trap where it can be held in a controlled environment in a well-characterised harmonic potential, and with a known applied magnetic field. The ion is Doppler cooled on the $^2\mathrm{S}_{1/2}$—$^2\mathrm{P}_{1/2}$ dipole transition with 422 nm light. To prevent the ion being lost from the cooling cycle due to decay from the ^{2}P$_{1/2}$ level to the ^{2}D$_{3/2}$ state, a 1092 nm laser resonant with this transition returns the ion to the cooling cycle. Sideband cooling to the motional ground state is carried out by driving the motional sidebands of a particular Zeeman sublevel of the ^{2}S$_{1/2}$—^{2}D$_{5/2}$ quadrupole transition with light at 674 nm [94] where the Zeeman sublevels are resolved by applying a magnetic field of 380 μT. The upper state of this transition is long-lived (τ = 390 ms [31]) and so must be quenched in order for cooling to proceed at an appreciable rate. This is achieved using 1033 nm radiation which couples the ^{2}D$_{5/2}$ state to the ^{2}P$_{3/2}$ state, from which the ion rapidly returns to the ground state. The state of the ion can be measured using Dehmelt's electron shelving technique by detecting the 422 nm light scattered by the ion.

Much of the apparatus described in this chapter was extant at the start of this thesis work. There are, however, several parts of the set-up which were built or improved as part of this work. The 461 nm source (comprising a 922 nm external-cavity diode laser [ECDL], and a frequency-doubling cavity) and the 405 nm laser were designed and built so that a new photoionisation scheme could be implemented. The pre-existing 422 nm Doppler-cooling laser was rebuilt using a new design (similar to that of the 461 nm photoionisation system), to improve the reliability of its operation. The 922 nm ECDL design used as part of the photoionisation system was also adapted to replace the previous 1033 nm quencher / clearout laser.

This chapter is organised as follows. The endcap trap and associated apparatus are described in section 3.2. The laser systems are described in section 3.3. Specifically, sections 3.3.1–3.3.2 describe the 461 nm and 405 nm sources used for photoionisation. Sections 3.3.3–3.3.4 describe the 422 nm and 1092 nm sources used for Doppler cooling. Sections 3.3.5–3.3.6 describe the 674 nm and 1033 nm sources required for sideband cooling and spectroscopy. The experimental procedures required to load a single Sr^+ ion are described in section 3.4. The apparatus associated with the microfabricated linear ion trap developed during this work [95] is not included in this chapter, but is covered in chapter 7.

3.2 Ion trap apparatus

3.2.1 Endcap trap

The ion is confined in an RF endcap trap, identical in design to that of Schrama *et al.* [64]. The trap (shown schematically in figure 3.1) is formed by a pair of 500 μm diameter tantalum wires with a tip-to-tip separation of 560 μm. These are each shielded by a concentric cylindrical outer electrode, which is also made of tantalum. The inner and outer endcaps are separated by a ceramic spacer. This geometry allows a harmonic potential to be produced, with efficiency $\eta = 0.64$, while maintaining a high degree of optical access.

Structure on an electrode's surface may contribute to setting up spatial variations in the electrode-material work function [96]. This is described further in section 4.2, though it is noted here that this is thought to be a cause of ion-heating. To reduce this possible cause, the tips of the inner endcap electrodes are abrasively polished to be smooth on the μm scale. The inner endcaps have an RF voltage applied, while the outer endcaps are held at RF-ground. Small DC bias voltages can be applied to either outer

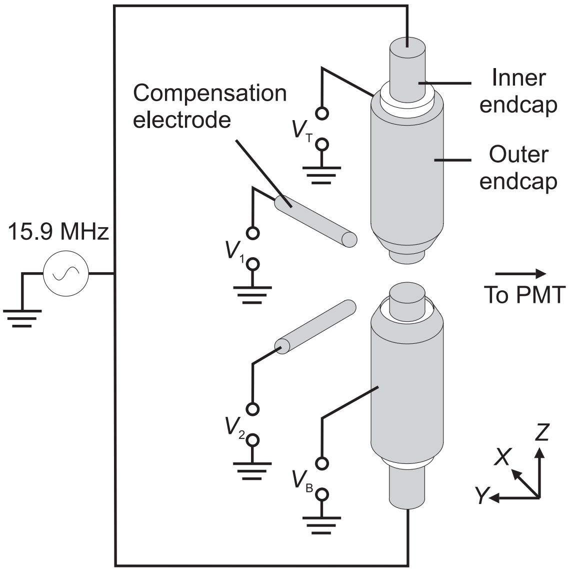

Figure 3.1: Endcap-trap schematic.

endcap to minimise axial micromotion. The ratios of axial to radial frequencies, $\omega_{\mathrm{X,Y}}/\omega_{\mathrm{Z}}$, can be varied by adding a DC voltage to both outer endcaps. Additionally there are two orthogonal compensation electrodes in the radial plane to which small DC voltages can be applied in order to minimise the radial micromotion. All trap electrodes are held by a macor structure which is mounted directly onto a 20-pin UHV feedthrough (2.75” conflat flange) as shown in figure 3.2. The DC electrodes are spot-welded to constantan pins on the feedthrough, and the RF source is connected to a separate feedthrough in order to minimise pickup on DC lines.

Sr vapour is generated using an oven and hotplate arrangement, analogous to that used in Ba by DeVoe and Kurtsiefer [97]. This arrangement can be seen in figure 3.2. The loading method used with the oven and hotplate system is outlined in section 3.4. It is noted here, however, that there is no

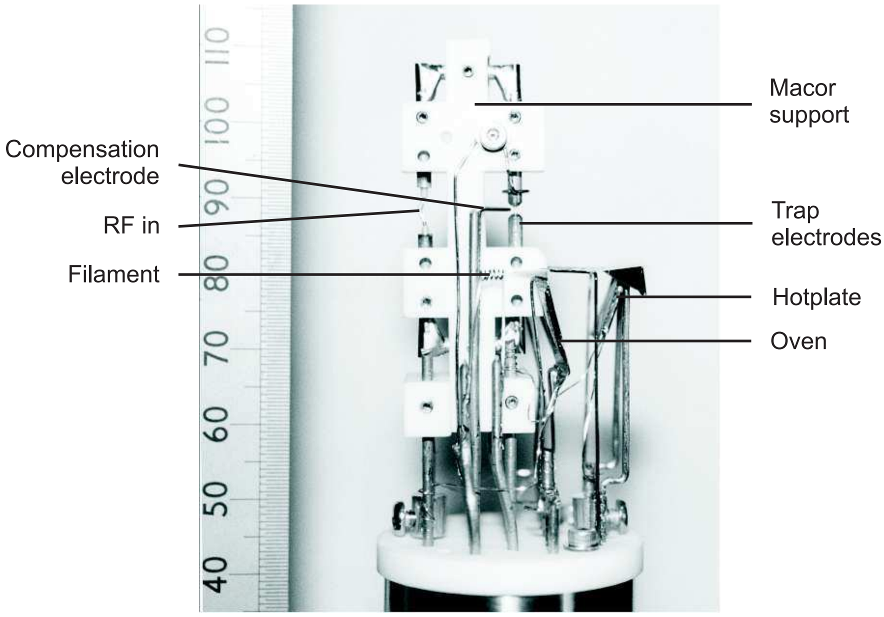

Figure 3.2: Photograph of an endcap trap, showing oven and hotplate arrangement.

line of sight between the oven apertures and the trap, so that no material from the ovens (be it Sr or impurity elements) can be evaporated from there onto the electrodes. Both the ovens and the hotplate are made of tantalum foil, and have their temperatures monitored by thermocouples spot-welded to them. Two tungsten filaments are positioned ∼15 mm from the trap. If photoionisation loading is not used, these can be used instead to produce a flux of electrons to ionise the Sr vapour from the hotplate. As with the DC trap electrodes, all electrical connections for the loading system are made via constantan pins in the vacuum feedthrough.

3.2.2 Trap drive

The RF trapping voltage is supplied by a high-Q helical resonator [98] driven by an RF synthesiser and amplifier. The helical resonator has an outer shield diameter of 100 mm and an unloaded Q of 500, at a resonant frequency of 43.4 MHz. This Q is reduced to ∼90, with a resonant frequency of 15.9 MHz when it is loaded by the endcap trap. The output of the resonator is highly harmonic, with the second order harmonics being 70 dB below the fundamental. Based on calculations of the endcap trap's efficiency carried out using SIMION 3D[1], the amplitude of the trap-drive voltage at the trap is inferred to be $V_0 = 390$ V, under standard operating conditions. This yields axial and radial motional frequencies of $\omega_{\mathrm{Z}}/2\pi \simeq 3.8$ MHz and $\omega_{\mathrm{r}}/2\pi \simeq 2.0$ MHz respectively.

3.2.3 Vacuum system

The trap is mounted within a cylindrical stainless-steel vacuum chamber, 250 mm long and 150 mm in diameter. The trap itself is mounted directly onto a conflat flange, with all DC connections entering the chamber via this feedthrough, and the RF connection entering via a separate feedthrough. The windows for laser access are mounted a distance of ∼10 cm from the trap, and one end of the chamber comprises a 150 mm re-entrant window to provide optical access for the imaging system. The chamber is pumped down to a pressure of 10^{-11} mbar by a Varian triode pump and SAES non-evaporable getter pump.

---

[1] SIMION 3D 7.0, Scientific Instrument Services, Inc. NJ. 2003.

The Zeeman splittings of the ion's energy levels are magnetic-field dependent. To control the magnitude of the Zeeman splitting, stray magnetic fields at the ion can be offset, and additional fields applied, using three orthogonal pairs of magnetic field coils wound outside the vacuum chamber. All three pairs of coils are used to null the ambient magnetic field. The X coils (*i.e.* the coils which produce a magnetic field along the X-direction) are then used to apply a known magnetic field to the ion. The current in the field coils produces a magnetic field at the ion of 140×10^{-6} T/A.

3.2.4 Imaging optics

The state of the ion is detected using Dehmelt's shelving technique [46]. This requires that the light scattered on the $^2\mathrm{S}_{1/2}$—$^2\mathrm{P}_{1/2}$ transition is detected. This is done by imaging the ion onto a photo-multiplier tube (PMT). One end of the chamber (in the $-\hat{Y}$ direction) has a 150 mm re-entrant window to allow a large solid angle for fluorescence detection. The 422 nm light scattered from the ion is focused by a multi-element lens (f/# = 1.05, focal length = 69 mm, magnification = 10) through a 200 μm pinhole onto the PMT. The PMT has a short pass filter to reduce sensitivity to any light at 674-, 1033- and 1092 nm which may be scattered from the trap electrodes. It does not filter light at 461- or 405 nm, and for this reason the light scattered from the cooling transition cannot be measured while the photoionisation lasers are incident on the trapping region. The PMT dark count is $\sim$10 s^{-1}. The background count with the cooling lasers incident on the ion, and the ion in a dark state, can be up to 1600 s^{-1}. The fluorescence count rate when a single cooling beam is incident, detuned by $-\Gamma/2$, is $\sim 2 \times 10^4$ s^{-1}.

3.3 Lasers

3.3.1 461 nm photoionisation laser

In the first step of the photoionisation process, light at 461 nm is used to resonantly excite Sr atoms from the ground state on the 5s^2 ^{1}S$_0$—5s5p ^{1}P$_1$ transition. It is generated by frequency doubling 922 nm light from an external-cavity diode laser (ECDL) using potassium niobate ($KNbO_3$; KN) in a resonant build-up cavity. The experimental arrangement is illustrated in figure 3.3.

922 nm light from a laser diode (Toptica LD-0935-0050-AR-2) is collimated, and incident on a ruled grating (1200 lines/mm, 200 nm blaze, ∼10% feedback) at the Littrow angle (33.6°) to form a 40 mm long external cavity. As the grating angle is tuned, the wavelength fed back to the laser changes, as does the length of the cavity. By correct positioning of the pivot point these two parameters can be made to tune synchronously, or near synchronously, as the grating angle is changed [99, 100]. In principle, mode hops due to the competition of these two effects can be avoided all together. However, the tuning range falls dramatically if the pivot point is moved even slightly from this ‘perfect’ point in a particular direction [100]. By operating in certain regions away from the perfect pivot point a compromise can be struck between an acceptable machining tolerance and a wide tuning range. The ECDL was designed so that it has a reasonable mode-hop-free tuning range (∼20 GHz)

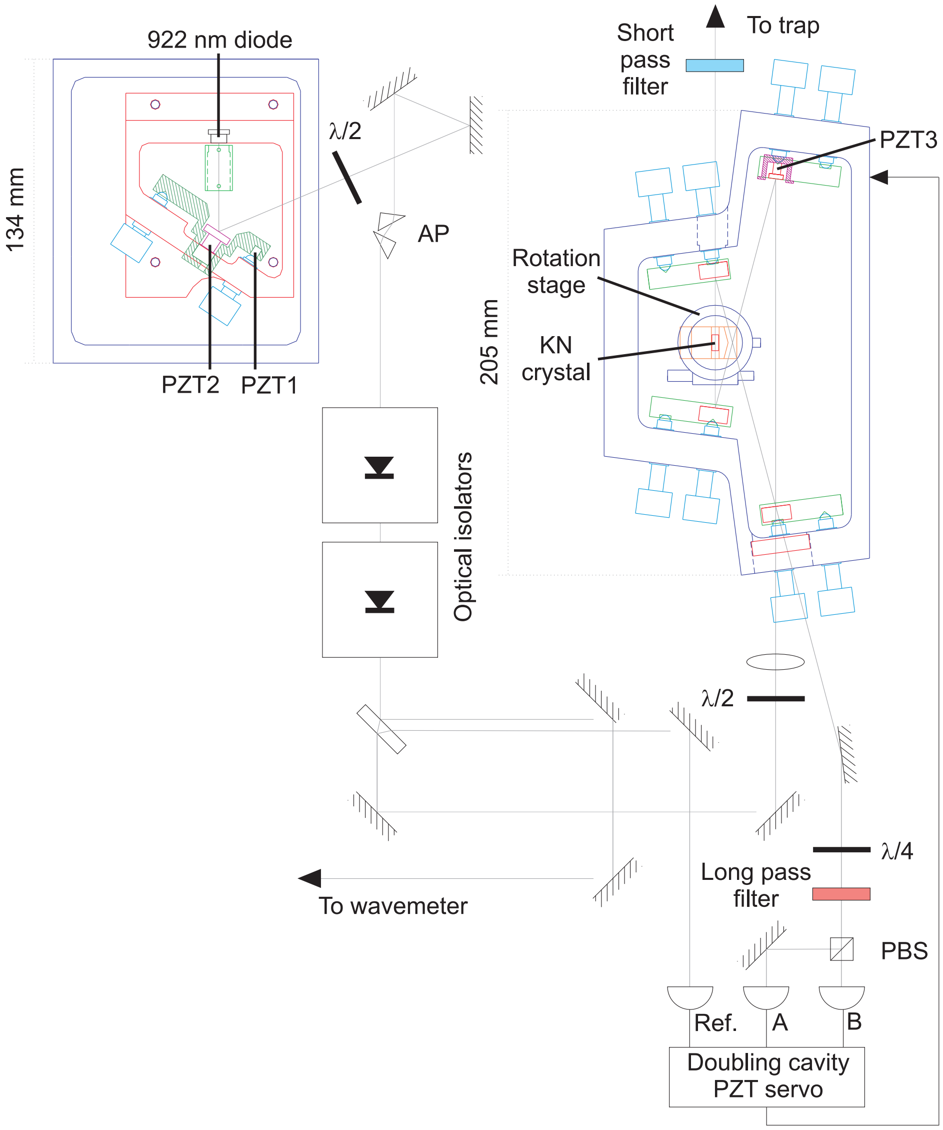

Figure 3.3: 461 nm laser.

and can be reliably machined. The angle of the grating is adjusted in the first instance using fine-pitched screws. Thereafter adjustment of the grating angle is provided by a long extension piezo (PZT1, figure 3.3) which changes the angle of the grating holder. The grating itself is mounted on a tubular piezo (PZT2) to provide fast feedback to the length of the cavity if required. The passive stability of the ECDL, and the requirements for photoionisation, are such that the fast feedback is not used on this system. The laser diode, grating and lens are all mounted in a monolithic aluminium block. This is temperature controlled to ∼12°C by a Peltier cooler on the base, which is in turn mounted within a hermetically sealed aluminium outer block. This block also acts as a heatsink for the Peltier cooler. The output beam from the ECDL is circularised by a pair of anamorphic prisms (AP). A pair of optical isolators (-30 dB isolation each) prevent feedback into the laser from elements further along the optical path. The laser's wavelength is set to 921.7240(5) nm using a wavemeter, and the laser possesses sufficient passive stability to require no active frequency stabilisation.

461 nm radiation is obtained by frequency doubling of light using a non-linear crystal. The physics of non-linear interactions of focused beams is covered comprehensively by Boyd and Kleinman [101] and references therein. The 922 nm light is frequency doubled using KN in a resonant build-up cavity. This crystal was chosen as it has a very high non-linear coefficient. For high circulating fundamental powers (more than a few watts) KN suffers from a reduced conversion efficiency, and heating due to reabsorption of the harmonic light [102], though for the modest circulating powers in this application (a few hundred milliwatts), this is not of concern. To obtain an

appreciable conversion efficiency the phases of the fundamental and harmonic light must be matched throughout the crystal. Phase matching for 922 nm can be achieved in KN by both angle tuning and temperature tuning of the crystal's refractive indices. Temperature tuning of KN is ideal to achieve harmonic wavelengths around 430 nm, as the phase-matching temperature at this wavelength is around 20°C. At longer wavelengths temperature tuning becomes impractical, as KN undergoes a phase transition at 223°C [103]. At temperatures approaching this, the crystal becomes increasingly likely to permanently depole, particularly if the temperature is changed rapidly (by more than a few tens of degrees per hour) or inhomogeneously. The phase-matching temperature for non-critically tuned KN at 922 nm is 150°C [103] which is closer to the crystal's phase transition than is desirable. Walk-off in the crystal means that angle tuning is a little less efficient than the temperature-tuned equivalent, but phase matching can be achieved without risking permanently depoling the crystal.

The refractive indices, $n_{\mathrm{x}}, n_{\mathrm{y}}, n_{\mathrm{z}}$ of KN at 22° as a function of wavelength are given by the Sellmeier equations [104]:

$$\begin{aligned} n_{\mathrm{x}}^2 &= 4.4308 + \frac{0.1004}{\lambda^2 - 0.054084} - 0.019592\lambda^2, \\ n_{\mathrm{y}}^2 &= 4.8388 + \frac{0.12839}{\lambda^2 - 0.056342} - 0.025379\lambda^2, \\ n_{\mathrm{z}}^2 &= 4.9873 + \frac{0.15149}{\lambda^2 - 0.064143} - 0.028775\lambda^2, \end{aligned} \tag{3.1}$$

where λ is the wavelength in micrometres. For light propagating in the yz-plane, the ordinary refractive index $n_{\mathrm{o}} = n_{\mathrm{x}}$, and the extraordinary refractive index, n_e, is given by:

$$n_\mathrm{e}(\phi) = \left(\frac{\cos^2\phi}{n_\mathrm{y}^2} + \frac{\sin^2\phi}{n_z^2}\right)^{-\frac{1}{2}}, \tag{3.2}$$

where ϕ is the propagation angle of the light off z towards y. From eqs. 3.1–3.2 the condition for type-I phase matching, $n_\mathrm{e}(\lambda, \phi) = n_\mathrm{o}(\lambda/2)$, is met when $\phi = 44°$, at which point the refractive index is 2.248.

The second harmonic power, P_2, generated in a non-linear crystal of length l, and refractive index n, by a focused Gaussian beam of power P_1, is given by [101]:

$$P_2 = \frac{8\pi^2}{\epsilon_0 c} . \frac{d_\mathrm{eff}^2}{n^2} . \frac{1}{\lambda^3}\ lh\ P_1^2 \tag{3.3}$$

where d_eff is the effective non-linear coefficient and h is the Boyd-Kleinman factor. l is chosen to be 7 mm by physical considerations such as providing a reasonable acceptance angle and temperature sensitivity, and practical considerations such as cost and availability. The only remaining parameter not fixed by the physics of the problem is h. This is related to the tightness of the beam focus in the crystal for a given crystal length and walk-off [101]. For the 461 nm system considered, h is maximised when the beam waist in the cavity is $2w_0 = 35\ \mu$m, giving a value of $h = 0.22$.

The KN crystal was held in a build-up cavity with a build-up factor of ∼60. The build-up cavity described here is slightly different from the cavity shown in figure 3.3, which is described below. The main features of the two cavities are sufficiently similar that the figure remains instructive. The crystal holder was held at 24°C by a resistive heater. The holder was mounted on a rotation stage to allow the angle of the crystal to be optimised. The cavity was set up in a bow-tie configuration of total length 640 mm, with the focusing mirrors having a radius curvature of −100 mm. The input coupling mirror had a reflectivity of 97.5% at the fundamental wavelength. Around 18 mW of 922 nm light were incident on the cavity, with a coupling efficiency of 60%. This was focused to a waist of $2w_0 = 35\ \mu$m inside the crystal, and produced up to 1.6 mW of frequency-doubled light. The length of the build-up cavity was stabilised to the laser wavelength using a Hänsch-Couillaud lock [105], which fed back to a piezo stack on which one of the cavity mirrors was mounted (PZT3).

The 461 nm light is overlapped with the 405 nm photoionisation beam on a dichroic beam splitter, and coupled into an optical fibre. The output from the fibre is overlapped with the Doppler-cooling light (Doppler-cooling beam #2, *c.f.* table 3.1), and 800 μW of 461 nm light is focused to a spot of $2w_0$ = 200 μm at the centre of the trap. The light is switched using a mechanical shutter at the input to the fibre.

A second doubling cavity was built (shown in figure 3.3) to replace the one described above. The new design was made to be more compact than the previous cavity. The main housing is temperature controlled and machined from a single block of aluminium to ensure a lower thermal drift over a day. The cavity was designed so that, by modifying only the crystal holder, the same design could be used to double 843 nm light for the 422 nm Doppler-cooling system, In this new cavity, the KN crystal is mounted in a holder, temperature controlled to 24°C by a resistive heater. The holder is mounted on a rotation stage which—along with the cavity mirrors—is mounted inside a monolithic, hermetically sealed aluminium enclosure, itself temperature

Beam	Wavelength	Unit vector
Photoionisation beam 1	461 nm	$0.87\hat{X} - 0.34\hat{Y} + 0.34\hat{Z}$
Photoionisation beam 2	405 nm	$0.87\hat{X} - 0.34\hat{Y} + 0.34\hat{Z}$
Cooling beam 1	422 nm	$-0.87\hat{X} - 0.47\hat{Y} - 0.13\hat{Z}$
Cooling beam 2	422 nm	$0.87\hat{X} - 0.34\hat{Y} + 0.34\hat{Z}$
Cooling beam 3	422 nm	$-0.87\hat{X} + 0.13\hat{Y} + 0.47\hat{Z}$
Far detuned cooling beam	422 nm	$-0.87\hat{X} + 0.13\hat{Y} + 0.47\hat{Z}$
Optical-pumping beam	422 nm	$\hat{X}$
Repumper beam 1	1092 nm	$-0.87\hat{X} - 0.47\hat{Y} - 0.13\hat{Z}$
Repumper beam 1	1092 nm	$0.87\hat{X} + 0.34\hat{Y} + 0.34\hat{Z}$
Weak probe beam	674 nm	$0.87\hat{X} + 0.48\hat{Z}$
Intense probe beam	674 nm	$-0.87\hat{X} - 0.48\hat{Z}$
Quencher beam	1033 nm	$0.87\hat{X} - 0.13\hat{Y} - 0.47\hat{Z}$
Clearout beam	1033 nm	$\hat{X}$

Table 3.1: Summary of beam directions. Unit vectors are defined using right-handed coordinates such that $\underline{\hat{Z}}$ is aligned along the axis of the endcap trap (*c.f.* figure 3.1) and $\underline{\hat{Y}}$ is in the radial direction, with the imaging optics in the $-\underline{Y}$ direction.

controlled to 23°C. The cavity is set up in a bow-tie configuration of total length 410 mm with the focusing mirrors having a radius of curvature of −50 mm. The input coupling mirror has a reflectivity of 97.5% at the fundamental wavelength. The crystal cut and beam parameters within the crystal remain unchanged from the previous design. It is expected that the new, hermetically-sealed, temperature-controlled, monolithic design should make the system more robust and easier to operate on a day-to-day basis.

3.3.2 405 nm photoionisation laser

In the second step of the photoionisation process light at 405 nm is used to resonantly excite Sr atoms on the 5s5p $^1P_1$—($4d^2$+$5p^2$) $^1D_2$ transition. The doubly excited ($4d^2$+$5p^2$) $^1D_2$ state is autoionising and from here one electron returns to the ground state, while the other is ejected into the continuum. This process is very rapid, resulting in a very broad transition (∼0.9 nm [56]). Given this, the transition is driven by light from a temperature controlled, free-running diode laser (Nichea NDHV 310 APCE 1) centred at 404 ± 0.5 nm.

This radiation is overlapped with the 461 nm photoionisation beam on a dichroic beam splitter, and coupled into an optical fibre. The output from the fibre is overlapped with the Doppler-cooling light (Doppler-cooling beam #2, *c.f.* table 3.1), and 7 mW of power at 404 nm is focused to a spot of $2w_0 = 170\ \mu$m at the centre of the trap. The light is switched using a mechanical shutter at the input to the fibre.

3.3.3 422 nm Doppler-cooling laser

Having obtained a single $^{88}Sr^+$ ion it is initially cooled by Doppler cooling. Light at 422 nm is used to drive the 5s $^2S_{1/2}$—5p $^2P_{1/2}$ dipole transition. It is generated by frequency doubling 843 nm light from an ECDL using KN in a resonant build-up cavity. The experimental arrangement is illustrated in figure 3.4.

The design of the ECDL is similar to that of the 922 nm laser described in section 3.3.1. 843 nm light from a laser diode (Eagleyard EYP-RWE-0850-

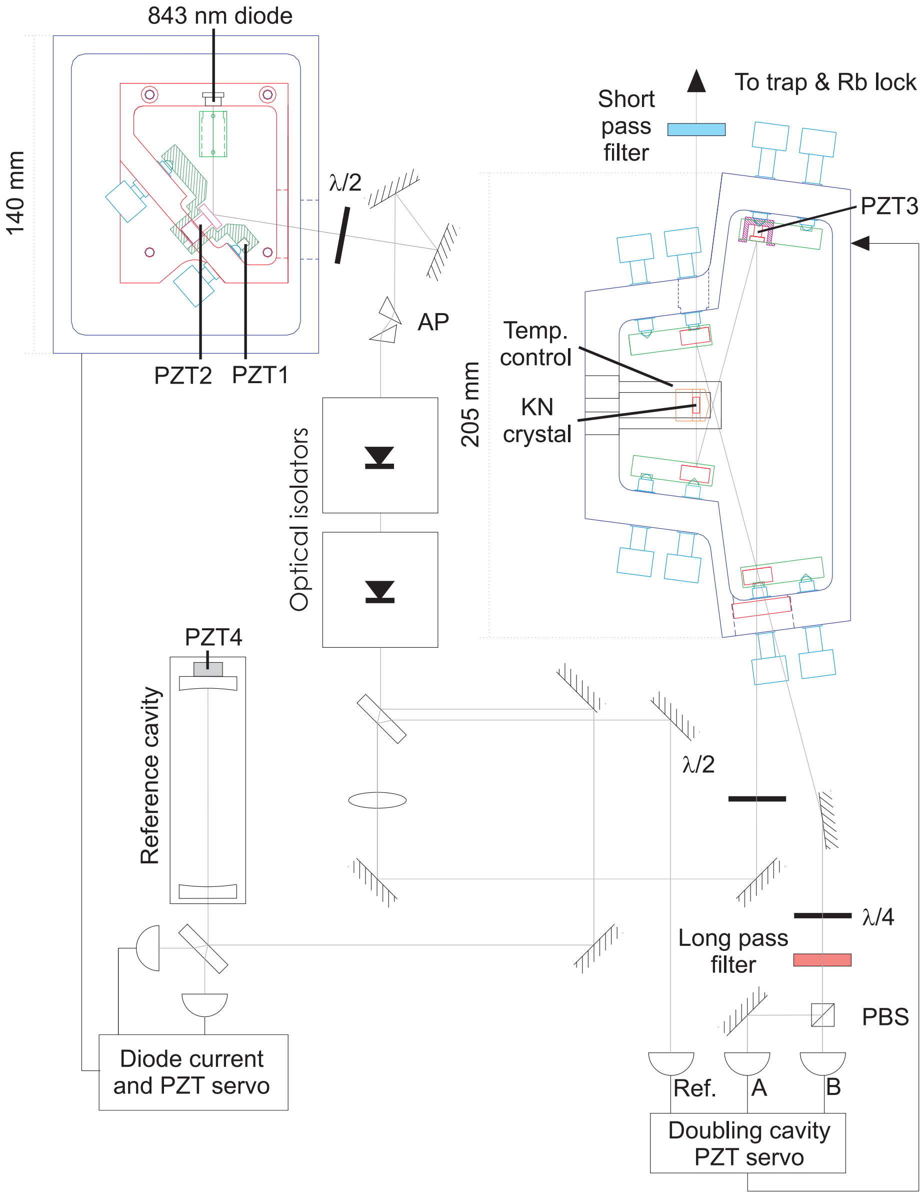

Figure 3.4: 422 nm laser.

05010) is collimated, and incident on a ruled grating (1800 lines/mm, 500 nm blaze, ~10% feedback) at the Littrow angle (49.4°) to form a 40 mm long external cavity. The stability requirements for the Doppler-cooling light are very much more stringent than those of the 461 nm photoionisation light, so the 843 nm ECDL is stabilised to a tuneable reference cavity (finesse = 115) by a side-of-fringe lock. This provides fast feedback to the laser via both the diode drive current and the tubular piezo on which the cavity grating is mounted (PZT2, figure 3.4).

The frequency doubling process was modelled using similar reasoning to the 461 nm system described in section 3.3.1. The 843 nm light is frequency doubled using a 7 mm long, non-critically phase matched (T = −17°C [103]) KN crystal in a build-up cavity. The crystal is temperature controlled using a Peltier cooler mounted on a water-cooled heatsink. The entire crystal mount—along with the cavity mirrors—is housed inside a monolithic, hermetically sealed aluminium enclosure, itself temperature controlled to 23°C. The enclosure is purged with dry nitrogen to ensure that the KN crystal remains above the dew point, even at −17°C. The cavity is set up in a bow-tie configuration of total length 405 mm with the focusing mirrors having a curvature of −50 mm. The input coupling mirror had a reflectivity of 97.5% at the fundamental wavelength. Around 28 mW of 843 nm light are incident on the cavity, with a coupling efficiency of 75%. This is focused to a waist of $2w_0$ = 24 μm inside the crystal, and produces up to 3 mW of frequency-doubled light. The length of the build-up cavity is stabilised to the laser wavelength using a Hänsch-Couillaud lock, which feeds back to a piezo stack on which one of the cavity mirrors is mounted (PZT3).

The Doppler-cooling transition in ^{88}Sr^{+} is only 440 MHz above the 5s ^{2}S$_{1/2}$ (F"=2)—6p ^{2}P$_{1/2}$ (F"=3) transition in ^{85}Rb [106]. The output light from the doubling cavity is double passed through a 270 MHz acousto-optic modulator (AOM) and the resultant down-shifted light is locked to a Rb cell using saturated absorption spectroscopy [82]. The error signal is fed back to the piezo in the tuneable reference cavity to which the ECDL is locked (PZT4). This provides an absolute atomic reference which guarantees long-term stability of the 422 nm light.

The 422 nm radiation output by this laser system is used for three purposes:

1) a far-detuned cooling beam to rapidly Doppler cool the hot ions after they are first created by photoionisation;

2) a near-resonant cooling beam to Doppler cool cold ions to close to the Doppler limit;

3) a σ^- polarised optical-pumping beam to prepare the ion in the ^{2}S$_{1/2}$ ($m_j = -1/2$) state in preparation for sideband cooling (details given in chapter 5).

The light from the doubling cavity passes twice through an AOM en route to the offset Rb lock. Some of the light is picked off after a single pass and used to provide the far-detuned cooling beam. This is overlapped with the near-resonant beam (Doppler-cooling beam #3 *c.f.* table 3.1) on a polarising beam splitter. The far-detuned light is switched using a mechanical shutter.

The near-resonant cooling beam is obtained by passing light from the doubling cavity through a 120 MHz AOM. The wavelength of this light can be tuned by varying the frequency of the double pass AOM to the Rb lock. The Doppler-cooling light is divided into three cooling beams of 25 μW each, which are focused to spots of $2w_0 = 100$ μm at the ion. The beam directions are chosen such that they are all at an angle of 29° with the X-axis of the trap (as defined in figure 3.1), and equidistantly spaced about a cone aligned with the X-axis. A single beam oblique to all three trap axes is sufficient to Doppler cool the ion. However all three beams are used to allow micromotion minimisation (see section 3.4.2) in three dimensions. The beam directions are summarised in table 3.1. The light is switched using both an AOM and a mechanical shutter. The AOM provides fast switching times and $\sim$33 dB extinction. The mechanical shutter, placed in the beam in front of a pin-hole, is slower but provides total extinction.

The σ^- polarised optical-pumping beam is created by picking off some light from the near-resonant Doppler-cooling beam, and passing it through a linear polariser and a quarter wave plate. The optical-pumping beam is aligned with the applied magnetic field (X-axis of the trap). This beam is switched using an AOM and a mechanical shutter.

3.3.4 1092 nm repumper laser

Light at 1092 nm is used to drive the 4d ^{2}D$_{3/2}$—5p ^{2}P$_{1/2}$ transition, to prevent the ion decaying to the otherwise dark ^{2}D$_{3/2}$ state and thereby being lost from the Doppler-cooling cycle. It is generated by a neodymium-doped fibre laser [82], illustrated in figure 3.5. An 825 nm diode (SDL-5421-G1) is coupled into a 6 m length of Nd^{3+}-doped optical fibre. The doped fibre

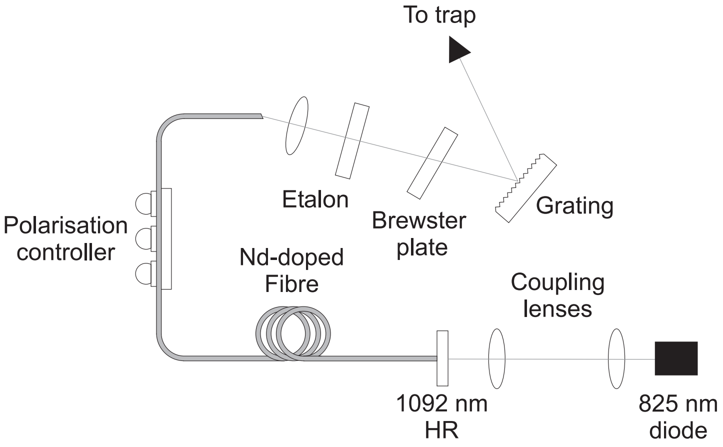

Figure 3.5: 1092 nm laser.

provides the active medium and the output of the fibre is incident on a grating (1200 lines/mm, 1μm blaze) at the Littrow angle (40.9°). The laser cavity comprises the length of the fibre, plus the distance to the feedback grating. The output of the laser consists of a large number of modes at 15 MHz intervals, under a $\sim$1.4 GHz wide envelope. The wavelength is set to 1091.786(1) nm using a wavemeter. The laser is not stabilised in any way, as when one mode drifts out of resonance with the atomic transition, the adjacent mode drifts into resonance. 2 mW of 1092 nm light are focused to a spot of $2w_0 = 560\ \mu$m, at the centre of the trap. Following the first pass through the trap (along the same line as Doppler-cooling beam #1), the repumper beam is redirected back through the trap along a different direction (along the same line as Doppler-cooling beam #2), and with a polarisation approximately orthogonal to the first, in order to prevent optical pumping into dark states (see section 3.4.3). The multimode nature of the repumper light prevents the fields of the two beams from simply coherently summing

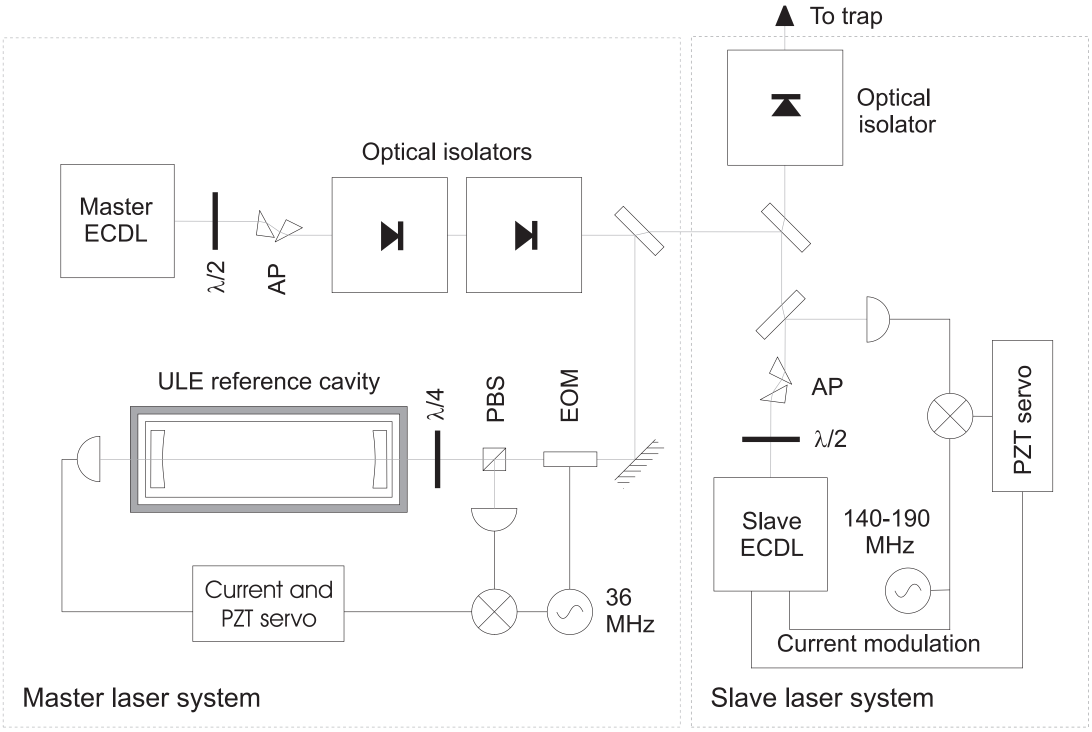

Figure 3.6: 674 nm laser. The master laser sideband injection locks a pair of slave lasers. For clarity only one of the slaves is shown.

to give a single effective polarisation. The beam directions are summarised in table 3.1. The beam is switched using an AOM and a mechanical shutter.

3.3.5 674 nm probe laser

Light at 674 nm is used to sideband cool the ion, and also perform spectroscopy, on the 5s $^2S_{1/2}$—4d $^2D_{5/2}$ quadrupole transition. The 674 nm laser system consists of three New Focus Vortex ECDLs in a master-slave arrangement, illustrated in figure 3.6. The master laser is stabilised to an ultra-low-drift resonator (free spectral range = 1.5 GHz, finesse = 1500) using the Pound-Drever-Hall technique [107], to realise a linewidth of $\Gamma/2\pi = 2$ kHz

[58, 94]. The master laser sideband injection locks a pair of slave lasers to create two narrow-linewidth sources that can be tuned independently across the $^2\mathrm{S}_{1/2}$—$^2\mathrm{D}_{5/2}$ transition. This arrangement provides:

1) a sideband-cooling beam with an interaction strength of $\Omega_0 = 2\pi\times$ 312 kHz (peak intensity $I_0 \approx$ 300 W/cm^2) on the 5s $^2\mathrm{S}_{1/2}$ ($m_j = -1/2$)—4d $^2\mathrm{D}_{5/2}$ ($m_j = -5/2$) transition;

2) a spectroscopy beam with an interaction strength of $\Omega_0 = 2\pi\times$ 110 kHz (peak intensity $I_0 \approx$ 10 W/cm^2) on the 5s $^2\mathrm{S}_{1/2}$ ($m_j = -1/2$)—4d $^2\mathrm{D}_{5/2}$ ($m_j = -1/2$) transition.

These two beams have antiparallel **k** vectors, inclined at 61° from the Z-axis of the trap (as defined in figure 3.1), and 29° to the X-axis (*c.f.* table 3.1). This results in a Lamb-Dicke parameter of $\eta_\mathrm{Z} = 0.018$. Both beams are switched using AOMs and mechanical shutters.

3.3.6 1033 nm quencher / clearout laser

Light at 1033 nm is used to shorten the lifetime of the 4d $^2\mathrm{D}_{5/2}$ state by coupling it to the 5p $^2\mathrm{P}_{3/2}$ level. This allows the ion to return rapidly to the ground state, and so closes the cooling cycle on a time scale short enough to allow effective resolved-sideband cooling. It is also used to clear out the $^2\mathrm{D}_{5/2}$ state during pulsed-probe spectroscopy of the $^2\mathrm{S}_{1/2}$—$^2\mathrm{D}_{5/2}$ transition. The light is produced by a diode in a Littrow configuration ECDL, the design of which is similar to that of the 922 nm laser described in section 3.3.1 and the 843 nm laser described in section 3.3.3.

1033 nm light from a laser diode (Toptica LD-1050-0050-AR-2) is collimated, and incident on a ruled grating (1200 lines/mm, 500 nm blaze, ∼6% feedback) at the Littrow angle (38.3°) to form a 40 mm long external cavity. The laser is stabilised to an invar cavity via a side-of-fringe lock, which reduces the drift to $\leq$60 MHz/h. The output 1033 nm light is divided into two beam paths.

For sideband cooling the quencher beam has intensity $I_0 = 5$ W/cm^2 and is red-detuned by $\simeq$300 MHz from the $^2\mathrm{D}_{5/2}$—$^2\mathrm{P}_{3/2}$ transition. This detuning is chosen to limit the variation in saturation parameter due to the quencher laser's frequency drift. The beam counter propagates to Doppler-cooling beam #3, as summarised in table 3.1. The quencher beam is switched using both an AOM and a mechanical shutter. The clearout beam has sufficient intensity to depopulate the $^2\mathrm{D}_{5/2}$ state within 2 μs. It is overlapped with the optical-pumping beam on a beam splitter (see table 3.1). The clearout beam is switched only by a mechanical shutter, as the exact switching time is not critical.

3.4 Loading an ion

Before cooling an ion to the motional ground state there are certain procedures which must be carried out to prepare the ion and the trap. Specifically, an ion must be loaded, the micromotion must be minimised, and any ambient **B**-fields must be nulled. These processes are now described in turn.

3.4.1 Loading

During the 10-year history of this experiment at NPL, three separate loading schemes have been used:

1) electron bombardment using a $SrAl_4$ oven source;
2) electron bombardment using a cleaner, SrO_2 combined oven and hotplate source;
3) photoionisation using the SrO_2 combined oven and hotplate source.

These methods are described here, and compared in chapter 4.

The first electron-bombardment method was employed between August 1999 and December 2002. While this usage predates the current work, it is instructive for comparison with the other loading methods. By this first method, Sr vapour was generated by an oven containing $SrAl_4$ and Ni powder [108]. No hotplate was used; the flux was incident on the trap directly from the oven. This required a different arrangement of the oven from that in figure 3.2, in which the oven was situated where the hotplate is shown in the figure. This source, however, was not particularly clean and could generate Al and Ni as well as Sr. Atoms created in this way were ionised by electron bombardment. For this, once the oven had reached a sufficiently high temperature to emit a significant flux of Sr, a current of 3.5 A was passed through the filament, which was biased at −35 V with respect to the DC-grounded trap electrodes. The Sr was then ionised by the high energy electrons emitted from the filament. The hotplate was also biased at −35 V, to ensure it did not attract the emitted electrons back towards itself, and away from the trapping region. The cooling laser was detuned ~250 MHz below line centre of the Doppler-cooling transition, and was incident on the trapping volume. The larger than usual detuning ($> \Gamma/2$) was used to more efficiently cool the hot ions. If an ion was trapped it could be detected by the light which was scattered on this transition.

The second method was employed between December 2002 and October 2004. By this method, the Sr was produced using an oven source and hotplate filter. Two ovens initially contained a high-purity mixture of $SrCO_3$ and Ta powders. These were heated to ~650°C for 24 hours to produce a SrO:Ta mixture. This process was completed with the vacuum chamber connected to a turbo pump, before the chamber was baked and pumped down to low pressure. The strontium was further reduced to form Sr and Ta_2O_5 by heating the ovens to ~800°C. The ovens were alternately heated to load an even coating of Sr on the tantalum hotplate. There was no line of sight between the oven apertures and the trap, so no material from the ovens could be evaporated from there onto the electrodes. The hotplate was ~20 mm from the trap, and was heated to temperatures in the range 220°C to 370°C by passing a current through it. This generated a Sr vapour in the trapping region, which could be ionised. The hotplate therefore acts as a vapour pressure filter and reduces the likelihood of impurities being evaporated towards the trap while loading: any impurity atoms with a vapour pressure significantly higher than that of elemental Sr are expelled from the hotplate on its first use, while impurities with significantly lower vapour pressures remain permanently on the hotplate, without ever being evaporated toward the trap. After a Sr reservoir had been deposited on the hotplate, the trap could be loaded many times before the reservoir had to be replenished. As in the first method, the strontium was ionised by electron bombardment. During loading, the Doppler-cooling laser was incident on the trapping volume and detuned ~250 MHz below line centre of the Doppler-cooling transition. If an ion has been trapped it can be detected by the light which is scattered on this transition.

The third loading method was employed from January 2005 to date. It uses the same combined oven source and hotplate filter to produce the atomic flux as described for method 2, except that the trap is loaded at very much lower hotplate temperatures: in the region of 120°C. The Sr atoms are photoionised using a resonant two-step process. This process is fully described in chapter 4. The atomic trajectory from the hotplate is at a mean angle of ~90° to the photoionisation beams, with the extended size of the hotplate source resulting in a spread of around ±10° in this angle. The most recent endcap trap has been loaded solely using this photoionisation method, and so the filaments are not, in principle, required. They have been included nonetheless, but never used.

3.4.2 Minimising micromotion

As described in section 2.3 the motion of an ion in an RF trap can be decomposed into a secular component, and a micromotion component. The micromotion is a driven component at the trap drive frequency, but provided the ion's mean position is at the RF null at the centre of the trap [81] and certain stability parameters are satisfied [60] the micromotion is generally small. Imperfections in the trap geometry, patch potentials due to uneven coating of the electrodes with Sr, or static charges which build up on insulators near the trap, can perturb the potential so that the ion is no longer at the RF null. This can lead to excess micromotion, which has the effect of adding RF sidebands to the atomic transitions' spectra. This complicates the observed spectra, and reduces the coupling strength of the probe laser with the ion. The micromotion must therefore be compensated for before the ion can be effectively cooled to the ground state. This compensation is achieved using an RF-photon correlation technique as follows [82].

By detuning the Doppler-cooling laser to be $\Gamma/2$ below resonance, the micromotion oscillations Doppler shift the ion closer to and further from resonance with the blue light. The scattered light from the ion therefore fluctuates in intensity with the same period as the trap drive, and with an amplitude related to the severity of the excess micromotion, as shown in figure 3.7. The position of the ion relative to the RF null can be adjusted by changing the voltages on the two compensation electrodes and on one of the outer endcap electrodes (figure 3.1). By iteratively minimising the observed fluctuations in scattered light from each of the three, non-coplanar Doppler-cooling beams in turn, the micromotion can be minimised. Figure 3.7 shows typical examples of the fluorescence modulation signal observed before and after micromotion minimisation. This procedure is simple, but time consuming; the full process can take up to half an hour. Unless the micromotion-compensation voltages required are stable over timescales very much longer than this, the experiment becomes unworkable. Instances of such a problem, and its solution are discussed in chapter 4.

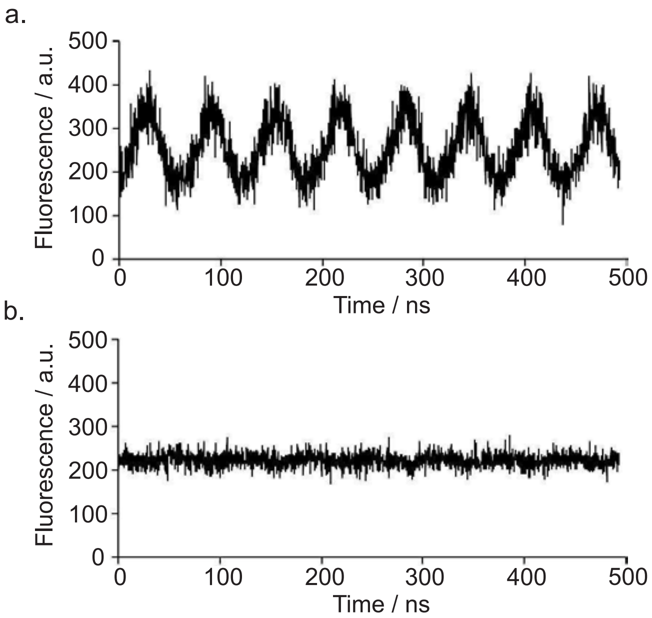

Figure 3.7: Typical examples of RF-photon correlation traces obtained by the RF-photon correlation technique. The fluorescence on the Doppler-cooling transition is recorded, triggered by the RF trap-drive voltage. The traces show the modulation (a) before and (b) after minimising the micromotion.

3.4.3 Zeroing the magnetic field

The implementation of sideband cooling used in this experiment drives a sideband of a particular Zeeman component of the $^2S_{1/2}$—$^2D_{5/2}$ transition (as outlined in chapter 2, and discussed fully in chapter 5). In order to resolve the otherwise degenerate Zeeman sublevels, a magnetic field of known amplitude and direction is applied to the ion. To do this, any ambient magnetic fields (such as from pieces of laboratory equipment, or the earth) must be nulled, and then an additional, known **B**-field applied. Two methods are used to zero the **B**-field; first coarsely, and then more sensitively.

Coarse zeroing of the **B**-field is achieved by minimising fluorescence on the Doppler-cooling transition. In an applied magnetic field, when the repumper light is not polarised parallel to this applied field, all Zeeman components of the $^2\mathrm{P}_{1/2}$—$^2\mathrm{D}_{3/2}$ are driven by the repumper laser [109]. In zero **B**-field one or more of the components is no longer driven, and the Doppler-cooling laser rapidly optically pumps the ion into a dark sub-level. Fluorescence on the cooling transition therefore goes to zero in zero **B**-field. By adjusting the current in the magnetic field coils so that the 422 nm fluorescence is minimised for two orthogonal polarisations of the repumper light, the magnetic field can be roughly set to zero. This method reduces the splitting of the $^2\mathrm{S}_{1/2}$—$^2\mathrm{D}_{5/2}$ quadrupole transition to ∼200 kHz. A more sensitive method of zeroing the magnetic field is to then minimise the splitting of this quadrupole transition. This minimisation is repeated for horizontal and vertical polarisations of the probe laser until the splitting is reduced to ∼40 kHz. This corresponds to a field of ∼2 μT. A field of 380 μT at the ion is then applied using the X magnetic-field coils.

3.5 Summary

This chapter has described the apparatus used to trap and cool a single $^{88}\mathrm{Sr}^+$ ion to the zero point of its motion. Such a state is a prerequisite for many QIP applications. Several parts of this apparatus were built during the course of this thesis work. The 922 nm ECDL, 461 nm doubling cavity, and 405 nm photoionisation laser were all designed and built so that a new photoionisation scheme could be implemented (described fully in chapter 4).

Implementation of this scheme was a prerequisite for the low trap heating rates which allowed the zero-point cooling results reported in chapter 5 to be taken. Subsequently the 922 nm ECDL design was modified to improve the pre-existing 844 nm and 1033 nm lasers. These replacement lasers have proved more stable than the earlier versions, and allow easier running of the experiment. Most recently, a pre-existing 422 nm doubling cavity has been replaced with the new design reported here. The compact, monolithic, temperature controlled design of the housing is expected to significantly reduce the drift of the system over the course of an experimental run. This chapter has also described the basic procedures required to load a single $^{88}\mathrm{Sr}^{+}$ ion into the endcap trap, and prepare the apparatus for the cooling procedures described in chapter 5.

CHAPTER 4

Photoionisation

4.1 Introduction

This chapter describes the implementation of a two-step, resonant photoionisation scheme to produce $^{88}\mathrm{Sr}^+$ for precision ion-trap experiments. One of the significant advantages of ion traps for precision experiments—such as metrology and QIP—is that the ions are well isolated, and largely unperturbed by external influences. Several ion-trap experiments [15, 72, 97, 110] including the experiment described in this thesis [93] have encountered problems with degraded trap performance directly or indirectly related to the traditional trap loading method of electron bombardment (EB). These problems are thought to be exacerbated by impurities in the atomic source used for loading [97]. The degradation in performance—specifically the very high heating rates and the time taken to adequately minimise the micromotion—renders many precision experiments, particularly QIP applications, unworkable.

Photoionisation loading of ion traps has been reported as an alternative loading method with several elements, namely Mg [111] Ca [111–113], Cd [114], and Sr [115]. This chapter presents a demonstration of clean, efficient and controlled photoionisation loading of $^{88}\mathrm{Sr}^{+}$, together with quantitative measures of its benefits. Similar to the observations of Gulde *et al.* [112] and Lucas *et al.* [113], (but in apparent contrast to the work of Vant *et al.* [115]) we demonstrate a $\sim 10^4$-fold reduction in the atomic beam flux when compared to EB loading. Moreover we observe a significant reduction in the variation of excess micromotion. In addition to the improvements due to photoionisation loading, this chapter also presents and quantifies the improvement in trap operation observed following the introduction of a pure atomic source of Sr using a two-step evaporation process.

This chapter is arranged as follows. The loading methods of electron bombardment and photoionisation are reviewed in section 4.2. The relative merits of several possible photoionisation schemes are described in section 4.3, and the scheme chosen for this work is highlighted. The factors affecting the photoionisation rate in the chosen scheme are outlined in section 4.4. Section 4.5 describes the experimental details of the loading methods used in this experiment (historically electron bombardment and latterly photoionisation). The trap behaviour resulting from these loading methods is compared in section 4.6. Further work is proposed in section 4.7.

4.2 Critical review of loading methods

4.2.1 Principal loading methods

The traditionally used method of creating singly-charged, positive ions for ion-trapping experiments is electron bombardment (EB) of neutral atoms. To form ions in this manner, a flux of atoms passing through the trapping volume is bombarded by energetic electrons emitted from a nearby filament. If an atom of sufficiently low energy is ionised within the trapping volume then it is trapped.

More recently, some ion-trapping experiments have used photoionisation to create ions. By this method, atoms passing through the trapping volume are excited either resonantly or non-resonantly, by one or several photons. If an atom of sufficiently low energy is ionised in the trapping volume then it is trapped.

4.2.2 Problems with electron-bombardment loading

Precision ion-trap experiments rely on the fact that the trap provides a well-controlled, harmonic trapping potential, with minimal undesired external perturbations. Previous work suggests that the high atomic flux required for EB loading causes problems with patch potentials on the electrode surfaces [97, 110]. Even on clean electrodes, surface fields arise from non-uniform spatial variations in the electrode material work-function. Such non-uniformities occur at the edges of crystal grain boundaries. In addition to this, they can be caused by chemically adsorbed materials on the electrodes; by Van der

Waals forces between the electrodes and contaminants; and by contact potentials between the electrode material and regions of material evaporated from the experiment's atomic source [96]. Due to unavoidable interactions with its environment, a trapped ion will be heated by various sources, including stochastic fluctuations in the electric field due to electric-field noise from the trap electrodes. The observed scaling behaviour of the ion-heating rate with the ion-electrode separation suggests that the heating is not due to spatially uniform noise sources on the electrodes (such as Johnson noise) but rather due to an uncorrelated noise source (such as fluctuating patch-potential fields) [110].

This heating (termed "anomalous heating") occurs in a large variety of experiments. It has been observed in traps with electrodes made of beryllium [97, 110], molybdenum [72, 110, 116, 117], tantalum [94], tungsten [66], gold [50, 72, 110] and gallium arsenide [71]. The traps have a range of ion-electrode separations from 30 μm [71] to 600 μm [117], and a variety of trap geometries, including linear traps [50, 71, 72], ring traps [72, 97, 116] and endcap traps [94]. Anomalous heating of ions is believed to be thermally activated, and has been reduced by an order of magnitude by cooling the trap electrodes to 150 K [66], but otherwise appears to be ubiquitous. Despite this baseline due to the microscopic structure of the electrodes, heating from patch potentials can be exacerbated by impurity atoms [96] such as those evaporated onto the electrodes during loading [97].

Many trapped-ion quantum-computing algorithms use the ions' motional state as a qubit, *e.g.* the Cirac-Zoller C-NOT gate [44, 45], Deutsch-Jozsa algorithm [20], and teleportation [23]. Significant heating during the implementation of such algorithms can destroy motional coherence and render the algorithm unworkable. Even algorithms which are not directly dependent on the motional qubit, *e.g.* [118], cannot be carried out if heating is excessive. For this reason, any ion-heating mechanism which can be reduced or removed is useful for QIP applications.

In addition to these heating problems, some of the charge emitted from the filament during EB loading accumulates as static charge on insulating surfaces near to the trapping region. This can displace the ion from the RF null and so causes excess micromotion [81, 82], which requires frequent compensation as the static charge drifts over time. If left uncompensated, micromotion can lead to reduced laser-ion coupling and increased ion-heating rates, as discussed in section 2.3.4. With time, the micromotion-compensation voltages required can fluctuate erratically and with increasing amplitude, to a point where the corrections required become prohibitively difficult [93, 97].

4.2.3 Advantages of photoionisation loading

In recent years, photoionisation techniques have been developed for ion-trap loading [111–115] in order to avoid these significant problems arising from EB loading. Photoionisation investigations using calcium [112, 113] have shown dramatic reductions in the atomic flux required to load a trap. This should significantly reduce the flux-associated patch potentials thought to be responsible for the ions' anomalous heating rates, and subsequent degradation of trap performance over time. A reduction in the fluctuations of applied micromotion-compensation voltages when compared to EB loading

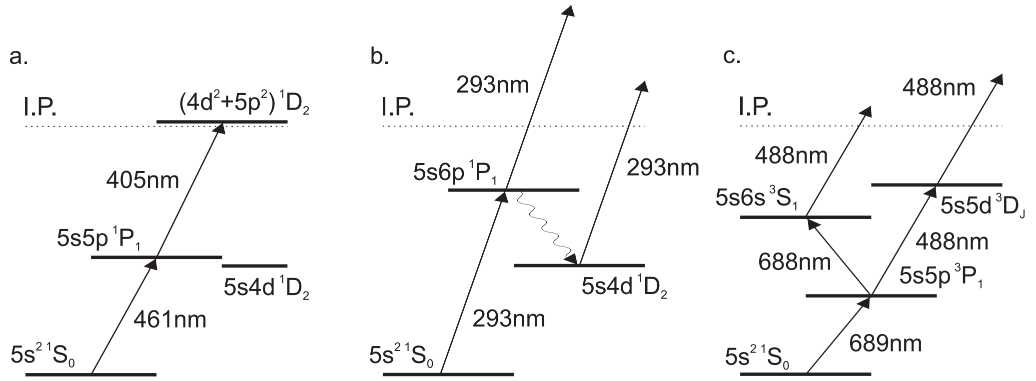

Figure 4.1: Energy levels in Sr. This work follows the path shown in (a) whereby neutral Sr is photoionised by excitation of the $5s^2\ ^1S_0$—$5s5p\ ^1P_1$ dipole transition at 461 nm, followed by excitation to the $(4d^2+5p^2)\ ^1D_2$ autoionising state with 405 nm light [93]. Photoionisation has been achieved in Ca using a path analogous to that shown in (b) [111]. Photoionisation of rare Sr isotopes has been carried out using the path shown in (c) [122].

is also observed [113], as would be expected given that photoionisation adds little or no charge to the system.

4.3 Sr photoionisation scheme

There are several reports in the literature of using Sr photoionisation as a spectroscopic tool e.g. [53, 119–124]. Photoionisation for the purpose of loading ion traps has been reported for Ca [111–113], which has a similar electronic structure to Sr. The energy levels for three possible photoionisation paths for Sr are shown in figure 4.1.

In the path shown in figure 4.1a, neutral Sr is photoionised by excitation of the $5s^2\ ^1S_0$—$5s5p\ ^1P_1$ dipole transition at 461 nm, followed by excitation to the $(4d^2+5p^2)\ ^1D_2$ autoionising state with 405 nm light. The autoionising state is doubly excited, so that each excited electron is bound, but their combined energy is greater than the first ionisation potential (IP). From here, one electron returns rapidly to the ground state and the other is ejected into the continuum. It is in principle possible that the atom could decay from the $^1P_1$ state to the lower-lying 5s5d $^1D_2$ state. However, the transition probability for this is sufficiently low that the effect would be negligible [52, 125]. The radiations required for this route are straightforward to obtain: one directly with a diode laser (405 nm), the other by a frequency-doubled diode laser (461 nm). A full description of these lasers is given in chapter 3. Photoionisation via similar pathways to this in Ca have been demonstrated by Gulde *et al.* [112] and Lucas *et al.* [113]. The second step in the pathway used by Gulde *et al.*, however, did not excite the electron into the continuum, but rather into a Rydberg state, from which the strong electric fields in the trap were sufficient to subsequently ionise it. The second step used by Lucas *et al.* excited the electron into the continuum to an energy which may be close to an autoionising level, though the position of the autoionising states in Ca—and hence how close this excitation is to resonance—is not well known. By contrast, the well documented ($4d^2+5p^2$) $^1D_2$ level in Sr [53, 56, 120, 121, 124, 126–128] is known to have a very large cross section (5,600 Mbn, where $1\ \mathrm{bn} = 10^{-28}\ \mathrm{m}^2$) and a broad natural linewidth (∼1 nm) due to its very short lifetime. It has been shown that photoionisation of Ca does not require that the transition from the $^1P_1$ state to the continuum be driven by a coherent, narrow linewidth source; light from an LED is sufficient [113]. Fortuitously, 405 nm is the chosen wavelength for Blu-Ray and HD-DVD data storage media. Laser diodes around this wavelength with output powers of tens of milliwatts are therefore standardly available. Given the possibility of a doubly resonant process, which can be realised using diode-laser-based sources, this is the route chosen for this work.

While this path seems the simplest approach for precision ion-trap experiments, it is not the only possible route. The path shown in figure 4.1b (analogous to that used by Kjærgaard *et al.* [111] to photoionise Ca) requires ultra-violet (UV) laser radiation for excitation. Sources at similar wavelengths have been produced by a number of methods. These include: frequency-doubled dye lasers [111]; frequency-tripled Ti:Sapphire lasers [129]; sum-frequency mixing of YAG and diode lasers [130]; and sum-frequency mixing, followed by frequency doubling of diode sources [131, 132]. Given the requirements of photoionisation, two reasonable methods for producing a few milliwatts of 293 nm light were found.

The first method required sum-frequency mixing of 532 nm light from a frequency-doubled YAG laser with 652 nm light from a diode source, using critically phase matched ($\theta = 41.5°$) Beta Barium Borate (BBO) in a doubly-resonant cavity. A second option required sum-frequency mixing of 1064 nm light from a YAG laser with 405 nm light from a diode source, using critically phase matched ($\phi = 51.3°$) Lithium Triborate (LBO) in a doubly-resonant cavity. Both methods are expensive and experimentally demanding compared to generation of the radiations required for the route illustrated in figure 4.1a. The main expenses in both cases were the purchase of a YAG laser and obtaining cavity mirror coatings with reflectivities specified over such a broad range of wavelengths (UV and infrared). Additionally, it is desirable to be able to fibre-couple light to the trap. Existing commercial fibres are generally

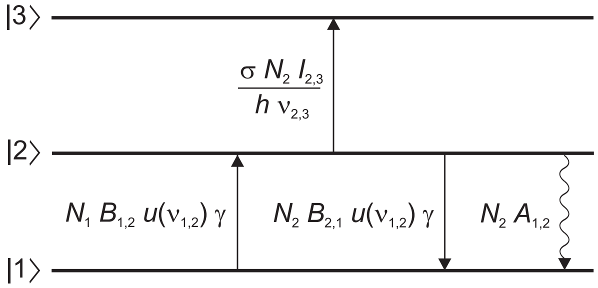

Figure 4.2: Transition rates for photoionisation. The electron is excited from $|1\rangle \rightarrow |2\rangle$ via absorption of a photon, and back from $|2\rangle \rightarrow |1\rangle$ via both stimulated and spontaneous emission. It can be excited from $|2\rangle \rightarrow |3\rangle$ via absorption, and is then lost from the system sufficiently rapidly that it cannot be returned to the lower levels.

designed for carrying longer (visible and infrared) wavelengths. While it is possible to fibre-couple 293 nm light, it is more difficult and more expensive than the fibre-coupling of visible radiations.

The path shown in figure 4.1c is that used by Bushaw and Cannon [122] for selectively ionising the unstable isotope ^{90}Sr. Isotope shifts in this route are favourable for such a purpose, although it requires three separate laser wavelengths, and its rate is limited by the nominally spin-forbidden first step. It is therefore non-ideal for use with more common isotopes.

4.4 Photoionisation rate

Having outlined the excitation path used for photoionising Sr, this section details the parameters relevant to the photoionisation rate. It also estimates the expected photoionisation rate, given reasonable experimental parameters, and shows that these are acceptable for the purpose of trap loading.

A Sr atom can be modelled as the three-level system shown in figure 4.2. The atom is excited from $|1\rangle \rightarrow |2\rangle$ via absorption of 461 nm radiation, which has an energy density per unit frequency of $u(\nu_{1,2})$, where $B_{1,2} = A_{1,2}\lambda^3/8\pi h$ is the Einstein B coefficient for the transition, γ is the linewidth of the 461 nm laser (assumed to be around 100 kHz), and h is Planck's constant. It can also be de-excited from $|2\rangle \rightarrow |1\rangle$ via both stimulated and spontaneous emission, where the Einstein A coefficient, $A_{1,2}$, is 2.1 × 10^8 s^{-1} [52]. The ion can be excited from $|2\rangle \rightarrow |3\rangle$ via absorption of 405 nm light of intensity $I_{2,3}$. The transition cross section, σ, is 5,600 Mbn centred at 405.2 nm, with a width of 0.9 nm, [56] and references therein. Upon ionisation the electron is lost from the system under consideration, and so cannot be driven back to level $|2\rangle$. The populations of the three levels, N_i (i = 1,2,3), can be described by three coupled, linear, ordinary differential equations:

$$\begin{aligned}
\frac{d}{dt}N_1 &= -N_1\ B_{1,2}\ u(\nu_{1,2})\gamma + N_2\left[\qquad B_{1,2}\ u(\nu_{1,2})\gamma + A_{1,2}\right], \\
\frac{d}{dt}N_2 &= N_1\ B_{1,2}\ u(\nu_{1,2})\gamma - N_2\left[\frac{\sigma I_{2,3}}{h\nu_{2,3}} + B_{1,2}\ u(\nu_{1,2})\gamma + A_{1,2}\right], \\
\frac{d}{dt}N_3 &= N_2\ \frac{\sigma I_{2,3}}{h\nu_{2,3}},
\end{aligned} \tag{4.1}$$

where at time $t = 0$: $N_2 = N_3 = 0$, and $N_1 = P$, the number of particles. Only the initial behaviour of the system must be considered as the characteristic times for excitation are long compared to the transit time of a hot atom through the photoionisation laser beams. Equation 4.1 can be solved analytically [133] for $N_3(t)$.

The partial pressure of Sr at the hotplate, and so the flux of atoms through the trapping region, increases exponentially with temperature. Specifically, for strontium the partial pressure in torr, P_{mm}, varies with the temperature in kelvin, T, as [134]:

$$Log_{10} P_{\mathrm{mm}} = 7.735 - \frac{7548}{T}, \tag{4.2}$$

where 1 torr $\simeq$ 1.33 mbar. To estimate the photoionisation rate, it is assumed that the atoms from the hotplate travel through the photoionisation beam, approximately at right angles to the beam (*c.f.* figure 4.3), and so Doppler shifts have been neglected. The atoms are then assumed to all travel at the most probable speed of a thermal velocity distribution. For 1 mW of light on resonance at 461 nm and 7 mW of light at 404 nm, with each beam focused to a spot of $2w_0 = 200$ μm at the trap centre (∼20 mm from the hotplate), it is calculated that an ionisation rate of several events per second is reached, once the hotplate is at a temperature of 120°C. All of these parameters are reasonable to achieve experimentally, and this ionisation rate is acceptable for loading single ions into a trap.

Several parameters could, in principle, be optimised for this process. For example, reducing the spot size of the photoionisation lasers increases the energy density, u. However, it also reduces the amount of time an ion of a particular velocity will spend in the radiation field, and reduces the total number of atoms which will pass through the beam focus, for a given partial pressure. Given the uncertainty in such experimental parameters as the area of the hotplate covered by Sr, no great effort has been made to further optimise the photoionisation parameters. It was also deemed unnecessary given the acceptable loading rate and the already-significant anticipated reduction in flux.

4.5 Loading methods used

During the 10-year history of the experiment described here, three separate loading schemes have been used:

1) electron bombardment using a $SrAl_4$ oven source;
2) electron bombardment using a cleaner, SrO_2 combined oven-and-hotplate source;
3) photoionisation using the SrO_2 combined oven-and-hotplate source.

For each loading method the majority of the additional apparatus (lasers, ion trap, vacuum chamber *etc.*) has remained unchanged, and is described fully in chapter 3. To summarise, however, the ion is cooled by 422 nm light produced by a frequency-doubled diode laser. A neodymium-doped fibre laser generates light at 1092 nm to ensure that the ion is not lost from the cooling cycle. The trapping potential is provided by applying an RF voltage (amplitude $V_0 = 390$ V; frequency $\Omega_{\mathrm{T}}/2\pi = 15.9$ MHz) to an endcap trap with an ion-electrode separation of 280 μm. This yields axial and radial motional frequencies of $\omega_{\mathrm{Z}}/2\pi \simeq 3.8$ MHz and $\omega_{\mathrm{r}}/2\pi \simeq 2.0$ MHz respectively. An ion is detected by focusing the near-resonant 422 nm photons scattered by it onto a photomultiplier tube. The trap is enclosed in a vacuum chamber at a pressure below 2×10^{-11} mbar.

4.5.1 Electron-bombardment loading

By the first EB-loading method, Sr vapour was generated by an oven containing $SrAl_4$ and Ni powder [108]. This process is described in section 3.4.1 However, this source was not particularly clean and generated Al and Ni as well as Sr; these other metals are thought to exacerbate anomalous heating rates [96, 97].

By the second EB-loading method, Sr vapour was generated using an oven and hotplate arrangement, analogous to that used in Ba by DeVoe and Kurtsiefer [97]. A photograph of the apparatus is shown in figure 3.2. For clarity, orientation of the oven and hotplate setup relative to the photoionisation laser beams is drawn schematically in figure 4.3. The loading procedure is fully described in section 3.4.1. While this loading method used a cleaner source of Sr than the previous method, it still required electron-bombardment ionisation, and incurred the experimental difficulties associated with high atomic flux and stray static charge described above.

4.5.2 Photoionisation loading

The photoionisation loading method uses the same combined oven source and hotplate filter to produce the atomic flux as described above, except that the trap is loaded at very much lower hotplate temperatures: in the region of 120°C. The Sr atoms were ionised using the photoionisation scheme outlined in section 4.3. In this scheme the ion is excited by 461 nm radiation resonant with the ${}^1S_0$—${}^1P_1$ transition. From here it is resonantly excited to the ($4d^2$+$5p^2$) ${}^1D_2$ autoionising state by 405 nm radiation. A pulsed

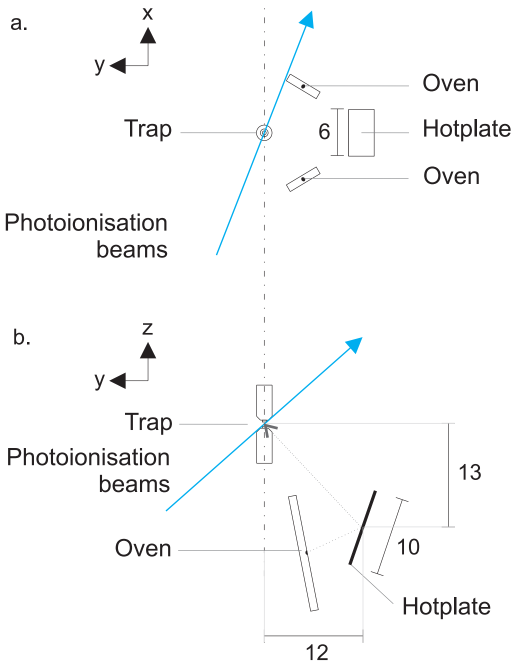

Figure 4.3: Schematic of oven and hotplate system. The relative positions of the ovens, hotplate and trap are shown, as well as the direction of the photoionisation beams through the trap (projected onto the plane shown).

photoionisation loading procedure is employed to enable the hotplate to be turned off as soon as possible after an atom is ionised. This ensures that only the minimum atomic flux necessary is used.

When the atom is first ionised in the trapping region it is still hot and the cooling transition is Doppler-shifted by the ion's motion, resulting in inefficient cooling by a standard Doppler-cooling laser with detuning $\Delta = -\Gamma/2$. If the ion is not rapidly cooled, it takes longer to detect its presence, delaying the time at which the hotplate can be turned off, and so increasing the amount of unnecessary flux evaporated towards the trap. To improve the efficiency of initial cooling, an additional Doppler-cooling beam, further red-detuned, is used to address the higher velocity of the hot ion. The initial velocity of the ion determines the optimal detuning of the off-resonant beam. For the ion loading temperatures used in this experiment a detuning of around $\Delta = -9\Gamma$ was used. Calculations by Guido Wilpers show that when this additional off-resonant beam is present, an ion from the hotplate experiences a more significant deceleration at all relevant velocities, and is slowed much more rapidly than it is by the near-resonant cooling beam alone. The results of this calculation are illustrated in figure 4.4. The ion can thus be detected much sooner after it is trapped. Given that the Sr flux increases exponentially with temperature, this faster detection can significantly reduce the amount of unnecessary flux evaporated towards the trap electrodes.

The loading process proceeds by alternating between periods of photoionisation and detection. This is illustrated schematically in figure 4.5. During the 70 ms photoionisation period, the 461 nm and 405 nm photoionisation lasers are incident on the trapping volume, as are the off-resonant and near-resonant cooling beams to rapidly cool any ions which are produced. To allow detection of the ion with the minimum amount of background scatter, the off-resonant laser and photoionisation lasers are blocked during the 30 ms detection period. If the photomultiplier detects a count rate above a certain threshold during this period it is due to scattering of the near-resonant 422 nm light, and is taken to infer the presence of a cold Sr^+ ion. Once this ion signal has been detected, the Sr source is turned off.

An ion is typically loaded after $\sim$40 s, at which point the hotplate temperature is $\sim$120°C, and increasing at a rate of $\sim$1.5°/s. From eq. 4.2 this means that at the time an ion is loaded, the partial pressure—and hence

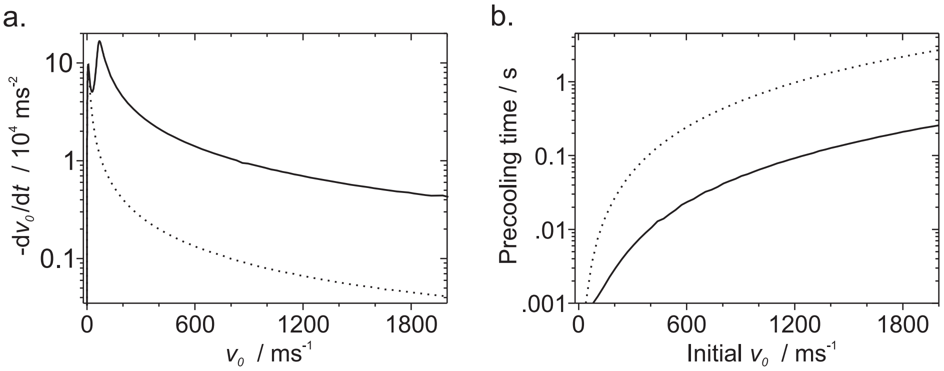

Figure 4.4: Calculated effect of an additional off-resonant cooling beam. (a) The rate of change of an ion's velocity amplitude, $\mathrm{d}v_0/\mathrm{d}t$, as a function of velocity amplitude, v_0. If only the near-resonant cooling beam is used (dotted) then an ion with $v \gtrsim 300\ \mathrm{ms}^{-1}$ is inefficiently cooled. With an additional cooling beam ($\Delta = -9\Gamma$, with 10 times the intensity of the near-resonant cooling beam), the ion is more efficiently cooled over the relevant velocity range (solid). (b) Time taken to cool an ion so that it scatters sufficient near-resonant photons to be detected ($v \lesssim 5\ \mathrm{ms}^{-1}$), as a function of the initial amplitude of the ion's velocity. When only the near-resonant beam is used (dotted) the precooling time is around 10 times longer than with both beams (solid).

the flux of Sr from the hotplate towards the trap—doubles approximately once every 5 seconds. The 100 ms photoionisation-detection cycle means that detection of the ion is fast compared to this timescale, thereby ensuring that a minimum of Sr is evaporated towards the trap electrodes. As the photoionisation-detection duty cycle is more rapid than the expected loading rate of a few events per second (section 4.4), there is a low probability that multiple ions are trapped during a single cycle.

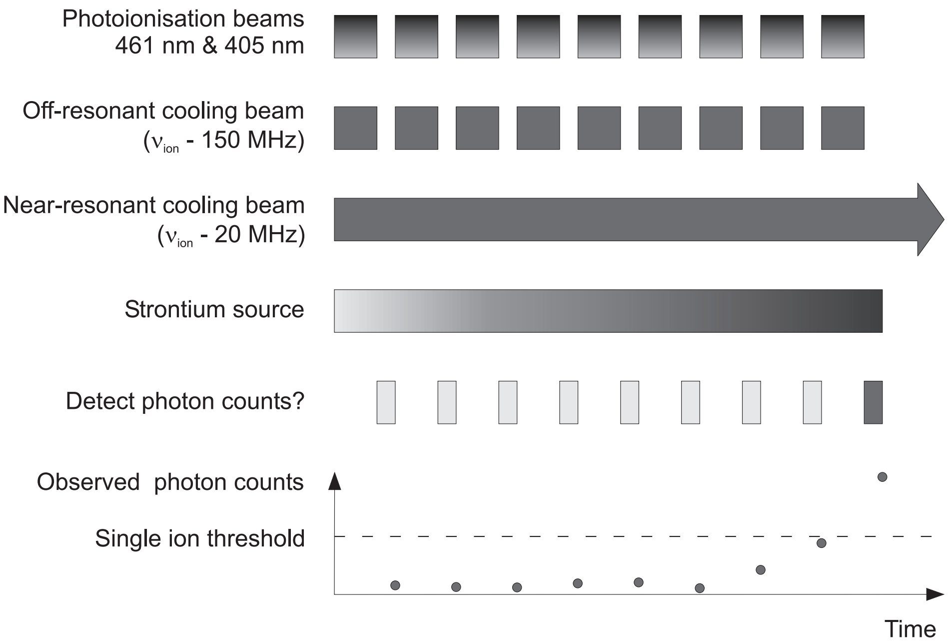

Figure 4.5: Timing of lasers for PI loading.

4.6 Results

Reliable, controlled photoionisation of $^{88}\mathrm{Sr}^{+}$ has been achieved for loading single ions into an ion trap. This has been demonstrated to require a substantially lower atomic flux than EB loading, and greatly reduce the variation in the voltages required to compensate micromotion.

4.6.1 Comparison of loading behaviour

Using photoionisation, single ions can typically be loaded at hotplate temperatures in the range 90°C to 140°C (average of 120°C over 70 loads) corresponding to a Sr partial pressure of $\sim 1 \times 10^{-13}$ mbar [134]. The hotplate is turned off if the temperature measured by the thermocouple rises above

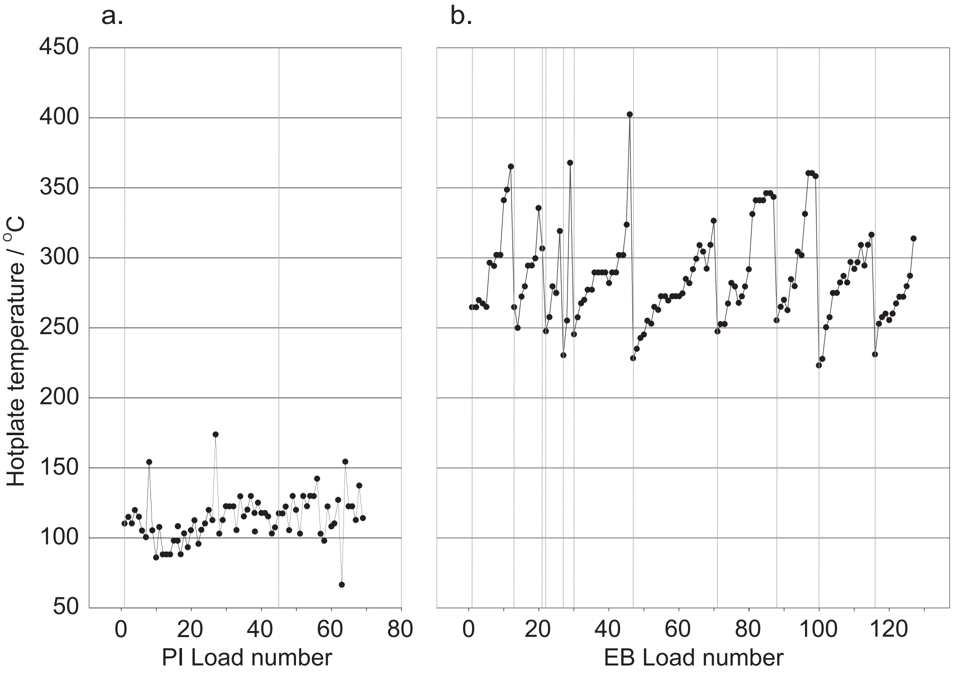

Figure 4.6: Hotplate temperature at which an ion is loaded as a function of the number of loads, for EB and photoionisation loading. The points at which the hotplate was replenished from the oven are indicated with a vertical grey line.

160°C without an ion having been loaded, although this occurs on < 10% of attempts. The hotplate temperature required to load the trap as a function of the number of successful loads using photoionisation is shown in figure 4.6a. The hotplate was replenished once during this time, although there is no indication that the Sr on the hotplate was significantly depleted by the loading process.

This contrasts sharply with the loading requirements when using EB, for which the hotplate typically needed to be run at temperatures above 220°C (Sr partial pressure of 3×10^{-9} mbar). The hotplate was turned off if its temperature rose too high without having loaded an ion, which

	Electron Bombardment	Photo-ionisation	Units
Loading temperature	220	120	°C
Sr partial pressure	3×10^{-9}	1×10^{-13}	mbar
Observed loading efficiency # loads / # attempts	~ 0.3	~ 0.9	

Table 4.1: Comparison of electron bombardment and photoionisation loading methods.

occurred on ∼70% of attempts. The hotplate temperature required to load the trap as a function of the number of successful loads using EB is shown in figure 4.6b. Over several EB loads the hotplate reservoir became depleted and the loading temperature required increased to ∼370°C. The hotplate ultimately needed to be replenished after around 16 successful trap loads (and 35 unsuccessful attempts). It is thought that the required increase in temperature over successive loads with electron bombardment may be due to inhomogeneous coating of strontium on the hotplate. As strontium is evaporated, the coating may become patchy, and so higher temperatures are required to obtain the same partial pressure of Sr at the trap.

A comparison of the effectiveness of the two loading methods is summarised in table 4.1. As the atomic flux through the trapping region is proportional to the partial pressure at the hotplate, it can thus be seen that photoionisation loading requires $\sim 10^4$ times lower atomic flux than EB loading, and loads more reliably.

4.6.2 Comparison of micromotion behaviour

To minimise micromotion in three dimensions, DC compensation voltages can be applied to three electrodes (compensation electrodes #1 and #2, and an outer endcap electrode, *c.f.* figure 3.1). Variations in excess micromotion behaviour can be quantified by the variation in the compensation voltages required to minimise the micromotion. Figure 4.7 illustrates this for each of the three compensation electrodes, for three periods of data taking; one period for each type of loading.

The original oven system, using EB loading, lead to significant variations in the required compensation voltages, which could change by several volts within a single day (figure 4.7d–e). The new oven system using SrO:Ta (but still using EB ionisation) introduces fewer impurities to the trap electrodes than the original oven system. Comparing figures 4.7i) and 4.7ii) clearly demonstrates the significant reduction (around a factor of 3) in the variation of required compensation voltages when using this new system. However, even with the improved oven, there remain significant variations from load to load. As photoionisation introduces little additional charge into the trapping region, the use of photoionisation loading reduces the variation still further (figure 4.7iii)). It is noted firstly that the amplitude of the day-to-day variation is reduced by over an order of magnitude when using photoionisation. Secondly, the required compensation voltages vary smoothly, in stark contrast to operation when using EB loading.

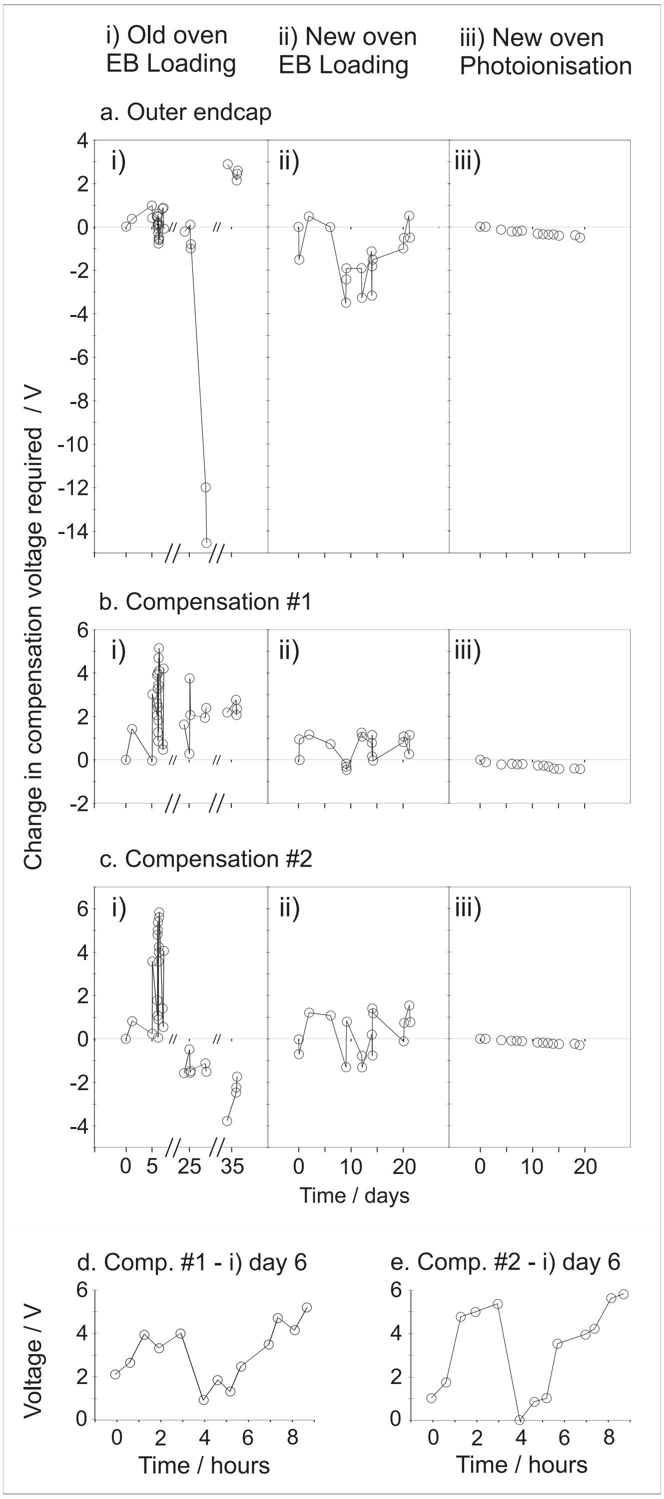

Figure 4.7: Effect of loading method on micromotion. To compensate micromotion in three dimensions, voltages must be applied to three electrodes. The change in compensation voltage required from the start of an experiment for each electrode is shown in (a)-(c), for three periods of data taking. In the different periods i) used the old $SrAl_4$:Ni oven and the atoms were ionised by electron bombardment; ii) used the new SrO:Ta oven with a hotplate filter, with EB ionisation; iii) used the new oven and hotplate with photoionisation. In period i) the compensation voltage required would fluctuate by several volts over the course of a single day. To illustrate this, figures (d) and (e) show the data from day 6 of (b)i and (c)i respectively. During this day a single ion was continuously trapped, without re-loading the trap at any time.

4.6.3 Comparison of heating behaviour

One of the significant motivations for implementing photoionisation loading is to reduce the large heating rates seen in systems loaded by EB methods; low heating rates are a prerequisite for almost all scalable trapped-ion quantum-computing applications. This expected reduction was observed, and is described fully in chapter 5.

4.6.4 Comparison with other atomic species

Some experiments have reported an increase in heating rate and a degradation in trap performance over time; this limitation is assumed to be due to fluctuating patch potentials caused by atomic vapour coating the trap electrodes. The most notable examples are those using Be [110] and Ba [97]. In contrast there are also examples of systems that do not exhibit this feature, specifically those with Ca [135] and Cd [72]. Earlier work at NPL (prior to this thesis work) saw the performance of an endcap trap for Sr degrade. Specifically it was observed that:

1) the required micromotion-compensation voltages fluctuated erratically and with increasing amplitude,

2) there was an associated increase in heating rate.

Only after having constructed a trap that was exclusively loaded by photoionisation (and hence was exposed to minimal atomic flux) [93] was it possible to observe the reduction in micromotion described here, and the low heating rates presented in chapter 5. While the dependence of trap performance on atomic species is not understood, Sr deposition on trap electrodes does appear to adversely affect trap operation over time.

4.7 Further work

The work described here requires only the loading of single $^{88}\mathrm{Sr}^{+}$ ions (naturally 82.6% abundant). However, trapping of odd-isotopes allows advantage to be taken of the very long coherence time of the ground state's hyperfine structure, and is therefore potentially interesting for QIP experiments [136]. The most abundant odd isotope (^{87}Sr) is only 7.0% abundant naturally. To load long, isotopically pure ion strings of such an isotope would therefore require isotope selectivity. Photoionisation work in Ca [112, 113, 137] has demonstrated isotopic selectivity using similar pathways to those used here in Sr. Although the isotope shifts in Sr are smaller than in Ca, there is a 56 MHz shift in the $^{1}\mathrm{S}_{0}$—$^{1}\mathrm{P}_{1}$ transition between ^{88}Sr and ^{87}Sr [138]. This compares to the smallest shift in the same transition in Ca of 154 MHz between ^{43}Ca and ^{44}Ca. (It should however be noted that when photoionising ^{43}Ca the most significant impurity contribution is from ^{40}Ca, centred 612 MHz away [113].) The spectrum in ^{87}Sr is complicated by a hyperfine splitting spanning 60 MHz [139]. Nonetheless, as the natural linewidth of the transition in Sr is 32 MHz [139] isotope selectivity should be realisable, provided Doppler and power broadening of the transition are minimised.

In the present experiment, this system is used to load single ions. The principle could easily be extended to load several ions deterministically into a linear trap. This will become an important capability in the new, linear trap, discussed in chapters 6–7.

4.8 Summary

The functioning of an ion trap can be compromised by a variety of issues arising from the loading method. These difficulties can be largely avoided by using a pure atomic source, and minimising the amount of stray charge and atomic flux incident on the trap during loading.

This chapter has presented a method for clean, efficient, and controlled photoionisation loading of strontium for precision ion-trap experiments. The two-step photoionisation proceeds via the $5s^2\ ^1S_0$—$5s5p\ ^1P_1$ dipole transition ($\lambda = 461$ nm), and is immediately followed by direct excitation to the $(4d^2{+}5p^2)\ ^1D_2$ autoionising state ($\lambda = 405$ nm). A frequency-doubled diode laser generates the 461 nm radiation and a free-running diode at 404 nm is sufficient to excite the 0.9 nm-wide transition to ionisation. These relatively simple laser sources render this a straightforward method for creating $^{88}Sr^+$ ions. Once an ion is created, near-resonant and far-detuned cooling beams facilitate rapid cooling to the Doppler limit; at this point the ion can be detected easily and the atomic source switched off, thus helping to minimise the atomic flux evaporated towards the trap electrodes.

Using this photoionisation method, the atomic flux required to load the trap is $\sim 10^4$ times less than when using electron bombardment. This compares very well with other similar implementations of photoionisation in the literature [112, 113]. Using photoionisation, we observe a trap loading success rate of >90%, which contrasts sharply with ~30% using EB loading. A further advantage of photoionisation is that it substantially reduces the variation in charge on insulating surfaces during the experiment: the day-to-day fluctuations of micromotion-compensation voltages are reduced by a factor of $\sim$10. Finally, using a clean trap which has only been loaded by photoionisation allowed a low ion-heating rate to be obtained. This is discussed in full in chapter 5.

CHAPTER 5

Zero-point cooling

5.1 Introduction

Trapped ions are now regarded as a credible physical system for the future realisation of a quantum information processor [140]. The universal set of gates proposed by Cirac and Zoller [44, 45] requires a linear string of trapped ions, cooled to the motional ground state. Such an initialised state is also required for other demonstrated QIP schemes, such as quantum gates [40, 45], algorithms [20, 21], deterministic teleportation [23, 24], ion-photon entanglement [38], and multiparticle entanglement [28, 29].

Decoherence of superposition and entangled states limits the fidelity of processing operations, and in principle there are many mechanisms of varying magnitudes that may contribute to this [15]. In practice, excessive heating of the trapped ions' motion [97, 110] can be a significant limitation to the fidelity of quantum logic operations. Cooling the trapped ions' motion to the zero point of its energy, and realising low motional heating rates are therefore important capabilities for research in quantum information using trapped ions.

The Doppler limit (eq. 2.13) means that Doppler cooling is not sufficient to achieve ground-state cooling for the trap frequencies used in this experiment. Sideband cooling requires the sidebands to be resolved from the carrier, for which it is required that $\Gamma \ll \omega$. This renders cooling on electric-dipole transitions impractical. Instead, resolved-sideband cooling to the motional ground state has been achieved using weakly-allowed optical transitions, such as quadrupole transitions in $^{198}\mathrm{Hg}^+$ [116] and $^{40}\mathrm{Ca}^+$ [117]; the narrow intercombination line in $^{115}\mathrm{In}^+$ [141]; and two-photon Raman transitions in $^{9}\mathrm{Be}^+$ [142] and $^{111}\mathrm{Cd}^+$ [72]. Laser cooling to the motional ground state has also been achieved in $^{40}\mathrm{Ca}^+$ using a technique based on electromagnetic-induced transparency [143]. Sideband cooling can be extended to more than one ion, and a collective vibrational mode of an ion string has been prepared in the ground state using resolved-sideband cooling [135, 144].

This chapter reports resolved-sideband cooling of a single $^{88}\mathrm{Sr}^+$ ion to the motional ground state, by means of the 674 nm $^2S_{1/2}$—$^2D_{5/2}$ quadrupole transition (natural linewidth 0.41 Hz [31]). This technique is analogous to those described in [116, 117]. The heating rate of an ion initially prepared in the motional ground state has also been measured and is found to be comparable with other reported heating rates [50, 66, 71, 72, 97, 110, 116, 117].

This chapter is arranged as follows. The method used to achieve sideband cooling to the ground state is given in section 5.2. Section 5.3 presents a measurement of the final ground-state occupation probability achieved, and also of the subsequent trap heating rate.

5.2 Method

The relevant energy levels of $^{88}\mathrm{Sr}^+$ for the cooling scheme implemented are shown in figure 5.1. For clarity of notation, certain specific states are written as follows:

$|^2\mathrm{S}_{1/2},\, m_j = -1/2\rangle \rightarrow |\mathrm{S}\rangle,$
$|^2\mathrm{P}_{3/2}\;\, m_j = -3/2\rangle \rightarrow |\mathrm{P}\rangle,$
$|^2\mathrm{D}_{5/2},\, m_j = -5/2\rangle \rightarrow |\mathrm{D}\rangle,$
$|^2\mathrm{D}_{5/2},\, m_j = -1/2\rangle \rightarrow |\mathrm{D}'\rangle.$

The transition wavelengths and decay rates between the various relevant electronic states in $^{88}\mathrm{Sr}^+$ have been summarised in table 2.1.

A single $^{88}\mathrm{Sr}^+$ ion is confined in an endcap trap, as described in chapter 3. This trap provides motional frequencies of $(\omega_\mathrm{X}, \omega_\mathrm{Y}, \omega_\mathrm{Z})/2\pi = (1.94,\ 1.97,\ 3.96)$ MHz. For the experiments reported in this chapter the trap used was exclusively loaded by photoionisation (and hence was exposed to minimal atomic flux) as described in chapter 4. Previous traps which had been loaded using electron-bombardment ionisation were found to have prohibitively high heating rates for ground-state cooling. The laser systems have been described in chapter 3, though the relevant details are summarised here. The ion is initially Doppler cooled by 422 nm light produced by a frequency-doubled diode laser. A neodymium-doped fibre laser generates light at 1092 nm to ensure that the ion is not lost from the cooling cycle. A 674 nm ECDL is stabilised to an ultra-low-drift resonator to realise a linewidth of $\Gamma/2\pi$

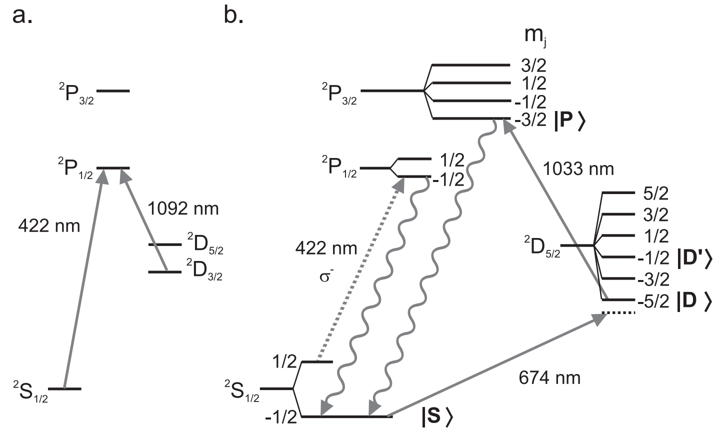

Figure 5.1: Energy levels of ^{88}Sr$^+$. (a) Doppler-cooling scheme. The ion is Doppler cooled using the ^{2}S$_{1/2}$—^{2}P$_{1/2}$ transition at 422 nm. Repumper light at 1092 nm prevents optical pumping into the metastable ^{2}D$_{3/2}$ state. (b) Resolved-sideband-cooling scheme. Zeeman sublevels (labelled by their m_j quantum number) are split using a magnetic field of 380 μT. σ^- polarised light at 422 nm optically pumps the ion into the ^{2}S$_{1/2}$ ($m_j = -1/2$) sublevel. The ion is then sideband cooled using 674 nm light tuned to the lower motional sideband of the ^{2}S$_{1/2}$ ($m_j = -1/2$)—^{2}D$_{5/2}$ ($m_j = -5/2$) transition. A 1033 nm quencher laser returns the ion rapidly to the ground state, to ensure a fast cooling rate.

= 2 kHz. This master laser sideband injection locks a pair of slave lasers to create two narrow-linewidth sources that can be tuned independently across the S—D transition, for sideband cooling on the |S⟩—|D⟩ transition, and spectroscopy on the |S⟩—|D′⟩ transition. The beams are oriented to provide a Lamb-Dicke parameter of $\eta_Z = 0.018$. The 1033 nm quencher and clearout radiations are also produced by an ECDL, which is stabilised to an invar cavity, reducing the drift to $\lesssim$ 60 MHz/h.

The implementation of ground-state cooling for ^{88}Sr$^+$ proceeds in two stages. First the ion is Doppler cooled on the ^{2}S$_{1/2}$—^{2}P$_{1/2}$ dipole transition

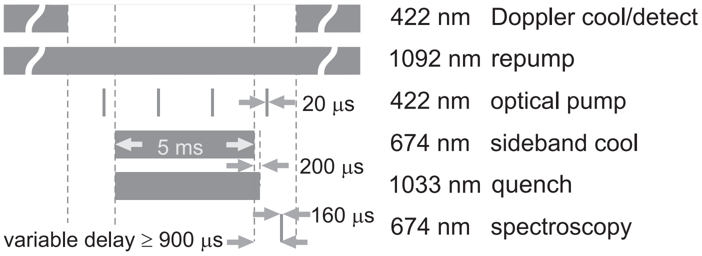

Figure 5.2: Timing of lasers for a single cooling and detection cycle. See the text for details.

using 422 nm light as shown in figure 5.1a. Repumper light of wavelength 1092 nm ensures that if the ion decays into the $^2\mathrm{D}_{3/2}$ state it is rapidly returned to the cooling cycle. The Doppler limit for the axial motion is $\bar{n}_{\mathrm{min}} \simeq 2$, and a mean phonon number of $\bar{n}_{\mathrm{Z}} \simeq 8$ is routinely achieved (see figure 5.4a). Confinement of the ion to the Lamb-Dicke regime is therefore easily obtained (*c.f.* eq. 2.14).

In the second stage the ion is cooled to the ground state using sideband cooling. The laser pulse sequence for this is discussed below, and summarised in figure 5.2. A magnetic field of 380 μT splits the Zeeman sublevels of the ion's electronic states (as shown in figure 5.1b). The ion is prepared in the $|\mathrm{S}\rangle$ state by optical pumping using σ^- polarised light at 422 nm. One potential limitation during sideband cooling is that the ion may decay from the $|\mathrm{P}\rangle$ state to the $^2D_{3/2}$ state, and then via the repumper laser to $|^2\mathrm{S}_{1/2}, m_j = +1/2\rangle$, thereby becoming lost from the cooling cycle. Short optical-pumping pulses can be applied to return the ion to the cooling cycle to avoid this problem. To cool the ion, it is then driven on the lower axial (Z) sideband of the $|\mathrm{S}\rangle$—$|\mathrm{D}\rangle$, $\Delta m = -2$, transition using a 674 nm laser as illustrated in figure 5.1b. The $\Delta m = -2$ transition is red detuned of all other transitions in the Zeeman spectrum, and is therefore chosen to minimise off-resonant excitation on any other transitions, which can lead to heating of the ion.

For sideband cooling to be feasible, the atomic transition must meet the condition $\Gamma \ll \omega$, where $\Gamma/2\pi = 0.41$ Hz is the natural linewidth of the transition [31]. However, such a low spontaneous decay rate does not enable efficient sideband cooling. The $|\mathrm{D}\rangle$ state lifetime is therefore quenched using a 1033 nm laser resonant with the $|\mathrm{D}\rangle$—$|\mathrm{P}\rangle$ transition, in order to achieve an appreciable cooling rate. By adjusting the saturation parameter of this quencher laser, the effective decay rate of the $|\mathrm{D}\rangle$ state, Γ'_{D}, can be tuned for optimal sideband cooling [57]. If the quencher coupling is not strong enough, the decay to the ground state is limited by the long $|\mathrm{D}\rangle$ state lifetime. However, as the quencher saturation parameter is increased, there is increased spontaneous emission from the $|\mathrm{P}\rangle$—$|\mathrm{S}\rangle$ and $|\mathrm{P}\rangle$—$|\mathrm{D}\rangle$ dipole transitions. Increased momentum diffusion arises, which in turn leads to increased heating, and again the net sideband-cooling rate is reduced. Following the reasoning of [17, 57] the optimal saturation parameter for the $|\mathrm{D}\rangle$—$|\mathrm{P}\rangle$ transition is:

$$s_{\mathrm{max}}(n) = \eta\Omega_0\sqrt{8n}/\Gamma_{\mathrm{PS}} \tag{5.1}$$

where Ω_0 is the interaction strength on the $|\mathrm{S}\rangle$—$|\mathrm{D}\rangle$ transition and Γ_{PS} is the $|\mathrm{P}\rangle$—$|\mathrm{S}\rangle$ decay rate. This yields an optimised cooling rate of:

$$\dot{\bar{n}}= \eta\Omega_0\sqrt{2\bar{n}}/4. \tag{5.2}$$

For this experiment, that is $\dot{\bar{n}}_\mathrm{Z} \simeq 12,000\sqrt{\bar{n}_\mathrm{Z}}\,\mathrm{s}^{-1}$. This $\bar{n}$ dependence requires that in order to maintain an optimised cooling rate the quencher laser's saturation parameter must be tuned as $\bar{n}$ reduces during cooling. This would of course alter the AC Stark shift of the $|\mathrm{D}\rangle$ state, and necessitate compensating via tuning the 674 nm sideband-cooling laser accordingly. Due to this additional complexity, a single saturation parameter is chosen and set, which provides an acceptable cooling rate for the $\bar{n}_\mathrm{Z}$ range of the experiment described here.

After cooling, the motional state of the ion is measured from the sideband spectrum of the $|\mathrm{S}\rangle$—$|\mathrm{D}\rangle$, $\Delta m = 0$ transition. This transition has the greatest relative coupling strength, compared to other transitions in the S—D spectrum [145], given the laser beam geometry of our apparatus. The upper and lower sidebands are recorded using pulsed-probe spectroscopy [146], where the Doppler-cooling laser is used to detect the ion's state with near unit efficiency via Dehmelt's electron shelving technique. The mean phonon number of the ion is calculated from the relative coupling strengths of the sidebands (eq. 2.16). If the ion is found to be in the $|\mathrm{S}\rangle$ state, another cooling and detection cycle can be carried out immediately. If the ion is in the $|\mathrm{D}\rangle$ state, a clearout pulse of 1033 nm radiation is applied to avoid having to wait ~0.5 s for the ion to decay naturally on the quadrupole transition.

As discussed earlier, the sideband-cooling rate is optimised via the saturation parameter of the quencher laser beam. In the experiment, the quencher intensity is fixed ($\mathrm{I} = 5\ \mathrm{W\,cm}^{-1}$) and the detuning varied (in region of -300 MHz), in order to tune the saturation parameter. This parameter is set by minimising absorption of the sideband-cooling laser on the cooling

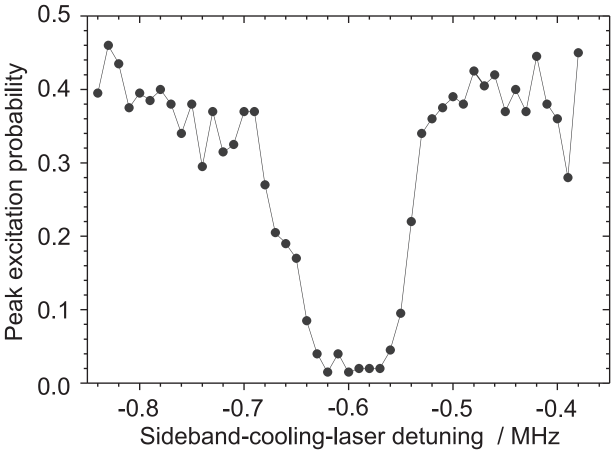

Figure 5.3: Modified sideband-cooling measurement. For a fixed intensity and detuning of the 1033 nm quencher laser, the frequency of the sideband-cooling laser is optimised to account for the quencher-induced AC Stark shift. With the spectroscopy laser always set to the peak of the lower detection sideband, the cooling laser is scanned across the Stark-shifted cooling transition. When sideband cooling is optimised, the excitation probability of the detection sideband is minimised.

transition, in the presence of the quencher. However, the quencher light AC Stark shifts the $|\mathrm{D}\rangle$ state and hence the cooling transition frequency. Therefore by adjusting the saturation parameter to minimise the absorption, the cooling transition frequency shifts as a consequence. Once the quencher parameters are fixed, the AC Stark shift of the cooling transition frequency can be verified using a modified sideband-cooling measurement as follows. The sideband-cooling beam's frequency is scanned across the cooling transition while the spectroscopy beam is fixed on resonance with the lower detection sideband; the excitation probability of this sideband is minimised when the cooling beam is resonant with the cooling transition. This is illustrated in figure 5.3.

5.3 Results

5.3.1 Zero-point cooling

The relative amplitudes of the lower and upper axial sidebands of the $|\mathrm{S}\rangle$—$|\mathrm{D}\rangle$, $\Delta m = 0$ transition are used to determine $\bar{n}_{\mathrm{Z}}$ before, during and after sideband cooling, as described in section 2.4.2. Figure 5.4 shows such axial sidebands following Doppler cooling and also sideband-cooling periods. The fitted curves in this figure were obtained by summing over the Rabi line-shapes [147] for each possible n, weighted by the occupation probability, $P(n|\bar{n})$ (eq. 2.17). The free parameters used for fitting were $\bar{n}$ and Ω_0. The fit value of $\Omega_0 = 2\pi\times 110$ kHz is consistent with the experimentally measured value. Doppler cooling reduces the ion's energy well into the Lamb-Dicke limit with $\bar{n}_{\mathrm{Z}} \simeq 8$ (figure 5.4a). It is found that the ion's vibrational energy is minimised after 5 ms of sideband cooling, where the mean phonon number is measured to be $\bar{n}_{\mathrm{Z}} = 0.03(1)$, corresponding to a ground-state occupation probability of 97(1)% (figure 5.4c). While a few optical-pumping pulses are applied during the cooling cycle, these are not observed to affect the final measured $\bar{n}_{\mathrm{Z}}$.

5.3.2 Heating-rate measurement

The ion's heating rate was determined by varying the delay between the end of the sideband-cooling procedure and the measurement of $\bar{n}_{\mathrm{Z}}$ (*i.e.* the spectroscopy pulse, see figure 5.2). The results of these measurements, presented in figure 5.5, show a linear increase in $\bar{n}_{\mathrm{Z}}$, corresponding to a heating rate

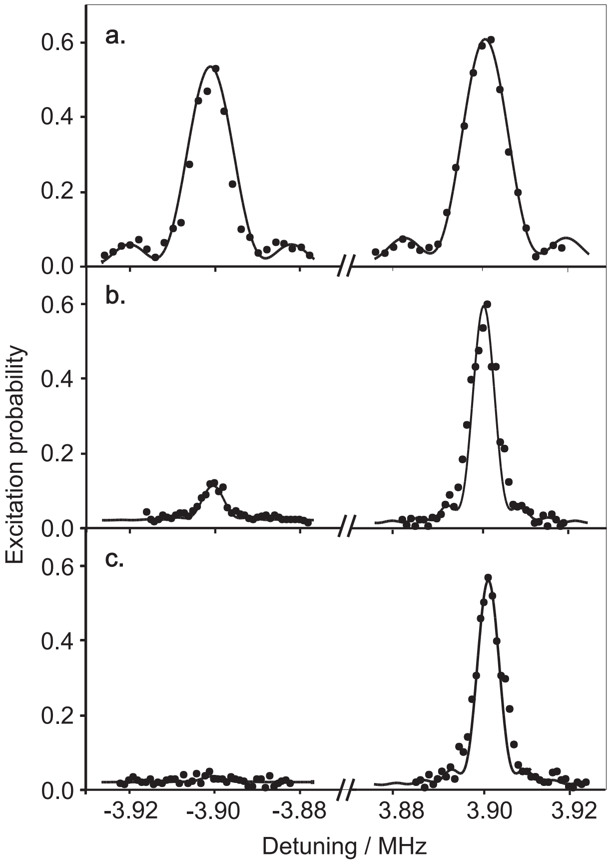

Figure 5.4: Axial sidebands of the $|\mathrm{S}\rangle$—$|\mathrm{D}'\rangle$, $\Delta m = 0$ detection transition after (a) Doppler cooling, $\bar{n}_\mathrm{Z} \simeq 8$, (b) 2 ms sideband cooling, $\bar{n}_\mathrm{Z} = 0.19(2)$, and (c) 5 ms sideband cooling, $\bar{n}_\mathrm{Z} = 0.03(1)$. The phonon number is calculated from the relative sideband interaction strengths (eq. 2.16). The spectroscopy pulse duration was 70 μs in (a) and 160 μs in (b) and (c). The number of interrogations per point ranged from 400 in (a) to 1200 in (c). The solid lines are fits to the data. The small background offset visible in the data of (b) and (c) is due to noise on the spectrum of the 674 nm laser, which causes resonant excitation of other Zeeman transitions in the ion's ${}^2\mathrm{S}_{1/2}(m_j = -1/2)$—${}^2\mathrm{D}_{5/2}$ spectrum.

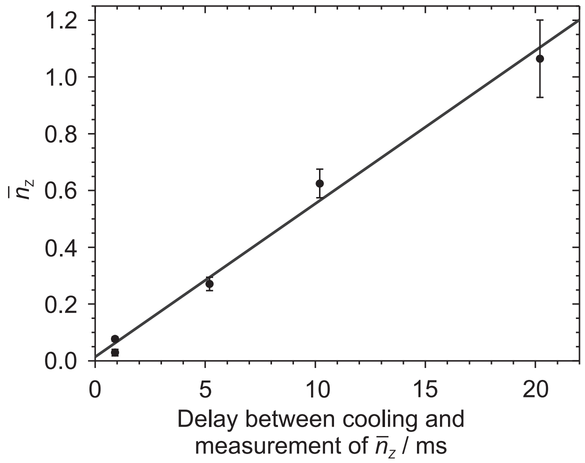

Figure 5.5: Trap heating rate. By increasing the delay between the end of sideband cooling and the spectroscopy pulse, the trap heating rate was determined to be $\dot{\bar{n}} = 0.054(4)$ quanta/ms. By extrapolating the data points to zero delay, the phonon number immediately after cooling is estimated to be $\bar{n}_{\mathrm{Z}} = 0.014(8)$.

of $\dot{\bar{n}}_{\mathrm{Z}} = 0.054(4)$ quanta/ms. The minimum delay between the end of the cooling cycle and the measurement of $\bar{n}_{\mathrm{Z}}$ was 0.9 ms, due to the switching speed of the quencher-beam mechanical shutter. By extrapolating the data in figure 5.5 back to zero delay, the phonon number immediately after cooling is estimated to be $\bar{n}_{\mathrm{Z}} = 0.014(8)$, corresponding to a ground-state occupation probability of 98.6(8)% (*c.f.* eq. 2.17).

As described in section 4.2, the main cause of ion heating is believed to be stochastic fluctuations in the electric field at the ion due to electric-field noise from the trap electrodes. A given magnitude of electric-field noise will give rise to different ion-heating rates dependent upon the ion's mass, M, and the motional frequency, ω. To facilitate a meaningful comparison of traps in different experiments, the measured heating rate is used to calculate the

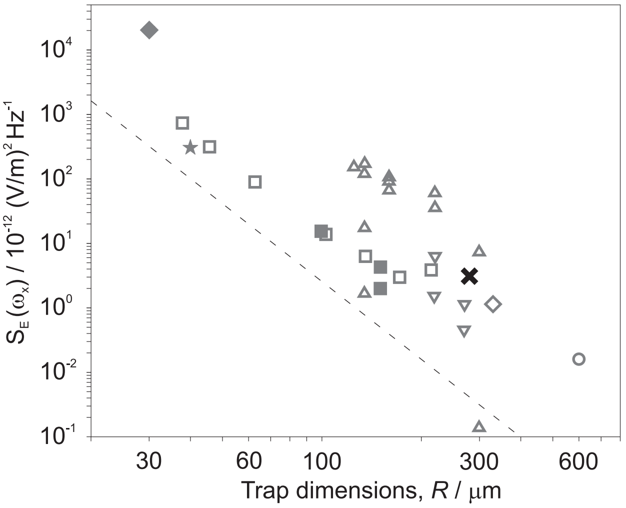

Figure 5.6: Comparison of the spectral density inferred by this work, with that of other traps reported in the literature. The spectral density of electric-field noise of traps in the literature is shown as a function of the ion-electrode separation. The spectral density inferred in this work is marked '×' [94]. For comparison, the figure also shows results from work in ^{9}Be^{+}: ▽ [50], △ [110]; ^{40}Ca^{+}: ○ [117]; ^{111}Cd^{+}: □ [66], ♦ [71], ■ [72]; ^{137}Ba^{+}: ★ [97]; and ^{198}Hg^{+}: ◇ [116]. The dotted line indicates the expected gradient due to an R^4 scaling law [110].

spectral density of the electric-field noise, $S_{\mathrm{E}}(\omega)$, where [110]:

$$S_{\mathrm{E}}(\omega_{\mathrm{Z}}) = 4M\hbar\omega_{\mathrm{Z}}\ \dot{\bar{n}}_{\mathrm{Z}}\ /e^2. \tag{5.3}$$

This quantifies the source of the heating, independent of M and ω. For the experiment described here, $S_{\mathrm{E}} = 3.1(2)\ \times 10^{-12}$ (V/m)^2 Hz^{-1}. This is plotted in figure 5.6 along with other results published in the literature, and can be seen to be comparable with values observed in other traps, once the size of the trap is taken into account.

5.4 Summary

The ability to cool an ion to the motional ground state is a requirement of many trapped-ion QIP applications. The demonstration of traps with low ion-heating rates is also an important capability for such work. We have cooled a single $^{88}\mathrm{Sr}^+$ ion to the zero point of its axial motion, using resolved-sideband cooling on an optical quadrupole transition. The heating rate of the trapped ion has also been measured. Assuming that the source of this heating is fluctuating electric-field noise, this yields an inferred spectral density of the electric-field noise comparable to the values reported by other groups using different traps and atomic species.

CHAPTER 6

Trap modelling

6.1 Introduction

The prospect of an operational quantum information processor is the most significant driver for ion-trap research at present. Experimental demonstrations such as quantum gates [40, 45], algorithms [20, 21], deterministic teleportation [23, 24], and ion-photon entanglement [38] have positioned trapped ions as a viable technology for quantum information processing (QIP). While current experiments have been performed using only a few qubits at most [28, 29], the scaling-up of devices to handle large numbers of qubits remains a significant challenge. Cirac and Zoller's original proposal for QIP with trapped ions [44] requires a linear string of ions in a single trapping potential, where the ions' internal electronic energy levels represent the qubit logic states, and the mutual Coulomb interaction facilitates the transfer of quantum information between the ions. Technical and fundamental limits are placed on the computations that can be carried out by a linear string of ions in a single trap [148]. As more ions are introduced to the string, the sideband spectrum becomes more complicated. It can be ensured that the sidebands are well spaced in frequency by increasing the axial trap frequency, though this in turn decreases the physical inter-ion spacing. This increases cross talk between the addressing laser for a particular ion and the neighbouring ions. Considering Shor's algorithm, it is suggested that using typical quadrupole transitions as a qubit, trapped ion quantum computers with a single segment could only factorise a ∼10-bit number [148]. It is, however, proposed that trapped-ion quantum computing systems can nonetheless be scaled to handle many qubits by using an architecture based on an array of many interconnected ion traps [34]. By segmenting the single, long electrode of a standard linear Paul trap (described in section 2.3), and applying appropriate voltages to the segments, the axial potential can be made so that many ions can be held in separate, independent trapping potentials. An example of the concept envisaged is illustrated in figure 6.1. Such a device would comprise distinct zones for loading, processing and storing qubits, and ions would be shuttled between the zones by applying appropriate time-varying voltages to the electrode segments. This would enable a trapped-ion quantum computer to realise DiVincenzo Criterion #1 ("A scalable system" [30], see chapter 1 for discussion). It would also facilitate one method of realising DiVincenzo Criterion #5 ("Qubit specific measurement" [30], see chapter 1 for discussion). Additionally, quantum gates have been proposed for segmented traps in which ions are moved into and out of stationary laser beams [149]. This has the benefit over other systems of simplifying the optics required for the laser systems.

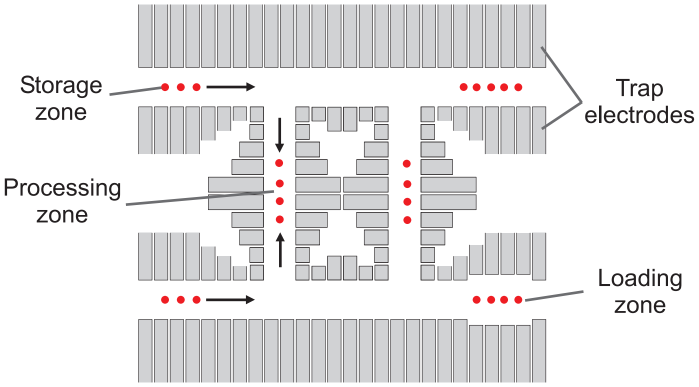

Figure 6.1: Generic concept for a segmented-trap architecture [34]. Each set of segments traps like a standard linear Paul trap, and ions can be shuttled between different zones.

There are several types of segmented linear traps that have been either used or proposed by various research groups, as illustrated in figure 2.3. The designs demonstrated in the literature have had electrodes arranged in either two layers [50, 71]; or three layers [72–75]; or had all the electrodes in a plane [77]. This thesis work proposes a design for a novel ion-trap quantum processor chip, microfabricated using a process based on planar silica-on-silicon techniques [95]. The trap electrodes are made of gold-coated silica (SiO_2) and are spaced by highly-doped silicon in a monolithic structure. This design is expected to allow a trap of unit aspect ratio, with an ion-electrode separation down to 100 μm, and which is scalable to many (*i.e.* $10^2 \rightarrow 10^3$) trapping segments. Any trap design is necessarily constrained by the physics of the trapping potential, practical limitations such as material properties, and fabrication considerations. This chapter describes the modelling of the trapping potential and the operating parameters required to achieve experimentally useful motional frequencies (a few MHz). Several possible practical problems are also modelled and are not expected to be a factor limiting the trap's operation. The monolithic, unit-aspect-ratio trap proposed is expected to exhibit a deep potential well with high trap efficiency, and a low RF loss, when compared to other microfabricated traps. This fabrication technology is in principle scalable to complex devices, and may form the basis for large-scale ion-trap quantum processors.

This chapter is arranged as follows. Section 6.2 outlines the geometry of the proposed structure. Section 6.3 describes the finite-element methods used to model the trapping behaviour of this structure. The results obtained using such methods are given in section 6.4. The modelling of several possible failure modes is presented in section 6.5, and it is shown that these are not expected to limit trap operation. The fabrication of the structures modelled is considered in chapter 7.

6.2 Geometry

The physics of ion trapping in a linear Paul trap is explained in section 2.3. Importantly, a linear Paul trap [60] can be deformed significantly from its idealised hyperbolic geometry, yet still maintain a harmonic potential, provided the ion is close to the trap axis (*i.e.* provided the ions' vibrational quantum number, n, is small). Examples of such deformations to the trap geometry include making traps with very high aspect ratios [70, 71]; changing the number of electrodes [72–75]; and placing all the electrodes in a plane [76, 77]. Nonetheless, while different realisations of linear RF traps may appear dissimilar, the basic physics of the trapping potential remains unchanged, save

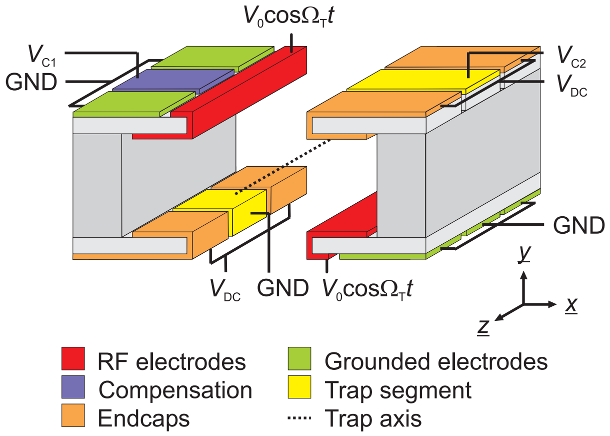

Figure 6.2: Microtrap electrode connections for an elementary unit cell. An RF voltage, $V = V_0 \cos \Omega_{\mathrm{T}} t$, on each of two electrodes running the full length of the trap provides the radial (xy) trapping potential, where the trap axis is shown as a dotted line. A DC voltage, V_{DC}, is applied to the four endcap electrodes and provides axial (z) confinement. The voltages V_{C1} and V_{C2} can be applied to compensate for micromotion.

for a dimensionless geometrical factor, η, known as the trap efficiency [70].

The most elementary unit cell of the trap required to provide a confining potential is shown in figure 6.2. The radially confining potential is created by applying an RF voltage, $V(t) = V_0 \cos \Omega_{\mathrm{T}} t$, to a pair of electrodes which run the full length of the trap, while all other electrodes are held at RF ground. The ion is confined axially by a DC voltage, V_{DC}, applied to the four endcap segments. For realistic traps, imperfections in fabrication and stray charges on insulating surfaces can displace the ion from the trap axis, leading to excess micromotion [81]. This is a driven motion at the trap drive frequency, which is explained in more detail in section 2.3.4. By applying DC voltages, V_{C1} to the compensation electrodes (behind the RF electrode)

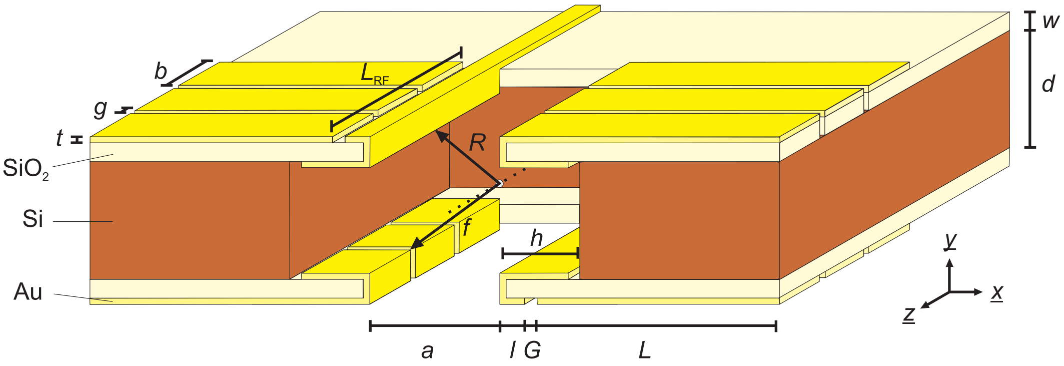

Figure 6.3: Trap design concept and parameter definitions. The electrodes are made of gold-coated SiO_2 layers, which are spaced by highly-doped silicon. The entire construction is created from a single silicon wafer. The section shown can be extended to include many more than three segments, or more complicated geometries such as varying a along the length of the trap, or including junctions. Typical values of the dimensions indicated are listed in table 6.1

and V_{C2} across the trap segment electrodes, the ion can be returned to the trap axis. Micromotion can thereby be minimised independently in each trapping segment. Throughout this chapter, the coordinate reference frame shown in figure 6.2 is generally used, with unit vectors $\underline{\hat{x}}$ (perpendicular to the trap axis, in the plane of the wafer), $\underline{\hat{y}}$ (perpendicular to the plane of the wafer), and $\underline{\hat{z}}$ (parallel to the trap axis). This is chosen as a reasonable coordinate system when discussing wafer dimensions. It should be noted that the principal axes of the trapping potential are not necessarily aligned along these axes. When a different set of coordinate axes is more appropriate this is made clear in each such instance.

A cut-away section of the proposed design is shown in figure 6.3. The electrodes, formed by a 5 μm layer of gold overlaid on 15 μm of SiO_2, are spaced

Parameter	Value			Units
	Trap #1	Trap #2	Trap #3	
Ion-electrode separation, R	350	160	90	μm
Wafer thickness, d	500	250	150	μm
Electrode separation, a	500	250	100	μm
Recess depth, h	300	300	200	μm
RF-DC electrode spacing, G	50	50	25	μm
DC-DC electrode spacing, g		10		μm
Electrode length, b		20 to 1000		μm
Ion-endcap separation, f		90 to 600		μm
Silica thickness, w		15		μm
Gold thickness, t		5		μm
RF electrode width, l		20		μm
Distance to edge of chip, L		$\sim$ 4000		μm

Table 6.1: Typical dimensions for different sizes of traps. All of these dimensions are believed to be reasonable, given existing silica-on-silicon fabrication processes.

by highly-doped silicon. All traps considered have an aspect ratio of one (*i.e.* $a/d = 1$). For the calculations presented in this chapter, silicon wafers of different thickness, d, are considered in the range 150 μm $< d <$ 500 μm. The structure shown in the figure is part of a larger 'chip', the dimensions of which are dictated by packaging and electrical connectivity requirements (as described in section 7.4.5). The un-etched areas of the chip, away from the trapping region, provide mechanical support for the trap electrodes, and are gold patterned with bonding pads for electrical connectivity (not shown in figure 6.3). The radial size of the trap is characterised by R, the distance from the trap axis to the nearest point on the electrodes. The characteristic distance for the axial behaviour, f, is the distance from the ion to the nearest point of a DC endcap electrode. Table 6.1 lists examples of the physical dimensions indicated in figure 6.3, for three traps of differing size. The chosen values (or ranges of values) are set by physical or fabrication constraints. These constraints are explained as they arise in the remainder of this chapter, and in chapter 7.

The three segments shown in figure 6.3 create a single trapping zone. However, by extending the design to include more segments, many independent trapping zones can be achieved. (Two independent trapping zones require at least 5 segments, three zones require 7 segments, and so on.) A trapped-ion quantum computer may be required to carry out a number of different operations [30, 34, 150], such as loading, storing, shuttling and optically addressing ions, and bringing together and separating small numbers of ions. It is useful to have dedicated regions for different tasks. For example, a region where quantum algorithms are carried out will need a low heating rate, and therefore require that the electrodes are as uncontaminated as possible (see discussion in section 4.2). Electrodes in the region where ions are loaded will receive a certain degree of contamination from the atomic source. By having separate regions for each purpose, certain limitations (*e.g.* high heating rates) can be confined to regions where they are unimportant (in this case, far from the interaction region). In the proposed segmented design the geometry of different trapping zones can be optimised for each specific purpose.

6.3 Finite-element methods

6.3.1 Introduction

For a limited number of geometries, potential distributions can be calculated analytically. In general, however, this is not the case and some numerical method is required. The electrostatic potentials due to the trap geometry described above were modelled by finite-element methods (FEM) using FEMLAB[1]. This data was then processed using MATLAB[2] to calculate the trapping behaviour of the system. For some results the values obtained by these methods were independently verified using SIMION 3D[3]. This ion-optics package calculated the potentials by a finite difference method (FDM) and modelled the effect of the full, time-varying RF potential on a charged, massive ion. The entire modelling procedure is summarised by the flow diagram shown in figure 6.4.

Figures 6.2 and 6.3 illustrate the proposed physical trap geometry. The notation used for the finite-element modelling is similar to that shown, with some minor modifications. The nomenclature for DC voltages given in figure 6.2 is useful for indicating specific voltages, applied to specific electrodes, for a particular purpose. In modelling the geometry, however, it is often more convenient to denote a general DC voltage applied to a general DC electrode as U_0. The potential distribution produced by a DC voltage, U_0, applied to a particular electrode geometry is then denoted U, and that produced by an

---

[1] FEMLAB 3.2, COMSOL, Inc., MA. 2004. Now called COMSOL Multiphysics.

[2] MATLAB 7.1, The MathWorks, Inc., MA. 2005.

[3] SIMION 3D 7.0, Scientific Instrument Services, Inc. NJ. 2003.

RF voltage, V_0, denoted V. In the physical system, the trap electrodes have some length, $L \gg a$ (see figure 6.3 and table 6.1). The trap will then be enclosed in a vacuum chamber, comprising conductors and dielectrics at some large distance from the ion (as described in section 7.4.5). In the computer model, the boundary condition is taken to be an insulator. *i.e.* at the boundary the electric field has only a tangential component to the boundary. The boundary was then moved back in each direction until the calculated values for the motional frequencies remained constant. This was found to require radial distances $> 3R$ and an axial distance $> 3f$. This is consistent with the design rules for microtrap fabrication used by other groups [150]. It can be noted that given the boundary was sufficiently distant to not affect the trapping potential, essentially identical trapping potentials are achieved by modelling conducting (instead of insulating) boundary conditions.

For the majority of the work described here, only the unit cell of three segments is considered. The algorithms required can be easily modified to consider more segments. However, for many segments ($\gtrsim$6) the processing speed becomes prohibitively slow and other, more efficient methods become favourable. Using FEM, the entire volume under consideration is discretised, and Maxwell's equations are solved for the potential distribution on the electrodes. Other work modelling similar systems has been carried out using boundary-element methods (BEM) [151–153]. By this method, only the electrode surfaces are discretised, and Maxwell's equations are solved for the charges on these surfaces. FEMLAB was chosen for the work described here as (for smaller systems) the benefits gained from the ease of using the software and its interface with other programmes were believed to outweigh any reduction in speed.

6.3.2 Two-dimensional modelling

Much of the trap behaviour can be well modelled by considering a cross-section through the centre of the trap in the $z = 0$ plane, and assuming that the electrodes extend uniformly and infinitely far in the axial direction. This is a good approximation provided that the gap between the electrodes, g, is small compared to the gap's distance from the ion, f, (*i.e.* $g \ll f$) and that any discontinuities in voltage occur at distances much greater than the ion-electrode separation. For the proposed trap the 2D model therefore provides a good description of the RF trapping potential. The fact that a voltage applied to the DC endcaps necessarily breaks the uniformity along the z-axis means that the DC potential cannot be described by a 2D model. The 3D modelling is described in section 6.3.3.

The general process for the 2D modelling is summarised in figure 6.4, and illustrated in figure 6.5. First, the electrode geometry is entered into FEMLAB. The boundary conditions can be set as required, and the geometry is meshed (figure 6.5a). The mesh is set to be finer near the tips of the electrodes as these are the regions of greatest potential gradient, and the finer mesh here reduces numerical errors. The mesh is also finer near the trap centre as this is the region over which most of the later fits are done, and a coarse mesh can give rise to significant interpolation errors. FEMLAB then solves for the potential, $V(x, y)$, produced by the geometry and boundary conditions specified (figure 6.5b). As described in section 2.3 (eq. 2.4) the

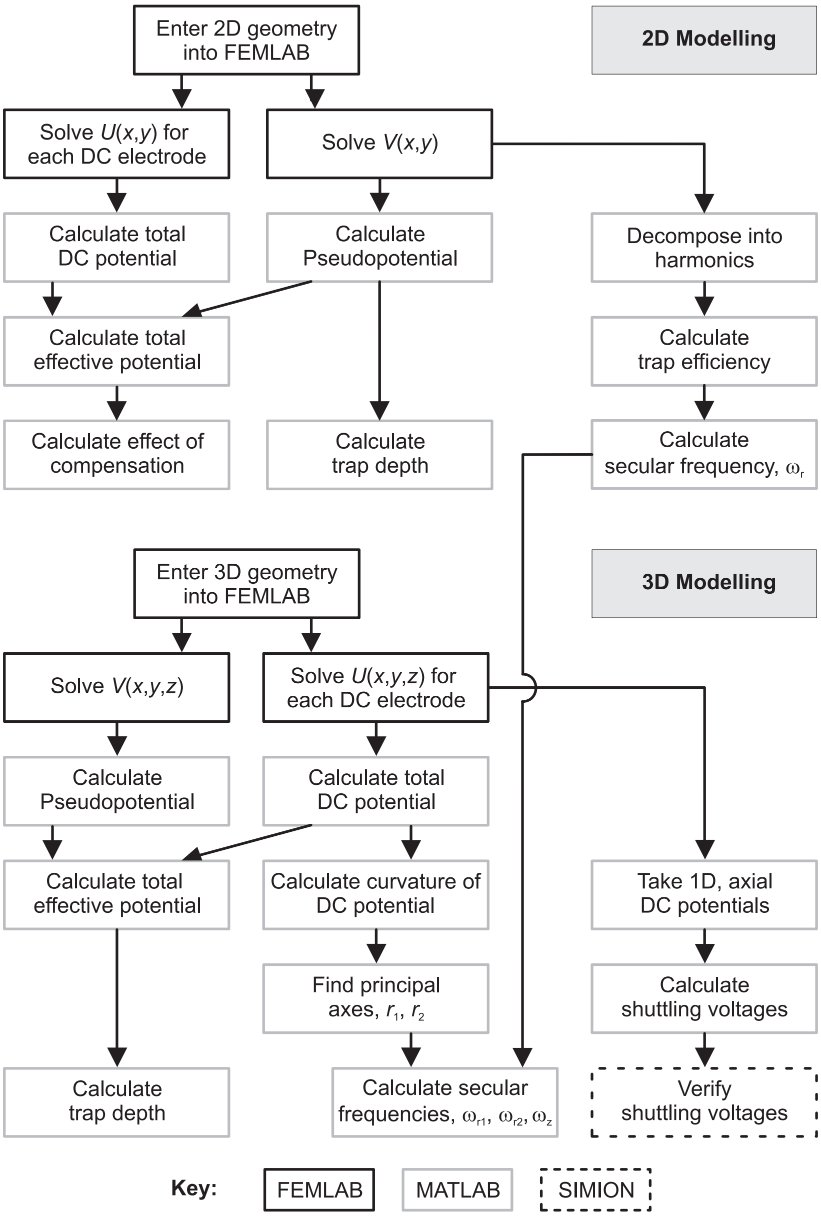

Figure 6.4: FEM process summary. This shows the dependencies for different calculations, and how the parts of the modelling process fit together. See text for details of each stage.

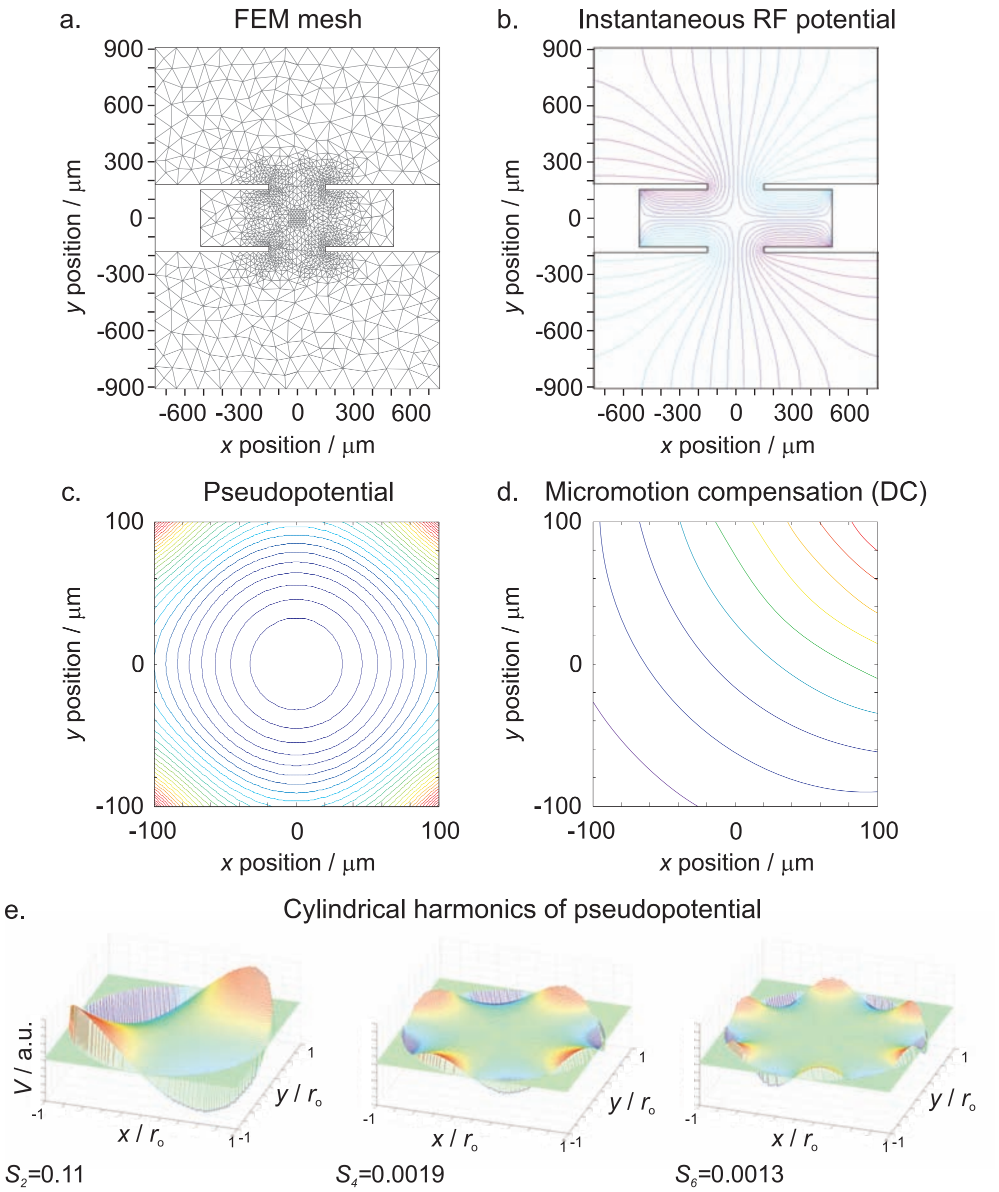

Figure 6.5: 2D modelling process. (a) The geometry is entered into FEMLAB and meshed. (b) The potential, $V(x, y)$, is solved for the specified boundary conditions. The figure shows equipotential lines for 1V being placed on diagonally opposite electrodes. (c) $V(x, y)$ is imported into MATLAB and the pseudopotential is calculated. The figure shows equipotential lines for the pseudopotential. (d) The potential, $U(x, y)$, due to the DC potentials applied to various electrodes is calculated. (e) If required, the instantaneous potential calculated in (b) can be decomposed into weighted circular harmonics, using a fitting algorithm in MATLAB.

pseudopotential, ψ, is given by:

$$\psi = \frac{e^2}{4M\Omega_{\mathrm{T}}^2}|\nabla V(x,y,z)|^2. \tag{6.1}$$

This pseudopotential is calculated for the specified trap geometry in MATLAB, using the potential obtained by FEMLAB (figure 6.5c). This pseudopotential can then be considered directly if required. Alternatively, the instantaneous potential can be decomposed into a set of harmonics for further analysis (figure 6.5e).

The algorithm for finding the weighted harmonics is carried out as follows. In general, an arbitrary 2D potential, $V(r,\theta)$, can be decomposed into a series of circular harmonics:

$$V(r,\theta) = V_0\left[\sum_{n=0}^{\infty} C_n\left(\frac{r}{r_0}\right)^n \cos(n\theta) + \sum_{m=1}^{\infty} S_m\left(\frac{r}{r_0}\right)^m \sin(m\theta)\right] \tag{6.2}$$

where r_0 is the radius over which the fit is made, and C_n and S_m are coefficients of the expansion. The expansion coefficients in eq. 6.2 are found using the following fitting algorithm. Let the potential calculated by FEMLAB be called V^{FEM}, and the potential generated by the summation in eq. 6.2 with some arbitrary set of C_n, S_m be V^{fit}. The fitting problem then becomes one of minimising the parameter:

$$F(C) = \sum_{i,j=1}^{I,J}\left(V_{ij}^{\mathrm{fit}}(C) - V_{ij}^{\mathrm{FEM}}\right)^2\ , \tag{6.3}$$

where

$$\begin{aligned} V_{ij}^{\mathrm{fit}}(C) &= \sum_{k=1}^{K} C_k P_{ijk} \ , & (6.4) \\ C &= (C_0, C_1, C_2, ..., C_N, S_1, ..., S_M) \ , & (6.5) \end{aligned}$$

and each layer, P_k, is the basis harmonic potential corresponding to C_k. I and J correspond to the size of the x, y array of data exported from FEMLAB. $K = N + M$ is the number of harmonics included in the summation. It may be noted that eq. 6.4 is entirely equivalent to eq. 6.2, if eq. 6.2 is terminated at $n = N$, $m = M$ instead of being an infinite series, and if $V_0 = 1$ V. Differentiating $F(C)$ with respect to each of the C_k and setting the differential to zero will give a minimum in this parameter, *i.e.* the best fit.

$$\begin{aligned} \frac{\partial F}{\partial C_k} &= \sum_{i,j=1}^{I,J} 2\left(V_{ij}^{\mathrm{fit}}(C) - V_{ij}^{\mathrm{FEM}}\right) \frac{\partial V_{ij}^{\mathrm{fit}}(C)}{\partial C_k} \\ &= 2\left(\sum_{k=1}^{K} C_k A_{ijk} - b_{ij}\right) \qquad = 0 & (6.6) \end{aligned}$$

where

$$\begin{aligned} \mathbf{A} &= \mathbf{P}\ \mathbf{P}^T \ , & (6.7) \\ \mathbf{b} &= \mathbf{P}\ \mathbf{V}^{\mathrm{FEM}}. & (6.8) \end{aligned}$$

It can be seen from eq. 6.6 that solving the minimisation problem is equivalent to solving the problem $C\mathbf{A} = \mathbf{b}$. This can be done efficiently in MATLAB.

Secular frequency

As described in section 2.3, the secular frequency of an ion confined in a linear RF trap of arbitrary geometry is given by:

$$\omega_\mathrm{r} = \frac{e\ V_0\ \eta}{\sqrt{2}\ M\ \Omega_\mathrm{T}\ R^2}\ . \tag{6.9}$$

All terms on the right hand side are known, except for the efficiency, η, which is defined as the ratio of the quadrupole component of a given trap to that of a hyperbolic trap of the same characteristic dimension. An ideal hyperbolic trap has only a quadrupole component. This means that, from eq. 6.2, for an ion-electrode separation R, $S_2^\mathrm{hyp} = 0.5(r_0/R)^2$, and all other expansion coefficients are zero. For a general trap the efficiency can therefore be given as:

$$\eta = \frac{2\ S_2\ R^2}{{r_0}^2}\ . \tag{6.10}$$

By eq. 6.9, the secular frequency of the ion can be then calculated. It is worth noting that because each basis function in eq. 6.2 is orthogonal to each of the others, the best fit value of S_2 found by the optimisation algorithm should be independent of how many higher orders are added to $\mathbf{P}$. In practice adding higher orders changes the optimised value of the fit S_2 by less than one percent.

By way of testing the algorithm, several analytically solvable cases can be modelled. One simple case is that of a hyperbolic trap which by definition has an efficiency of 1. The algorithm described above gives the correct answer to within 0.5 %, where the discrepancy is due to the model boundary being a finite distance away, rather than the electrodes asymptotically approaching each other. A second analytically solvable case is that of a trap in the limit of high aspect ratio (*i.e.* $a/d \rightarrow \infty$) where $\eta \rightarrow 1/\pi$ [70]. The algorithm described here agrees to within 1 % for an aspect ratio of 100.

Trap depth

In determining the maximum energy of an ion which can be trapped, or how energetic a collision with the background gas can be before the ion is lost from the trap, it is useful to know the depth of an ion trap's potential. The trap depth is determined by the saddle point which occurs in the effective potential between the electrode tips, indicated in figure 6.6. To calculate the depth of the proposed trap, the pseudopotential is calculated and the difference between the potential at the saddle point and the potential minimum is taken.

Compensation voltages

In a physical trap imperfections in fabrication or static charges on insulators can perturb the trapping potential so that the ion no longer resides at the RF null. The ion can be moved back in to position by applying DC compensation voltages (V_{C1} and V_{C2}, figure 6.2). The effect of such compensation voltages can be modelled in 2D by calculating the potential, U, due to a voltage applied across the trap segment (figure 6.5d). When this is added to the pseudopotential, the position of the minimum in the total effective potential is translated. This procedure is repeated for voltages applied to one of the compensation electrodes.

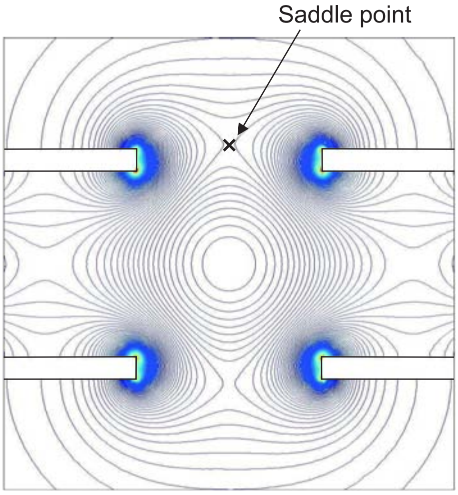

Figure 6.6: Calculating the trap depth. The lowest point of the trap "wall" is set by the position of the saddle point in the pseudopotential between the electrode tips. The trap design model shown here is slightly simplified in that the compensation electrodes (*c.f.* figure 6.2) effectively have an RF voltage applied. The effect of this at the saddle point is negligible.

6.3.3 Three dimensional modelling

To this point, it has been assumed that a linear trap can be modelled in two dimensions. While this is a good approximation for the RF pseudopotential, it does not hold when considering the effect of the DC endcaps; clearly, for example, a potential which is uniform along its length (as in the 2D approximation) does not axially confine ions. Three-dimensional modelling is therefore required to calculate the axial motional frequency, and also corrections to the radial motional frequency, due to the DC endcap potential. It is noted that the trap efficiency is dependent only on the RF potential, and remains unaltered by considering a 3D trap.

The 3D modelling process is summarised in figure 6.4 and illustrated in figure 6.7. It is carried out in a similar fashion to the 2D case. The geometry is entered into FEMLAB and meshed. The potential is then solved for the specified boundary conditions. An example of the calculated potential is shown in figure 6.7a. From the RF potential, the pseudopotential is calculated in MATLAB, a 2D section of which is shown in figure 6.7b. The DC potentials due to each of the DC electrodes (including compensation electrodes) are also calculated and summed (figure 6.7c). For some of the calculations outlined below the potential must be converted into cylindrical coordinates, and rotated about the z-axis of the trap. To facilitate this in MATLAB, all data points which lie outside a radius of interest are removed, as can be seen at the corners for figure 6.7c. The total effective potential that the ion experiences is then the sum of the RF pseudopotential and the DC potential.

Principal axes

In the treatment so far, the ion's radial motion has been degenerate. In this section that degeneracy is lifted, and the radial secular frequency is split into ω_{r_1} and ω_{r_2}. To cool all three motional degrees of freedom, the cooling laser must have a component of its **k**-vector oblique to all three principal axes of the motion (*i.e.* r_1, r_2, and z). When planning the cooling-laser beam angles it is therefore necessary to know what the principal axes of the ion's motion are. Additionally, the direction of these axes must be known to calculate the new motional frequencies, ω_{r_1}, ω_{r_2}.

Near the trap axis, the pseudopotential due to the RF voltage is radially

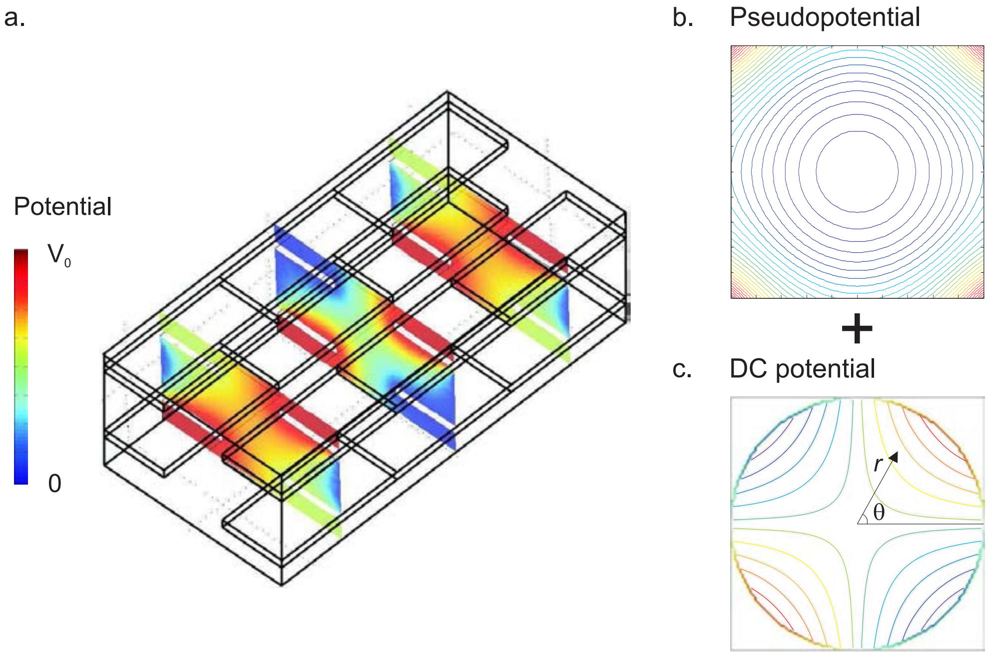

Figure 6.7: Calculation of the 3D potential. (a) The DC potential is calculated in 3D using FEMLAB. The potential is calculated for the entire volume, although for clarity only three cross sections are shown. The processing to achieve this is essentially a 3D generalisation of figure 6.5a–b. (b) The pseudopotential is calculated in a similar fashion to before. Here only a 2D slice is shown. (c) The total potential due to the DC electrodes is calculated. This is converted into cylindrical coordinates to facilitate the calculation if the principal axes, as described in the text. The total effective potential is found as the sum of the RF pseudopotential, and the total DC potential.

symmetric. This can be seen in figure 6.7b. The ion therefore does not have any preferred direction. From eq. 6.9 it can be seen that this is generally true, independent of the geometry of the trap; the inclusion of η does not break the radial symmetry of ω_r near the trap axis. Rather, the symmetry is broken by the addition of the DC endcap potentials (see figure 6.7c); the saddle shape of the DC potential adds to the pseudopotential in one direction, and subtracts from it in another. To find the principal axes, the curvature of the DC potential is calculated at the trap centre. *i.e.*

$$\left.\frac{\partial^2}{\partial r^2} U(r, z, \theta)\right|_{r=z=0} \tag{6.11}$$

is calculated in the range $0 \leqslant \theta \leqslant \pi$. The principal axes occur at the two extrema of this expression. These are found by taking sections through the origin (*i.e.* at the trap centre) at different values of $\theta = \theta'$, and fitting a quadratic curve of the form:

$$U(r, \theta') = c_2 r^2 + c_1 \, r + c_0 \tag{6.12}$$

to each. The second derivative of this quadratic is equal to $2c_2$. By plotting $c_2(\theta)$ the angles of the two extrema of eq. 6.11 (*i.e.* the principal trap axes) can easily be found.

Motional frequencies

As established from eqs. 2.1–2.2 the DC potential due to the endcaps cannot be trapping in all three dimensions. For the traps considered here the potential is trapping in the axial direction, and one radial direction, and anti-trapping in the perpendicular radial direction. The addition of this DC potential to the pseudopotential therefore necessarily gives rise to a splitting of the radial, secular frequency which was calculated above. Considering the quadratic component of the potential near the trap centre, the Taylor expansion of a symmetric but otherwise arbitrary DC potential $U(r_1, r_2, z)$ can be written as:

$$U = \frac{U_0}{2}(D_{\mathrm{r}_1} r_1^2 + D_{\mathrm{r}_2} r_2^2 + D_{\mathrm{z}} z^2) + c \tag{6.13}$$

where $\hat{\underline{r}}_1$ and $\hat{\underline{r}}_2$ are the principal axes in the radial direction, c is a constant, and D_{r_1}, D_{r_2} and D_{z} are expansion coefficients which give a measure of the tightness of the trap at the centre. By comparing eqs. 6.12–6.13, it can be seen that these coefficients can be expressed as:

$$D_i = \frac{2}{U_0} c_{2,i}. \tag{6.14}$$

for $i = r_1$, r_2, z. From these D_i the axial frequency and the corrected radial frequencies can be calculated [70]:

$$\begin{aligned} \omega_{\mathrm{z}} &= \sqrt{\frac{2\ \kappa\ e\ U_0}{M\ f^2}} \quad , \\ \omega_{\mathrm{r}_1} &= \sqrt{{\omega_{\mathrm{r}}}^2 - \qquad \epsilon\ {\omega_{\mathrm{z}}}^2}\ , \\ \omega_{\mathrm{r}_2} &= \sqrt{{\omega_{\mathrm{r}}}^2 - (1-\epsilon){\omega_{\mathrm{z}}}^2}\ , \end{aligned} \tag{6.15}$$

where:

$$\begin{aligned} \epsilon &= -\frac{D_\mathrm{x}}{D_\mathrm{z}} = 1 + \frac{D_\mathrm{y}}{D_\mathrm{z}} \ , \qquad (6.16) \\ \kappa &= \frac{D_\mathrm{z} f^2}{2} \ . \qquad (6.17) \end{aligned}$$

Given the reasoning of eqs. 6.13–6.17, the problem of finding the motional frequencies along each axis is now equivalent to calculating the total effective potential for a given electrode geometry in three dimensions, and evaluating the second derivative of that potential at the origin.

A test for the code's self consistency can be seen from eq. 6.16: there are two methods of calculating ϵ which, in principle, should both give the same result. In practice, uncertainties in the numerical calculations mean the two values (termed ϵ_x and ϵ_y respectively) are slightly different. For the results quoted here, ϵ_x and ϵ_y vary by $\lesssim 2\%$ and the mean value has been taken.

Ion transport

The ability to transport ("shuttle") ions from one trap segment to another is a promising method of scaling trapped-ion quantum computers beyond the level of a few ions [34, 75, 154]. Shuttling of ions has been demonstrated in linear segmented traps [50, 71] and through junctions [73, 75]. It has also been demonstrated to preserve the coherence of electronic states when implemented between steps of quantum protocols [22, 24, 50, 155]. Ions are moved by varying the DC potentials on different segments of the trap, and thereby moving the axial position of the trap minimum.

To investigate the shuttling of single ions, a trap model with five segments was used. It is required that sets of DC electrode voltages are found which provide—for each point along the trap axis—a harmonic axial confining potential. The trap is modelled in 3D using FEMLAB and MATLAB as described above. The potential due to each electrode is calculated by applying 1 V to each electrode in turn, while all other electrodes remain grounded. By superposition of these solutions a potential due to an arbitrary combination of voltages can be found without the time-consuming requirement of re-running the finite-element solver. The potentials along the trap axis ($x = y = 0$) are taken, and thereafter the problem is treated as being one dimensional. This is a reasonable approximation, provided the DC potential at the ion is small compared to the depth of the pseudopotential, and the stability parameters a^L and a^{DC} (eqs. 2.9–2.10) are sufficiently small that the trap remains stable.

Calculation of the voltages needed for shuttling an ion requires that electrode voltages be found for each of the five DC electrode pairs which provide a harmonic potential for different axial positions of the potential minimum. To do this, the reasoning of section 6.3.2 can be modified to solve a 1D problem. The nomenclature may now seem a little strange, but it is used to follow the formalism of eqs. 6.3–6.8. The 1D potentials due to each of the five pairs of DC electrodes were taken as five basis sets, each point of which is denoted P_{ik}. A MATLAB routine then optimises the five DC electrode voltages (C_k) so that over an arbitrary range the resultant axial potential (V^{fit}) will fit a 1D harmonic potential (V^{FEM}). By doing this over a range of positions for the harmonic potential minimum, a set of smoothly varying electrode voltages can be obtained which shuttles ions between trap segments.

It is not necessary for the axial potential to be harmonic along the full length of the trap. If the algorithm is required to fit a potential over too great a range then it will improve the fit away from the trap centre (which is of no interest) at the cost of the quality of fit close to the ion. Additionally, the electrode voltages calculated to provide a harmonic potential along an extended region can be large (hundreds or thousands of volts) which is impractical and unnecessary. The axial distance over which the fit was required was set to ensure that the range was useful, and the voltages required were practical.

If the DC voltages used for shuttling are too large they can cause the trap to be unstable (*c.f.* eq. 2.10. Note, the large voltages mentioned above in connection with the range of the fit should be avoided on grounds of practicality: the electrodes in question are far from the ion and have little effect on the potential the ion experiences. The stability problem considered here is a separate issue). To ensure that the shuttling voltages moved the ion as expected, and the trap remained stable throughout the shuttling operation, the calculated voltages were applied to a 3D model of the trap using SIMION 3D. Rather than simply calculating the pseudopotential approximation, this programme models the effect of the full, time-varying RF potential on a charged, massive ion.

6.4 Finite-element results

Motional frequencies and trap depths are calculated for a range of trap sizes, voltages and drive frequencies. This is done to show that, in principle, the geometry described here can provide a stable trapping potential for achievable experimental parameters. The effect of compensation voltages on the position of the potential minimum is calculated, and shown to allow compensation of expected perturbations using reasonable voltages. Finally, smoothly varying DC voltages are calculated which will shuttle an ion between trap segments while maintaining a harmonic axial potential.

6.4.1 Motional frequencies

For traps of the design proposed here, the efficiency increases with decreasing size, from $\eta = 70\%$ for a trap with $R = 350$ μm, to $\eta = 79\%$ for $R = 90$ μm. This change is due to the SiO_2 thickness, w, not being scaled with the trap size, R; as the trap size becomes smaller the proportionally thicker SiO_2 better approximates a hyperbola. Ideally the grounded, conducting surfaces of the silicon are sufficiently far from the ion that they do not perturb the potential. For mechanical reasons (discussed in section 6.5) and due to fabrication constraints (chapter 7) the undercut distance, h (figure 6.3), cannot be arbitrarily deep. The trap efficiency as a function of the recess depth for different trap sizes is shown in figure 6.8. Several points are of interest. Firstly, it is noted that there is little additional benefit to undercuts of $h \gg R$. Also, in the limit of zero undercut, while the efficiency is dramatically reduced, it does not fall to zero. This can be simply understood by observing that electrostatically $h = 0$ is not a physically important limit, as the conducting silicon is still $a/2$ from the ion.

As stated in section 2.3, in order to be experimentally useful, traps are

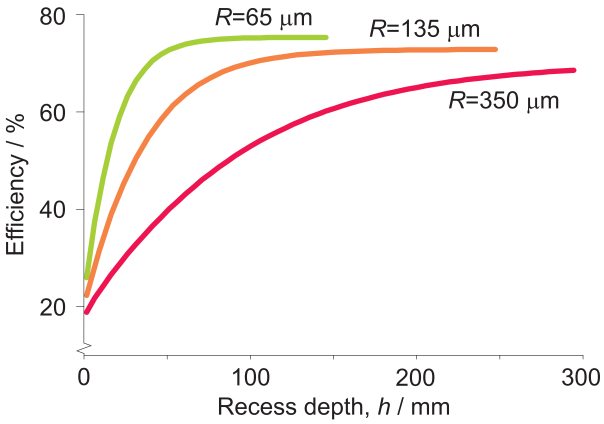

Figure 6.8: Trap efficiency as a function of recess depth and trap size. For large recesses ($h \gg R$) the efficiency tends asymptotically to its final value. This ultimate value is larger for smaller traps. In the limit as $h \rightarrow 0$, the efficiency remains non-zero.

required to have motional frequencies of a few MHz. Using the calculated efficiencies, the voltages required to operate traps of different sizes can be calculated from eq. 6.9. Examples of the RF voltage required for different trap sizes as a function of ω_{r} are shown in figure 6.9. For $R = 160$ μm, and requiring $q = 0.6$, a radial secular motional frequency of $\omega_{\mathrm{r}}/2\pi = 4.3$ MHz is realised using $V_0 = 160$ V and $\Omega_{\mathrm{T}}/2\pi = 20$ MHz, thus demonstrating that reasonable frequencies can be reached with achievable experimental parameters. Examples of some typical parameters for different sized traps are tabulated in table 6.2.

With the operation parameters quoted above, a stable string of four ions can have an axial frequency of up to 2 MHz (*c.f.* eq. 2.12). This requires endcap voltages of a few volts, which varies as a function of the segment length, b. If the trap segment is very long, then the ion experiences very little effect from the endcaps and, for a given endcap voltage, the axial motional

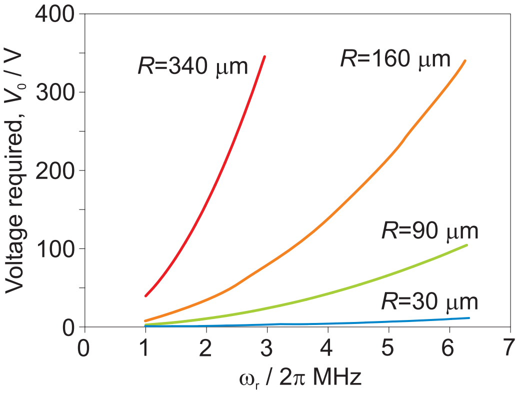

Figure 6.9: Voltage required to achieve a specific radial motional frequency for traps of ion-electrode separation in the range 30 μm $<$ R $<$ 340 μm, assuming $q = 0.6$, $h \gg R$ and $^{88}\text{Sr}^+$ ion species.

frequency is low. Conversely, if b is very small then the ion experiences very little effect from the (grounded) trap segment electrode, and again the axial frequency is low. It has been found that the length of trap electrodes that gives the highest axial frequency for a given endcap voltage is around $b \sim 1.4R$, as exemplified in figure 6.10.

The DC voltages applied to the four endcap electrodes lift the degeneracy of the radial motional modes. The principal axes of motion will then lie along the diagonal lines ($\underline{\hat{x}} \pm \underline{\hat{y}}$), and have frequencies split by a few hundred kHz. This orientation of the principal axes of motion is advantageous for cooling, as both radial degrees of freedom can be cooled by a single laser with a **k**-vector along the y-axis of the trap.

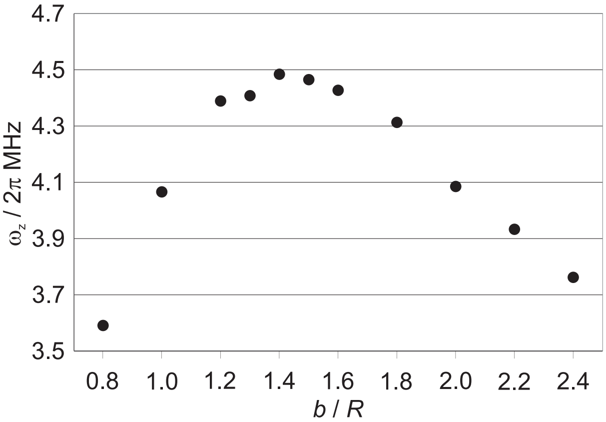

Figure 6.10: Axial frequency as a function of segment length. For both very long segments and very short segments curvature of the axial potential is low. The curvature (and so the axial motional frequency) is found to be maximised for a trap-segment electrode length of $b \simeq 1.4R$. There is an uncertainty in the calculated motional frequency of ∼5% introduced by interpolation within the meshed elements in FEMLAB. This graph shows axial frequencies for a trap where R = 160 μm; V_0 = 170 V; V_{DC} = 5.1 V; $\Omega_{\mathrm{T}}/2\pi$ = 21 MHz.

6.4.2 Trap depth

It is desirable that the trap depth be significantly greater than the kinetic energy of ions loaded directly from a thermal atomic source. This enhances the probability of loading ions, and minimises the likelihood of ion loss due to collisions with the background gas. In practice, this requires potential depths of ∼1eV.

To compare different-sized traps, Ω_{T}, V_0 and V_{DC} were chosen to ensure that up to 4 ions can be trapped in a stable linear string. The results for traps with R = 160 μm and R = 90 μm are summarised in table 6.2. The trap design presented here was also compared to a microfabricated trap which

Parameter	Value			Units
Trap size, R	160	90	30	μm
Ion	$^{88}\mathrm{Sr}^+$	$^{88}\mathrm{Sr}^+$	$^{111}\mathrm{Cd}^+$	
Wafer thickness, d	250	150	42	μm
Trap segment length, b	225	125	130	μm
RF voltage, V_0	170	54	8.0	V
Endcap voltage, V_{DC}	5.1	1.6	1.0	V
Trap drive frequency, $\Omega_{\mathrm{T}}/2\pi$	21	21	15.9	MHz
Radial motional frequency, $\omega_{\mathrm{r}}/2\pi$	4.5	4.5	5.0	MHz
Axial motional frequency, $\omega_{\mathrm{z}}/2\pi$	2.0	2.0	0.7	MHz
Trap depth	5.3	1.7	0.6	eV

Table 6.2: Summary of trap depths for different trapping conditions. For 160 μm and 90 μm traps the parameters V_0, V_{DC}, and Ω_{T}, were chosen to confine 4 ions in a 1D string with $\omega_{\mathrm{z}}/2\pi = 2$ MHz. For the 30 μm trap, the conditions were chosen to mimic those of [71].

has demonstrated successful operation; the calculation of trap depth was repeated running the model for proposed trap design under the same conditions (R, Ω_{T}, V_0 and V_{DC}) as were used for the high-aspect-ratio GaAs trap [71]. Under these conditions, the silica-on-silicon trap proposed here has a potential depth of 0.6 eV: seven times deeper than that of the GaAs trap. This demonstrates a significant advantage to be gained from a unit-aspect-ratio geometry.

The depth of the trapping potential was also modelled in 3D, in order to ascertain the effect of the endcap voltages. For the magnitude of endcap voltages being considered (see table 6.2) the trap depth was reduced only marginally ($\lesssim$3%). However, the calculation incurred a large uncertainty due to the coarser mesh necessitated by the much larger memory requirements of the 3D problem solver.

6.4.3 Micromotion compensation

Stray static charges that can build up on insulating surfaces near the ion can perturb the potential and these effects must be corrected for. The area of the bare insulating surfaces near the trap has been reduced as much as possible: the underside of the SiO_2 in the undercut is to be gold coated to within 50 μm of the silicon, and the silicon itself is grounded and doped to be highly conducting. Nonetheless, dedicated compensation electrodes are required to move the ion back to the trap centre if the potential is perturbed. The trap design allows independent compensation of micromotion in each trapping segment. This is achieved in the proposed design using:

1) compensation electrodes behind the RF electrode, and

2) an additional potential difference across the DC trap segment electrodes

(see figure 6.2).

The distance over which the potential minimum is expected to move as a function of applied compensation voltage was calculated using FEMLAB, and are illustrated for a trap with $R = 160$ μm in figure 6.11. By applying a voltage V_{C1} across the compensation electrodes (see figure 6.2), the potential minimum moves along the line 0.09 $\underline{\hat{x}}$ - 0.99 $\underline{\hat{y}}$. Applying a voltage V_{C2} across the trapping segment electrodes shifts the potential minimum in the direction $-0.71\ (\underline{\hat{x}} + \underline{\hat{y}})$. These are sufficient degrees of freedom to minimise micromotion in two dimensions. For example, an ion displaced by ($\Delta x =$

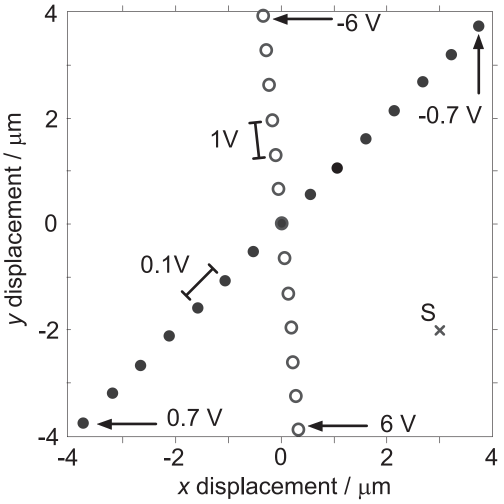

Figure 6.11: Displacement of the ion as a function of applied compensation voltage. For no applied compensation voltage ($V_{\mathrm{C1}} = V_{\mathrm{C2}} = 0$ V) the displacement is zero. The open points show the position of the trap minimum for increasing compensation voltage V_{C1} (with $V_{\mathrm{C2}} = 0$ V), where each successive point represents a 1V increase in voltage. The closed points do the same for V_{C2} (with $V_{\mathrm{C1}} = 0$ V) at 0.1 V intervals. The results shown are obtained with the trap parameters specified in table 6.2 for a trap of $R = 160$ μm.

-3 μm, $\Delta y = 2$ μm) from the trap axis because of stray charges, must be compensated by an opposite shift ($\Delta x = 3$ μm, $\Delta y = -2$ μm) to minimise the micromotion. Point S in figure 6.11 shows that this can be achieved using voltages $V_{\mathrm{C1}} = 6$ V, $V_{\mathrm{C2}} = -0.5$ V. The direction and magnitude of the effect for a given applied compensation voltage are different for V_{C1} and V_{C2} due to the different geometry of the electrodes: there is direct line of sight between the ion and the trap segment electrodes, while the compensation electrodes are shielded from the ion by the RF line.

In order to estimate the magnitude of the displacements which may be necessary in the new linear trap, the known behaviour of the existing endcap trap was modelled using SIMION 3D. The endcap trap (described in section 3.2) typically requires compensation voltages of ~10 V applied across the outer endcaps in order to minimise axial micromotion. (Note that the results reported in section 4.6.2 refer to a reduction in the variation of required compensation voltages, not in the required compensation voltage itself. Non-zero—though now very much more constant—compensation voltages are still required.) The effect of 10 V applied across the outer endcaps has been modelled and leads to a 4 μm translation of an ions equilibrium position. Assuming that such a displacement may also be required in the proposed linear trap, it is clear from figure 6.11 that this can be achieved with compensation voltages of a few volts.

6.4.4 Shuttling

To allow specialisation of different trap regions for tasks such as loading, storage or processing, and to physically move ionic qubits between interactions, it is required that ions can be shuttled between trapping segments. Electrode voltages can be found to smoothly shuttle the ion from one trap segment to another. An example of shuttling voltages, where the potential was required to be harmonic over a 200 μm range about the ion, is shown in figure 6.12. The maximum required DC voltage for a shuttling procedure is dependent upon the axial harmonicity required at the minimum; the range over which the potential is required to be harmonic; and the axial size of the electrodes.

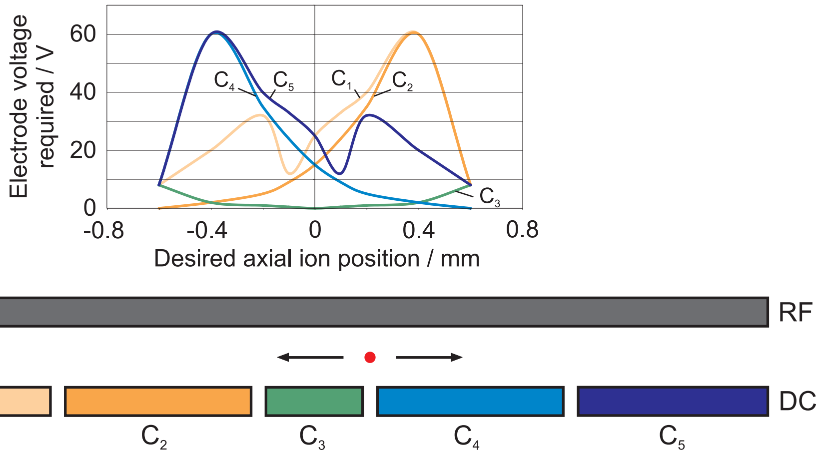

Figure 6.12: Example voltages for ion shuttling within a segmented trap. A trap of $R = 160\ \mu$m with a continuous RF electrode, and five DC segments of varying length was modelled (shown here schematically, on the same horizontal scale as the graph above). The voltages required to place the trap minimum at positions between the 2nd and 4th segments are shown. By applying these voltages as a function of time, an ion can be shuttled from one zone to another.

6.5 Practical considerations

The modelling described in sections 6.3–6.4 demonstrates that the proposed design will provide a suitable trapping potential, with motional frequencies and trap depths appropriate for QIP applications. Beyond this, there are several practical factors that must also be considered. Specific requirements of the trap include:

1) adequate dissipation of heat generated in non-perfect conductors and dielectrics;

2) electrical breakdown voltages which are well above required operating

conditions;

3) minimal ion-heating rate, $\dot{\bar{n}}$;

4) mechanical integrity of the structure.

These are now each addressed in turn.

6.5.1 RF heating of substrate

One of the reasons put forward for avoiding silicon-based technology is the power dissipated in the material [11, 76], as even highly-doped silicon has high RF loss compared to low-resistivity metals, such as gold. The proposed design is expected to circumvent these problems, as the electrodes themselves are made of gold rather than silicon; the silicon is simply used as a spacing material, and is isolated from the electrodes by a 15 μm layer of SiO_2. The RF loss is therefore expected to be a less significant problem than if the silicon were used as the electrode material [11, 156, 157]. At RF frequencies, however, there is a non-negligible capacitive coupling from the gold to the silicon through the SiO_2 dielectric, so heating in the silicon and SiO_2 layers must still be considered.

To calculate the heating effects due to this RF loss, each part of the trap was modelled as a lumped element, as shown in the circuit in figure 6.13. The lumped element approximation is valid since the trap features (< 5 mm) are much smaller than the RF wavelength ($\sim$10 m). The most significant elements are:

- the resistance of the gold tracks leading to the RF electrodes, R_A;
- the resistance of the gold RF electrodes, R_B;

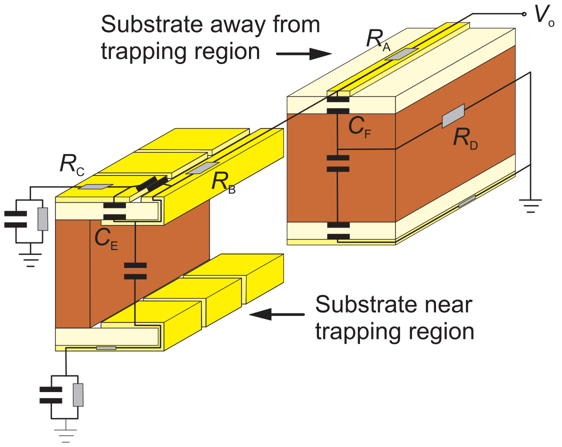

Figure 6.13: Lumped-element-circuit model of the trap showing the dissipative elements near the trapping region, and in the substrate away from the trapping region. The resistive and capacitive components that provide a significant dissipative contribution are labelled, and are explained in the text. Other elements drawn have been considered but were calculated to be insignificant.

- the resistance of the compensation electrodes, R_{C};
- the resistance of the silicon from the trapping region to ground, R_{D};
- the capacitance between the RF electrode and the compensation electrodes, through the SiO_2, C_{E};
- the capacitance between the gold track to the RF electrodes and the silicon substrate, through the SiO_2, C_{F}.

Other dissipative elements were also considered, but were found to be negligible compared to those listed here. To model the power dissipated in the trap structure, capacitances were calculated assuming the components consisted of either a pair of parallel plates or long thin wires, depending on which geometry was the closer approximation. The loss in the capacitors is due to the loss tangent of the SiO_2, $\tan\delta = 4\times10^{-5}$ [158], giving rise to an effective

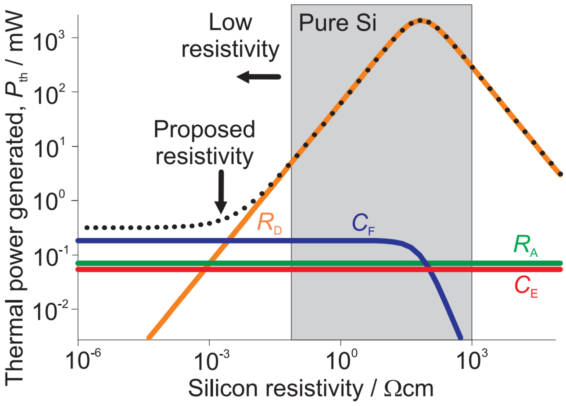

Figure 6.14: Power dissipated in the trap chip as a function of silicon resistivity. The contributions from components $\mathrm{R_A}$, $\mathrm{R_D}$, $\mathrm{C_E}$, $\mathrm{C_F}$ (as defined in figure 6.13) are shown by solid lines. The total power dissipated is given by the dotted line. At high resistivities, very little current flows through the silicon, and for low resistivities very little voltage is dropped across it. In both cases, power dissipation is low. However in the intermediate case, RF heating is significant. The grey box marks a range of resistivities for commercially available ‘pure’ silicon. Resistivities below this range can be achieved by doping.

series resistance.

The introduction of a dopant can change the silicon resistivity by several orders of magnitude. In the limit of the silicon having a high resistance, no current would flow through it, while in the limit of low resistance, no voltage would be dropped across it. In both cases very little resistive heating occurs, but between the two extremes significant amounts of heat may be produced. Using the circuit shown in figure 6.13, and for a trap with $R = 160\ \mu$m, RF electrode length, L_{RF}, of 3.2 mm (*c.f.* figure 6.3) and $\omega_{\mathrm{r}}/2\pi = 4.5$ MHz, the power dissipated in the various parts of the trap as a function of silicon resistivity is shown in figure 6.14. Pure silicon is near the worst case, with the total thermal power generated $P_{\mathrm{th}} \sim 1$ W. No significant reduction in heating occurs when the silicon resistivity is below $\sim 10^{-3}$ Ωcm, since losses in other materials dominate. Choosing this value of the silicon resistivity, $P_{\mathrm{th}} \simeq 0.4$ mW. With reference to figure 6.13, the dominant sources of heat are the resistances R_{A} and R_{D}, and the effective series resistances associated with capacitances C_{E} and C_{F}.

In calculating the upper limit to the chip's temperature rise due to 0.4 mW of generated heat, it is assumed that radiation is the only effective heat loss mechanism. The heat is generated in localised volumes within the chip, and must be conducted effectively throughout the chip to avoid excessive local heating. A very simple thermal transport model was developed to estimate the temperature gradient across the chip. By modelling each part of the trap as a lumped thermal resistance, a heat load of 0.4 mW leads to a temperature variation of less than 100 mK across the chip. The temperature rise is small because any heat generated in the thin $\mathrm{SiO_2}$ layer is well heatsunk to the gold and silicon layers, which are good conductors. Given this expected thermal uniformity, it is reasonable to model the chip as a blackbody radiator of uniform temperature, in a room-temperature heat bath. Of the chip's total surface area, around 50% is likely to be gold-coated tracks leading to the trap electrodes. Since gold has a very low emissivity ($\epsilon = 0.03$) compared to $\mathrm{SiO_2}$ ($\epsilon = 0.8$), only ∼50% of the surface area is therefore an effective radiator. For a 9 mm × 9 mm square chip, 0.4 mW of heat yields a 10 K temperature rise to 303 K.

This calculation has been performed for traps of other sizes. The RF electrode length, L_{RF}, was scaled with R and the chip size remained as

Parameter	Value			Units
Trap size, R	350	160	90	μm
RF voltage, V_0	250	170	54	V
Radial motional frequency, $\omega_\mathrm{r}/2\pi$	2.3	4.5	4.5	MHz
Thermal power generated, P_th	800	400	36	μW
Temperature gradient, $\mathrm{d}T/\mathrm{d}x$	40	20	1	mK/mm
Temperature rise, ΔT	16	10	1.2	K

Table 6.3: Summary of substrate-heating effects. Heating rates are calculated for a 9 mm × 9 mm chip, for a fixed number of segments, where the axial length, b, of each segment is scaled with R. As the traps are reduced in size, the thermal power generated in the traps is reduced, and the temperature rise due to a given number of trapping electrodes becomes smaller.

a 9 mm × 9 mm square. The results of this calculation are presented in table 6.3, and show that as the characteristic trap size, R, decreases, the thermal power generated and the chip's temperature rise also decrease. An approximate reasoning suggests that this is to be expected: for a constant motional frequency ω_r, $P_\mathrm{th} \propto R^4$ (because $P_\mathrm{th} \propto V_0^2$ and $V_0 \propto R^2$, *c.f.* eq. 2.8). In reality, as the trap size is reduced, not all the components are scaled in proportion. Specifically, the $\mathrm{SiO_2}$ thickness, and the gold thickness remain at a constant value. This means that the trap efficiency, η, is not constant, and the RF losses of different components do not scale exactly with size. A full calculation was performed to investigate how P_th scales with R, while maintaining a fixed motional frequency. The results, presented in figure 6.15, do indicate that $P_\mathrm{th} \propto R^4$ is in fact a good approximation. This scaling relationship applies to the thermal power generated by a single

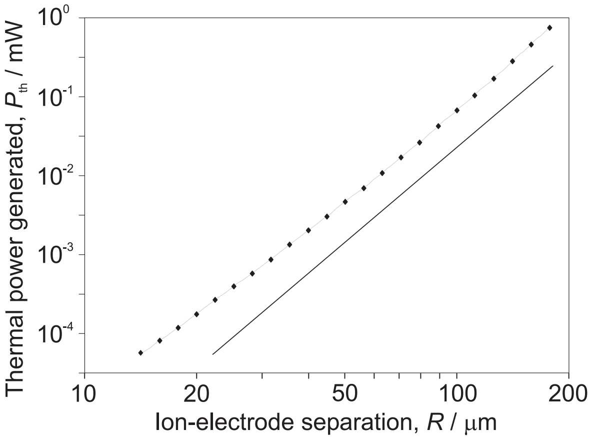

Figure 6.15: Power dissipated in the trap chip as a function of size. A simple model suggests that the power dissipated in the trap should scale with R^4 (see text), as indicated by the solid black line. The points show results of a full calculation using the circuit shown in figure 6.13 and demonstrate that the simple approximation holds reasonably well for this design.

linear trap comprising several segments. However, to realise arrays of ions stored and manipulated in a large number of interconnected traps [34], the areal density, n_{a}, of unit-aspect-ratio traps on a single chip will need to increase. The total thermal power generated on chip, P_{tot}, scales with the areal density according to $P_{\mathrm{tot}} \propto P_{\mathrm{th}} n_{\mathrm{a}}$. Since $n_{\mathrm{a}} \propto R^{-2}$, then $P_{\mathrm{tot}} \propto R^2$. As R decreases to enable devices of increasing density and complexity, P_{tot} and the resulting temperature rise are therefore not expected to limit the device performance.

6.5.2 Electrical breakdown

There are several places in the trap where the RF electrode is in close proximity to a conductor at RF ground. It must therefore be ensured that, under the operating conditions required, there is no danger of electrical breakdown. The most likely point for breakdown is expected to be between the RF electrode and the compensation electrodes, across the surface of the SiO_2. At this point the electrodes are close, and surface effects can mean that arcing along the SiO_2-vacuum interface can occur at much lower voltages than would be possible through either vacuum or bulk SiO_2 alone [159]. This effect is not well understood, but is known to be dependent on many factors including the RF frequency, the geometry, surface finish, adsorbed gases in the material and any history of previous arcing events. Blackburn *et al.* [160] report devices with a DC breakdown field of $\sim$430 V/μm across an SiO_2-vacuum interface. Results showing an AC (100 MHz) breakdown field of $\sim$ 30 V/μm between sharp-edged electrodes through vacuum were presented by Gerhard *et al.* [161]. Given the uncertainty regarding surface breakdown effects, the proposed design uses a 50 μm separation between the RF and compensation electrodes, resulting in a maximum AC electric field of 5 V/μm. We conclude that this should be sufficiently low to avoid surface flashover and vacuum breakdown at a few tens of MHz.

6.5.3 Ion heating

The most significant process contributing to the heating of the ions' motion is thought to be fluctuating patch potentials on the electrode surface. This is far from understood, although observations indicate that the ions' heating rate, $\dot{\bar{n}}$, is inversely proportional to R^4 [72, 110]. For metallic electrodes, surface quality is also thought to be a significant parameter affecting patch potential fluctuations. The trap design proposed here uses electrodes of gold-coated SiO_2 which, after electroplating, will have a surface roughness of < 10 nm RMS. This figure is entirely limited by the electroplating process and not by the surface quality of the SiO_2. This compares favourably with other traps in the literature (*e.g.* [50]), and should help minimise the ions' heating rate [96].

6.5.4 Mechanical integrity

When a voltage is applied to the RF electrode there is an attractive force between this electrode and the DC electrodes on the opposite side of the wafer due to image charges. The electrodes are therefore mechanically driven at twice the trap drive frequency, $2\Omega_\mathrm{T}/2\pi$. It must be ensured that any mechanical resonances of the electrodes are far from this frequency. To calculate this, the electrodes are modelled as SiO_2 cantilevers of uniform rectangular cross section with thickness w, and length h. These will have a resonant frequency of [162]:

$$\frac{\omega_\mathrm{res}}{2\pi} = 0.16\frac{w}{h^2}\sqrt{\frac{E}{\rho}}\ , \tag{6.18}$$

where $E = 73$ GPa [158] is the Young's modulus of SiO_2, and $\rho = 2.2 \times 10^3$ kg m^{-3} [158] is its density. For a trap with $h = 300\ \mu$m, $w = 15\ \mu$m (see figure 6.3 and table 6.1), this gives a resonant frequency of 150 kHz. Given that the cantilever is expected to have a mechanical Q of several thousand [163], this should be sufficiently far from $2\Omega_\mathrm{T}/2\pi$ to avoid resonant effects.

It must additionally be ensured that the force acting on the cantilevered electrode will not give rise to mechanical failure. Following [70, 164], when far from resonance, so that only the DC deflection of the electrode need be considered, the maximum voltage which can be applied before the electrode fails, V_0^{Max}, is given by:

$$V_0^{\mathrm{Max}} = \frac{dw}{h}\sqrt{\frac{\sigma}{\epsilon_0}} \tag{6.19}$$

where $\sigma = 50$ MPa is the ultimate tensile strength of silica [158]. For typical trap dimensions (table 6.1) with $h \sim R$, this has a value of several tens of kV. This is well outside the planned operating region.

6.6 Summary

A design for a novel, monolithic, linear RF ion trap has been described. The three-dimensional symmetric trap structure, to be microfabricated on a chip using silica-on-silicon processing techniques, is of significant interest for implementations of QIP using trapped ions. The trap electrodes are formed by gold-coated SiO_2, and are spaced by highly-doped silicon.

Finite-element modelling has shown that under practical operating conditions, the trap design provides deep potentials with motional frequencies of several MHz. The design also incorporates the means to compensate micromotion independently in each of the chip's trapping segments. Heating of the trap chip due to RF loss has been investigated, and is not anticipated to be a factor that limits the trap's performance, even in traps with larger ion-electrode distances. The dimensions have been chosen such that the electrical failure due to RF breakdown, and mechanical failure should not be of concern. Finally, the surface of the electroplated gold which forms the electrode material should be of sufficient quality that it does not aggravate to excessive ion heating.

The microfabricated trap design detailed in this chapter has specific advantages over surface electrode traps [76, 77] and the high-aspect-ratio GaAs chip trap [70, 71]. The unit-aspect-ratio trap results in a significantly greater trap depth compared to the surface trap and the GaAs trap (up to a factor of ∼7 deeper in the latter instance). A further consequence of the design is a greater trap efficiency; the unit-aspect-ratio structure presented in this work has an efficiency twice that of the GaAs trap. As in the surface electrode trap, the gold electrodes in our trap design have a low resistive impedance, and the SiO_2 dielectric has a low capacitive reactance. These features result in RF losses (and subsequent heating of the trap chip) that are calculated to be significantly lower than in the GaAs trap. Thus our design for a monolithic unit-aspect-ratio trap is expected to exhibit a deep potential well, a high trap efficiency, and a low RF loss, which contrasts with some features of the other microfabricated traps. These differences will contribute to an increased understanding of ion trap materials and structures for QIP applications.

CHAPTER 7

Trap fabrication

7.1 Introduction

This chapter describes the progress towards the fabrication of a novel, monolithic, linear, RF ion-trap chip. Scalable trapped-ion quantum computing requires an architecture that is scalable to many ions, and one method of realising this uses microfabricated, segmented linear traps. Plans for such an architecture have been proposed [34, 150], though the fabrication of truly scalable systems remains a significant challenge. It is proposed that the 3D trap structure outlined in chapter 6 can be microfabricated using a process based on planar silica-on-silicon techniques. The trap electrodes are made of gold-coated silica (SiO_2) and spaced by highly-doped silicon in a monolithic structure. Once demonstrated, the fabrication processes used are scalable to enable handling of many ionic qubits.

The work presented in this chapter was carried out in cooperation with the Centre for Integrated Photonics (CIP) in Ipswich. Working together an initial concept was arrived at, which NPL was satisfied would act as a trap, and which CIP believed was fabricable. Following the modelling described in chapter 6, NPL presented CIP with the design specifications and CIP proposed the original fabrication process to achieve this design. CIP also carried out all of the initial fabrication work. Work has been done at NPL to inspect the results of these fabrication efforts, model the effects of any artefacts not originally envisioned, and provide feedback to CIP regarding the impact of any fabrication difficulties upon the physics of the problem. Possible modifications to the design or the fabrication process were then worked out in discussion between NPL and CIP. Latterly, Patrick See (of NPL, working at the University of Cambridge) has worked directly on process development.

This chapter is organised as follows. The work already carried out by other groups into ion-trap microfabrication is reviewed in section 7.2, and the potential advantages offered by the proposed fabrication method are highlighted. The original concept of the fabrication process is explained in section 7.3. The progress which has been made towards realising this process, along with the difficulties encountered, and the changes which have been made are summarised in section 7.4. This section also includes work towards fabricating "intermediate" traps to demonstrate principal aspects of operation. Section 7.5 outlines the remaining work required to realise a functioning silica-on-silicon microtrap.

7.2 Review of microtrap fabrication methods

Traps have been successfully fabricated in other groups using gold-coated alumina [24, 50, 72, 73] . Such traps have been used to demonstrate trapping of a linear string of ions, separation and recombination of small groups of ions [24, 50, 73], basic algorithms carried out over spatially distinct locations [24, 50], and shuttling of one or more ions through junctions [73]. There remain, however, two significant fabrication limitations. Firstly, the traps consist of several separately fabricated layers which must be assembled following the wafer processing. This is non-ideal particularly for larger, more complex trap arrays. Secondly, the machining of alumina is a serial process; the work required increases in proportion to the size of the trap array. A two-layer ion trap, with electrodes of boron-doped silicon spaced by borosilicate glass, has also been demonstrated [11], but this too requires post-processing assembly of the electrode and insulator layers.

Geometries suitable for monolithic microfabricated ion traps include asymmetric planar electrode structures [76], and symmetric, three-dimensional high-aspect-ratio GaAs structures [70]. Operational ion traps based on these geometries have been demonstrated [71, 77]. The latter geometry is perhaps more demanding to fabricate than the former, however it enables greater optical access and results in a deeper trapping potential. This thesis proposes a symmetric trap geometry that is also monolithic and suitable for microfabrication, but which possesses additional advantages over the GaAs semiconductor chip trap demonstrated by Stick *et al.* [71]. Specifically, the fabrication process is capable of producing a trap with unit aspect ratio, which resulting in a deeper trapping potential (up to $\sim$7 times that of the GaAs trap) while maintaining adequate optical access ($f/\# = 1$). In addition, it uses metallic electrodes and a low-loss dielectric, resulting in significantly lower heating of the ion-trap chip. Using silica-on-silicon processing techniques, it may ultimately be possible that this design could be used to create traps where the characteristic ion-electrode separation, R, varies by over an order of magnitude in the range $350\ \mu\text{m} > R > 20\ \mu\text{m}$.

Other groups are also investigating alternative microfabrication approaches. For example, Slusher [165] has been developing planar ion traps constructed on a p-doped silicon wafer; the electrodes are tungsten/aluminium conductors and are spaced by silicon nitride (Si_3N_4; SiN) and SiO_2 dielectrics. Compatibility with CMOS technology is one of the criteria central to this design. MEMS (Micro Electro-Mechanical Systems) techniques have been employed by Blain *et al.* [166–168] to develop planar segmented traps; the trap is constructed on a silicon substrate, has gold-coated tungsten electrodes and uses SiN and SiO_2 dielectrics. Three-dimensional trap configurations are possible using MEMS processes.

7.3 Planned fabrication method

The basic trap structure has been described in section 6.2, and is illustrated in figure 6.3. This structure can be microfabricated using planar processing techniques developed in the semiconductor industry. For reviews of standard processing techniques available see [169, 170]. The processing steps required for the proposed trap involve standard techniques, although some are used in a novel context. To fabricate the proposed trap design, a silicon wafer is oxidised and then processed using lithographic patterning, isotropic and anisotropic etching, and metallic evaporation and electroplating. A simplified version of the processing stages is illustrated schematically in figure 7.1. These stages are now outlined sequentially.

1) Thermal oxidation of double-sided-polished n-doped silicon wafers, resulting in a 15 μm thick layer of SiO_2 on both surfaces of the silicon wafer. This is followed by an inductively coupled plasma (ICP) reactive ion etch (RIE) through the SiO_2 to produce SiO_2 “windows” at the corners of each chip. These allow metal pads on the silicon for grounding purposes. (These pads are well away from the trapping region, and for clarity are not shown in figure 7.1. They can, however, be seen in figure 7.2.)

2) Evaporation of 500 nm of gold onto SiO_2, resulting in the electrode pattern. 50 nm of titanium is laid down as a base layer on the SiO_2, prior to the gold evaporation, to ensure the gold adheres to the surface. A 150 nm thick nickel mask is also laid down on top of the gold to protect it during step 4.

3) ICP RIE etch of SiO_2 to expose the silicon where the volume of free space is required and to create individual segmented DC electrodes. The features are masked with a standard photoresist called SU8.

4) Isotropic SF_6 RIE etch of silicon to create the clear aperture through the structure and the free-space undercut between the two parallel SiO_2 layers. A fresh SU8 mask is applied for this step.

5) Shadow evaporation of titanium and then gold to coat the edges and surface of the SiO_2 in the undercut. This creates a continuous surface of gold from the outside of the electrodes to the underside. A nickel mask is then evaporated onto gold surfaces of the DC electrodes in the undercut.

6) Removal of SU8 mask, wet etch of the titanium and gold between the DC segments, then removal of the nickel mask. A further wet etch of silicon ensures no electrical connection between the gold in the undercut and the silicon.

7) Electroplating of gold electrodes to a thickness of 5 μm, with surface roughness < 10 nm RMS.

The steps described involve standard techniques, although some are used in a novel context. Two steps are notable in this regard. The first is the through-etch of the wafer to create a 3D structure from an otherwise planar piece (step 4). The second is gold coating the underside of the SiO_2 cantilevers (step 5). Extending the design to incorporate many segments of varying sizes is simply a matter of mask design; increasingly complex traps do not necessarily lead to increased complexity of fabrication. For clarity only three segments have been shown in figure 7.1, though the full trap designs can have many more segments. Figure 7.2a shows an example of a trap from the current fabrication run, with 10 independent trapping zones, and a loading region. The parallel nature the processing means that this is essentially no more difficult or time consuming to fabricate than a trap with a single trapping zone. Furthermore, a 100 mm diameter wafer can produce 60 chips,

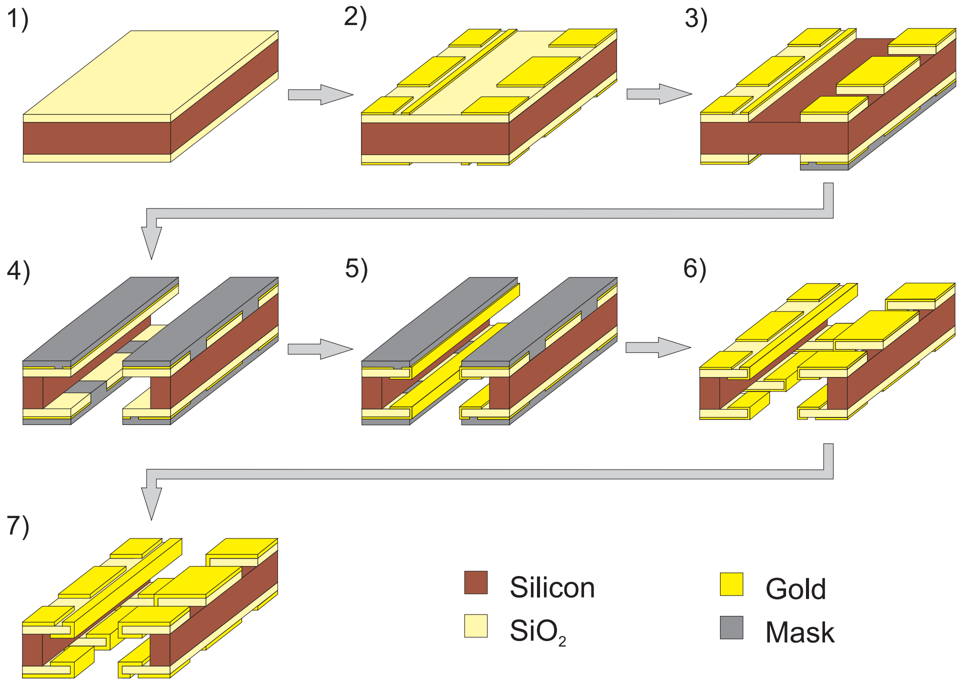

Figure 7.1: Outline of fabrication process. This begins with thermal oxidation of a silicon wafer and is followed by a series of steps consisting of lithographic patterning, anisotropic etching of SiO$_2$, isotropic etching of silicon, and metallic evaporation and electroplating. The specific steps of the process are detailed in the text.

where not all chips need be of the same design. Figure 7.2b shows an example of a design planned for a future fabrication run. The qualitative change from linear traps to junctions will require more complex fabrication methods, particularly for the undercut (step 4) and shadow evaporation of gold (step 5). Both of these steps in the linear design can be treated as two-dimensional problems; they are axially invariant. However, in the junction design it is not necessarily clear how the processes will behave near a junction structure. For example, the etchant may well behave differently when attacking a plane surface compared to when attacking a corner. These steps will therefore need careful process development.

The trap designs specified by figure 6.3 and table 6.1 (with wafer thicknesses in the range 150 μm $\rightarrow$ 500 μm), are expected to be achieved using existing processes, or modifications thereof. The processes do, however, set limits on the degree to which particular parameters can be varied. The maximum SiO_2 layer thickness in our design is limited by the rate at which it can be grown. The duration of the thermal oxidation process increases exponentially with the required oxide thickness. For example, 1 μm of SiO_2 can be grown in $\sim$3 hours, while the 15 μm used in our designs takes 24 days. This thermal oxidation process is used in the fabrication of photonic devices containing silica-on-silicon planar lightwave circuits (typically constructed on a plane of 16 μm thick SiO_2). The low-loss optical quality of resulting devices demonstrates the low density of defects present in the thermal oxide, together with the uniformity of the oxide density. It may be noted that other oxidation techniques, such as high pressure oxidation, can deposit SiO_2 faster, although these oxides are of a lower optical quality than thermal oxides. If

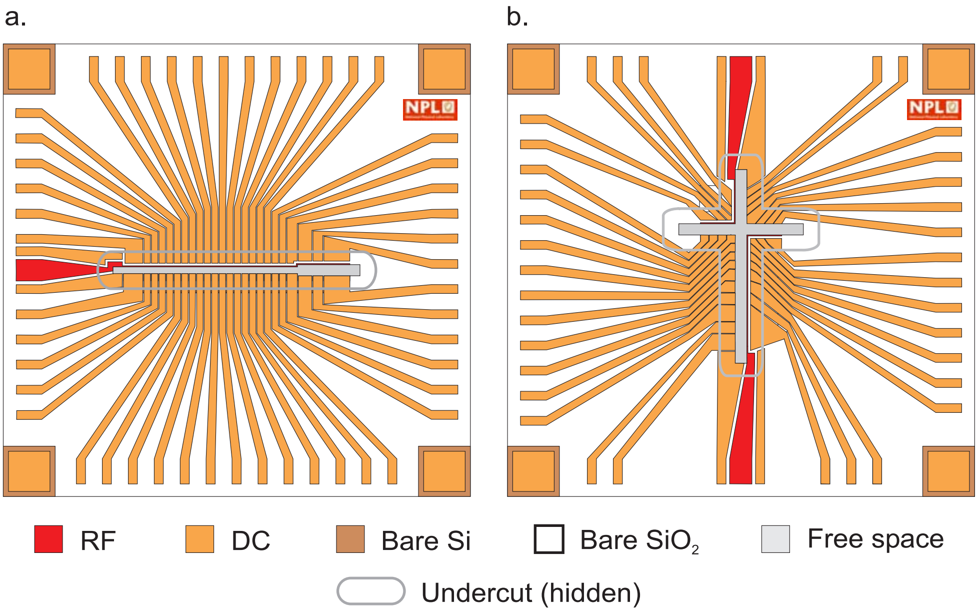

Figure 7.2: Examples of trap-chip designs. The designs shown are 9 mm to a side. (a) shows a design for a 150 μm-thick wafer, with 10 independent trapping regions (left hand side of the free space) and a wider loading region (right hand side of the free space). (b) shows a design for the next fabrication run. The junction design will need more processing steps, (*i.e.* the same steps, but repeated for both the upright and transom of the cross) and will require additional process development, beyond that of the linear traps exemplified in (a).

the SiO_2 layer is made significantly thicker then mechanical resonances may become important (*c.f.* eq. 6.18). The minimum SiO_2 thickness is set by RF heating considerations (described in section 6.5).

Presently, the minimum wafer thickness ($d \sim 150$ μm) is set by the decreasing yields expected for increasingly thin and fragile wafers. This limit may be overcome by further process development, or by using silicon-on-insulator (SOI) fabrication methods. The dimensions of the gold features in the xz-plane are constrained by the fabrication process to be greater than or equal to the gold-layer thickness. The 5 μm thickness of the gold layer is chosen to ensure that the resistance of the RF lines is sufficiently small to avoid excessive resistive heating. This constraint can, however, be relaxed in smaller traps where the required RF voltages are smaller. Further details of this reasoning are given in section 6.5.

7.4 Fabrication progress

The fabrication methods proposed in this chapter aim to create traps with a 3D structure by making use of processing technologies that were originally developed for planar devices. Prior to any process development, the major uncertainties were expected to be associated with:

1) the silicon through-etch and under-etch,

2) the SiO_2 fingers' structural integrity,

3) shadow evaporation of electrodes' inside surface.

Fabrication development has been dominated by these steps; the difficulties encountered and associated progress are now described.

7.4.1 Silicon through-etch and under-etch

In the very first instance it was envisaged that the removal of the silicon from the trapping region (step 4) could be achieved in two stages. First using an anisotropic (KOH) etch through the silicon, followed by an isotropic, wet etch to create the undercut. Following a trial of this two-stage method it is believed that the KOH and isotropic wet etch affect integrity of SU8. An alternative method requiring a single, dry SF_6-based silicon isotropic etch was therefore pursued to provide the under-etch.

Using such an isotropic etch, the process was performed in equal measures from each side of the wafer. After breakthrough of the aperture, the etch virtually stopped. This left a sharp silicon "knife edge" around the perimeter of the aperture in the plane of the wafer, exactly halfway through the wafer thickness. Figure 7.3a shows the cross-section of the wafer and illustrates how the isotropic silicon etch is expected to proceed, resulting in the silicon being etched back underneath the SiO_2 layers. Figure 7.3b shows the initial extent of the knife edge formed after the through-etch, unable to proceed due to the cessation of the etch following breakthrough. A scanning electron microscope (SEM) image of this knife edge on one trap chip is presented in figure 7.4, which clearly shows that the etch is not isotropic as expected. After varying the RF power during the RIE etch the etch-back now reaches a depth of $\sim 150\ \mu\text{m}$ (see figure 7.3c). From finite-element modelling (section 6.4) it

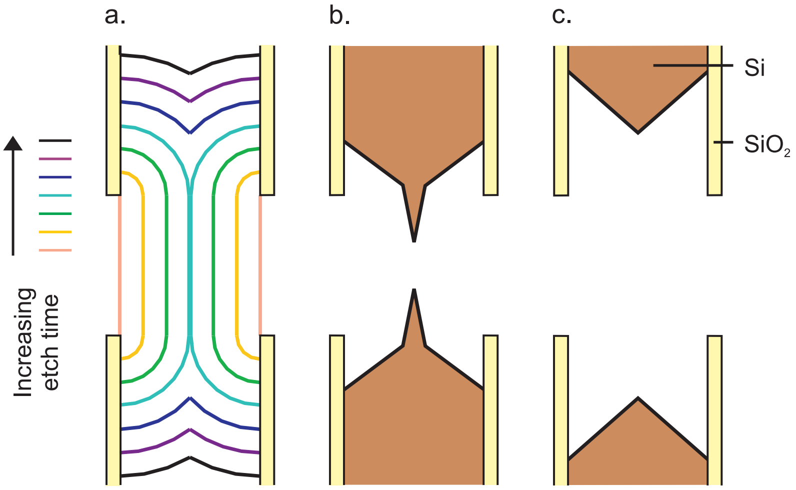

Figure 7.3: Progress made with “isotropic” etching of silicon. Schematic cross-sections of the wafer around the aperture illustrate: (a) hypothetical evolution of the isotropic etch, (b) results observed initially, where the etch stopped once the wafer had broken through, and (c) results observed after further investigation. The improvement was largely due to better optimising the RF power during the RIE etch.

is clear that the latest under-etch results should provide a usable trapping potential, though it is not ideal.

7.4.2 Mechanical integrity

The modelling presented in section 6.5.4 suggests that under normal operating conditions the cantilevered electrodes should not fail mechanically. However, the stresses to which the structures are subjected during fabrication are very different to those of standard trap operation. Difficulties have been encountered with the SiO_2 fingers breaking off at various stages of the fabrication process. Examples of this, and the progress made, are illustrated in figure 7.5. The main problems arising were:

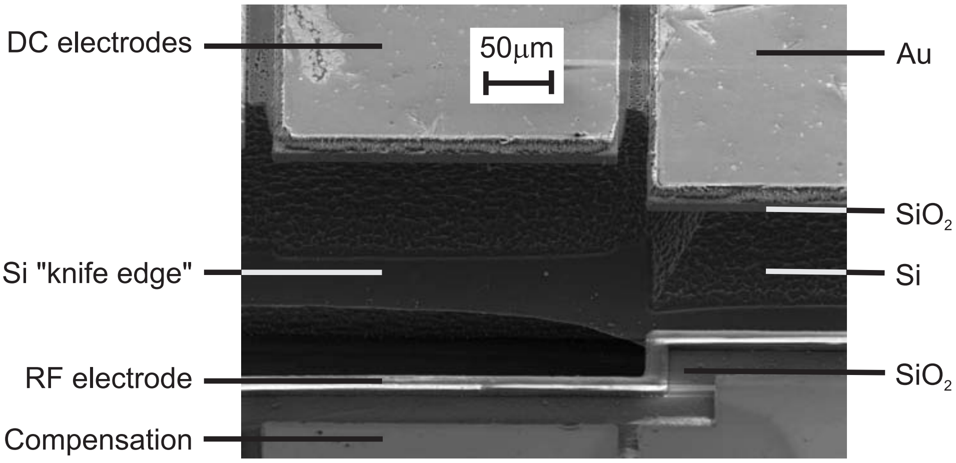

Figure 7.4: "Knife edge" problem during under-etch development. SEM image of a trap structure following "isotropic" SF_6 RIE etch (figure 7.1 step 4). The image shows DC electrodes and the RF electrode at the boundary between a loading zone and another trapping zone. The viewing angle of 45° from the normal shows the silicon knife edge and the silicon surface which has been etched anisotropically.

1) The initial techniques for holding the processed wafer while dicing it into individual chips was to mount it onto a mylar backing. This caused breakage and removal of SiO_2 electrode fingers, as shown in figure 7.5a. This has been solved by using an alternative mounting technique during dicing whereby the processed wafer is held on a substrate using a water-soluble wax.

2) The RF electrode was broken off due to the etch process attacking the SiO_2 during the silicon etch, as shown in figure 7.5c. This etch was expected to attack SiO_2, but at a rate of only 1% of that for silicon. Several possible solutions exist, including increasing the initial oxide-layer thickness. To date the problem has been reduced by better

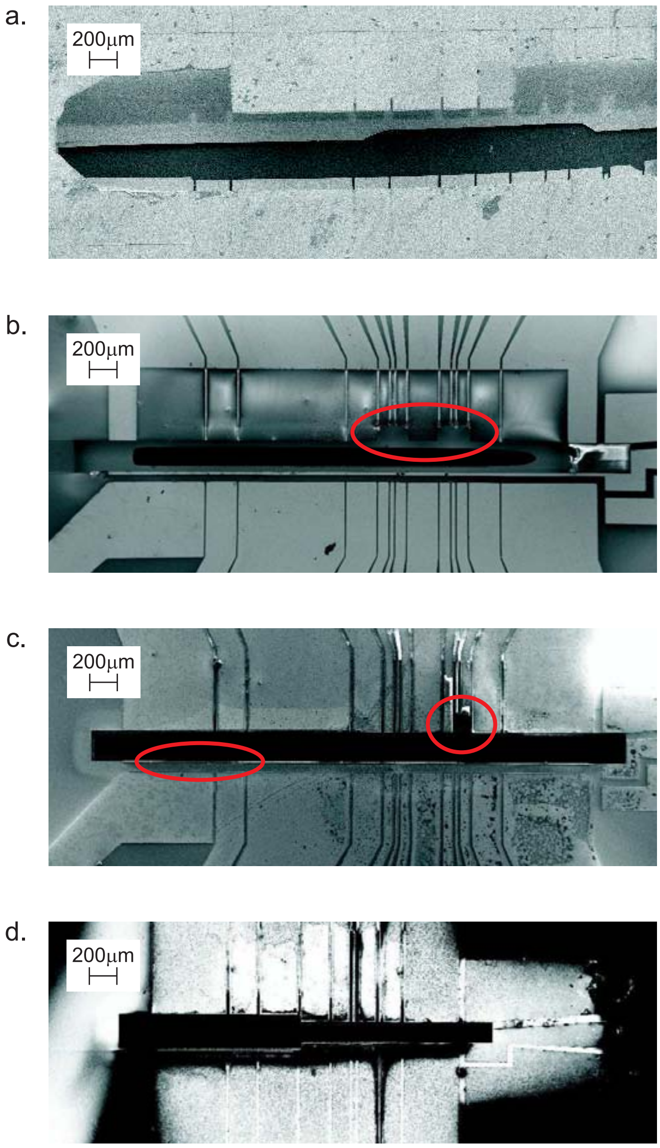

Figure 7.5: Progress made with integrity of cantilevers after processing. SEM images show trap apertures and electrodes following the through-etch processing step. In chronological order of development, (a) shows the extent of finger breakage using the original dicing technique, (b) shows that all of the narrow electrodes have been broken and (c) shows the RF electrode is no longer present along portions of the trap. (d) demonstrates that all electrodes are intact on at least some traps in the latest processing iteration.

optimising the parameters of the silicon etch.

3) The removal of the SU8 mask causes finger damage for several reasons. The mask expands during the lift-off process. The SU8 between the fingers therefore stresses the SiO_2 causing the fingers to break off. This is a particularly significant problem for the thinnest of the fingers. In addition, if the SU8 does not fully delaminate from the wafer it can pull fingers off with it when it comes away. Under normal processing for photonics components a small amount of SU8 remaining on the surface is not necessarily a problem. However, for trap applications the additional insulator in the region of the trap is unacceptable. The additional steps required to ensure that the SU8 is fully removed (*e.g.* fuming nitric acid) are prohibitively harsh to the trap structure.

   SU8 was originally chosen as a mask because it is able to planarise the deep (15 μm, unit aspect ratio) features etched in the SiO_2. However in the light of the difficulties encountered with the SU8 removal here, and additional problems caused by the SU8 outlined elsewhere in this chapter, it is believed that alternative masks may be more suitable. The mask AZ9260, for example, is used as a thick photoresist in bulk micromachined MEMS structures, and will be trialed for use in the present context.

7.4.3 Shadow evaporation and electroplating

The technique of shadow evaporation was proposed to coat gold onto the SiO_2 surfaces inside the aperture. By evaporating gold towards a tilted wafer,

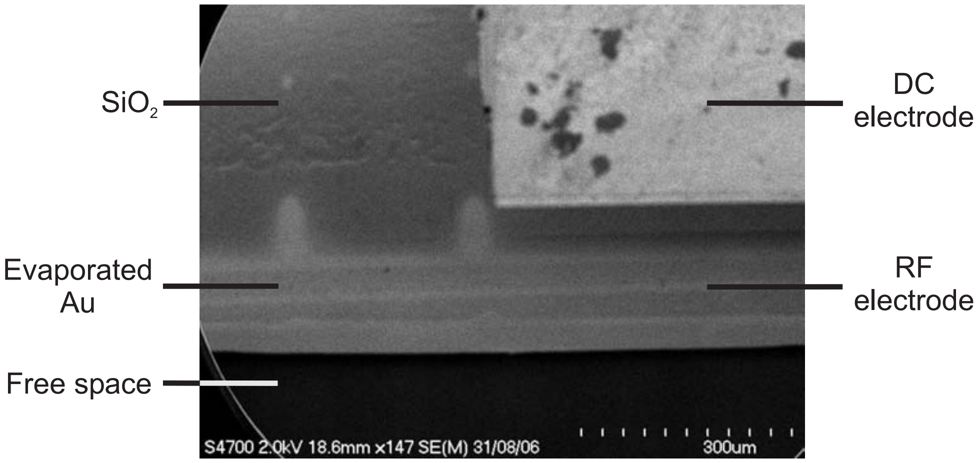

Figure 7.6: Shadow evaporated sample. SEM image of the trap chip viewed at an angle of 25° from the normal, and shows the gold coating on the underside of the RF electrode. DC electrodes originally existed on the left of the picture, and masked the RF electrode, as indicated by the well-defined edge of evaporated gold. These DC electrodes were broken off in the mask lift-off stage of the process.

the electrodes on the top side of the wafer mask the inside surfaces of the electrodes on the bottom side. The angle of tilt controls the area of this inside surface that is coated. The technique can be used on both sides of the wafer to coat all of the SiO_2 surfaces. The use of existing structures to shadow-mask certain regions during evaporation of metals (including gold) is an established and controllable technique. It has been used for some time in the fabrication of high contrast grating structures [171], and provides a high quality surface finish [172]. It has also been used to fabricate thin film microstructures [173]. This technique has been tested and demonstrated to work as anticipated. Figure 7.6 shows an SEM image of such a test.

Electroplating of evaporated gold initially resulted in a surface that had

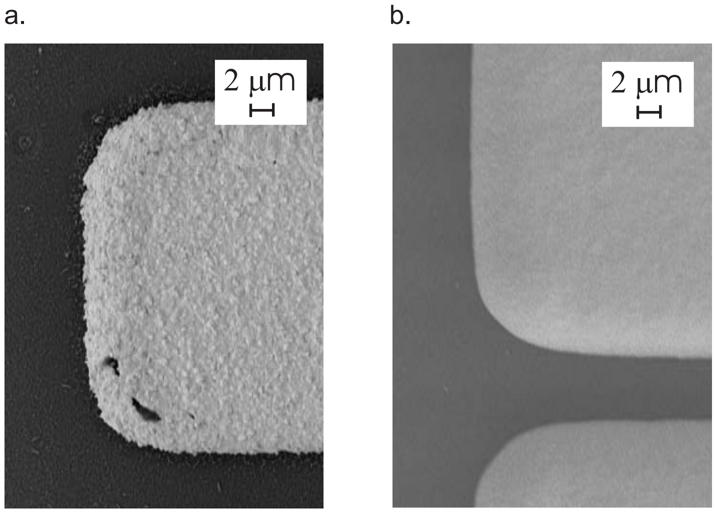

Figure 7.7: Progress with quality of electroplating. SEM image of electroplated gold (a) using initial standard process, and (b) using Metalor ECF64 electroplating solution. The latter shows a much smoother surface.

feature sizes of ∼1 μm. An SEM image of such a sample is shown in figure 7.7a. This is a relatively rough surface, and its reflectivity is much less than that of evaporated gold. A dramatic improvement was observed when using the Metalor ECF64 electroplating process. Using this, gold tracks appear much brighter with reflectivities of 80-90% and look more like evaporated gold. Surface roughness is less than 10 nm RMS. Uniformity is very good across the wafer with a standard deviation in thickness of less than 2% for 7 μm thickness. Such a sample is shown in figure 7.7b.

7.4.4 Intermediate traps

Given the difficulties described above, an "intermediate" trap fabrication method is being investigated. This proceeds as before for steps 1–2 (figure 7.1). The through-etch of the silicon is then achieved by an anisotropic Bosch process [174]. This consists of short, alternating phases of isotropic etching and passivation, resulting in a vertical-walled aperture. In the first instance, this structure could be electroplated immediately after Bosch processing, thus removing the requirement for under-etching and shadow evaporation. It would also mean that the electrodes would be supported during the mask-removal steps. There are, however, several limitations to the performance of such a design. Firstly there would remain a 15 μm-wide strip of exposed, insulating SiO_2 along the front edge of each electrode. It is not clear how significant such a region of bare insulator would be, but it is considered best practice to minimise the surface of bare insulators as far as possible. Secondly, the trap would have a grounded, conducting surface at a distance $R/\sqrt{2}$ from the ion and the efficiency would be reduced to around 25% (*c.f.* figure 6.8). This would in turn require either that the RF trap voltage be three times higher, or that the ions' motional frequencies are lower by a factor of three (or some compromise of the two. *c.f.* eqs. 2.11, 6.9). The substrate heating has been modelled for the intermediate trap design (following the same method as outlined in section 6.5.1) and is not expected to be worse than in the main design. Without any gold in the undercut the much narrower RF electrode has a significantly larger resistance. Most of the current therefore flows to ground in the substrate away from the trapping region (C_{F},

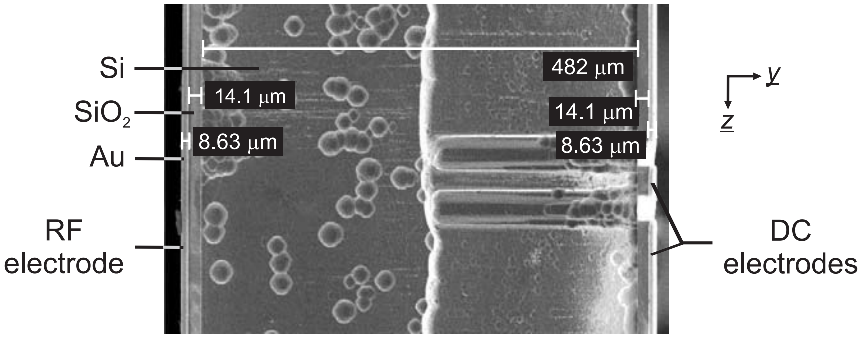

Figure 7.8: Bosch processing. SEM image of a Bosch-processed wafer, viewed from the trap axis, looking towards the electrodes in the plane of the wafer. The silicon has been etched from both sides. The line along the middle of the trap is where the vertical sidewalls etched from each side of the wafer do not meet perfectly due to imprecision of initial mask alignment. The pits seen on the left are thought to be from a slightly prolonged dip in an aggressive polishing etch, which can be avoided in future work.

R_{D}, figure 6.13). While increased heating may be expected due to the higher resistance of R_{A} and the increased current through the substrate, this is offset by the much lower current flowing through R_{A}, and the effective removal of any capacitive coupling through the $\mathrm{SiO_2}$ near the trap, C_{E}. While the limitations of the bare insulator and the reduced efficiency are undesirable for a final trap design, there remains a significant amount of work and testing which could be accomplished with such an intermediate design.

Ultimately the Bosch process could be followed by an isotropic under-etch and then processing steps 5–7 (figure 7.1) can be carried out as described previously. Initial tests of the Bosch process have been carried out and produce vertical sidewalls as expected. An SEM image of a sample structure is shown in figure 7.8.

7.4.5 Trap mounting

In parallel with the work of this thesis, a system of mounting the trap into an ultra-high vacuum (UHV) chamber has been developed by Guido Wilpers. The system is briefly outlined here. The microtrap must be mounted inside a vacuum chamber which is pumped to low pressure (10^{-11} mbar $\simeq$ 10^{-9} Pa). and which allows adequate optical access for the incident lasers beams required. The chip itself has electrodes on both sides of the wafer which must be connected via filters to control electronics outside the vacuum chamber.

The chip will be mounted on an intermediate aluminium nitride (AlN) substrate. While alumina is more standard and easier to machine, the thermal expansion coefficient of alumina and SiO_2 are very poorly matched, leading to the possibilities of poor adhesion and damage to the chip during the bake-out procedure. By contrast, the thermal expansion of AlN is very well matched to that of SiO_2. The intermediate substrate contains electrical tracks and vias to position all of the trap's electrode connections on the upper surface of the substrate. The intermediate substrate is then mounted into a standard-sized 64-pin ceramic leadless chip carrier (CLCC), measuring approximately 30 mm × 30 mm × 2 mm (inner cavity dimension of 11.92 mm × 11.92 mm). Custom laser machining of the CLCC is required to provide optical access to the trap chip from both sides, and also to ensure adequate vacuum pumping on both sides of the chip. The CLCC is then assembled into part of a small UHV chamber. This entire assembly is illustrated in figure 7.9

This mounting approach allows maximum optical access to both sides of

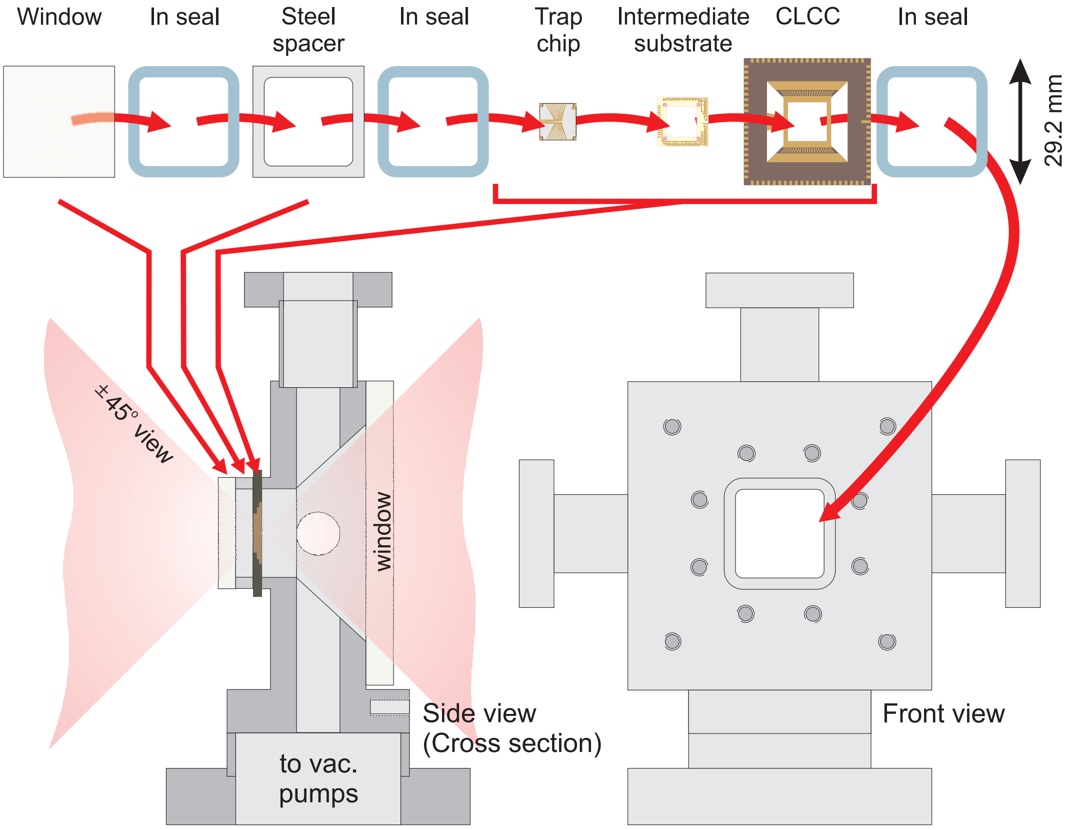

Figure 7.9: Microtrap mounting and vacuum chamber setup. The trap chip is mounted on an intermediate substrate to bring all electrical connections on to one side of the device. This is then mounted in an 84-pin CLCC, custom machined for optical access and vacuum conductance. The CLCC is mounted onto the front of a custom-machined chamber, with seals being formed by indium wire. A filter board consisting of surface mount device (SMD) filters on a custom made PCB is then mounted over the CLCC, to provide connections to the electronic control hardware.

the trap chip through optical quality windows. All of the trap electrodes are connected to the outside of the UHV chamber through the CLCC, which eliminates the need for complicated and tedious wiring inside the chamber, and simultaneously provides UHV feedthroughs for several tens of conductors. A circuit board containing filters for all DC electrodes can be mounted directly around the CLCC. This minimises the electrical path from the electrodes to the filters, yet does so outside the vacuum chamber.

The one drawback is that the chamber cannot be baked out to greater than 120°C due to the melting point of the indium seals (see figure 7.9). However, it will be possible using pre-baking techniques to reach pressures in the 10^{-11} mbar range with final bake-out at this limited temperature.

7.5 Further work

There remain several outstanding actions required for the realisation of the proposed trap structure. A significant difficulty is that of removing the SU8 photoresist layer. It is thought that a different masking substance, such as AZ9260, should be used. This will be trialed on an intermediate design, and ultimately on the full traps. While each individual step of the fabrication process has been demonstrated, a single wafer has yet to be taken through the full process from beginning to end, to produce the trap design originally specified.

Once the traps have been fabricated, mounted and tested, work must be carried out to load, trap and cool a string of a few ions. There are various aspects of trap performance which it will be instructive to characterise. Most notable among these are the trap efficiency and the heating rate. Having characterised the trap, a string of cold ions can be used to demonstrate shuttling of ions and eventually to implement QIP protocols and demonstrate quantum-enhanced metrology capabilities. To realise this ultimate aim, the existing experimental apparatus must be upgraded in several respects. The agility of the frequency- and phase-switching of the probe laser system must be improved, so that arbitrary pulse sequences can be applied. The imaging optics must also be improved to allow the spatial resolution of a string of ions. This is planned to involve a series of high numerical aperture lenses (NA of 0.5–0.7) imaging the fluorescence from the ion onto a CCD camera.

In addition to the work on the existing fabrication run of traps, NPL is part of a European Union collaboration involving six institutions (IST 2006-517675-MICROTRAP). This collaboration will require further advances in the silica-on-silicon fabrication methods developed to date, and extend them to traps with cross junctions (figure 7.2), as well as linear traps similar to those described in this chapter.

Ultimately, it may be possible for such devices to be integrated with other technologies such as optical fibres, on-chip waveguides and MEMS optical components. Furthermore, as with photonics components, construction of hybrid devices which integrate electronics components onto the silica-on-silicon trap chip could be feasible.

7.6 Summary

This chapter has described the progress made towards the fabrication of novel, monolithic, linear, RF ion traps, based on silica-on-silicon fabrication techniques. A fabrication process is being developed in order to achieve the structure modelled in chapter 6. Each individual step of the originally proposed process has been demonstrated separately, although there have been difficulties associated with performing the entire sequence. Notable among these problems are those associated with the SU8 photoresist and its removal, and alternative photoresists have been proposed to circumvent such issues. An intermediate design has also been proposed which should provide a reasonable trapping potential, and allow initial tests of trap performance while the full fabrication process is being refined. As the development progresses, it is expected that certain aspects of the design may need to be modified.

CHAPTER 8

Conclusion

8.1 Summary

This thesis has described photoionisation loading of a single $^{88}\mathrm{Sr}^{+}$ ion into an RF endcap trap, resolved-sideband cooling of this ion to the zero point of its motion, and a measurement of the ion's subsequent heating rate. It has additionally described the design and modelling of a novel, monolithic, silicon-based linear ion trap, and the progress that has been made towards fabricating the proposed design. This work has been carried out in the context of developing experimental techniques which will be required for realising trapped-ion quantum computing, and investigating scalable technologies which will provide architectures for quantum computation involving many trapped ions. Ultimately, this project aims to implement quantum operations in a segmented trap, and perform quantum-enhanced metrology on strings of entangled ions.

During the course of this work, a number of improvements have been made to the pre-existing experimental system. Most notable among these has been the implementation of a photoionisation method. The external-cavity diode laser designed for this implementation was then adapted to upgrade the previous 844 nm ECDL (for the Doppler-cooling laser system) and the 1033 nm ECDL (quencher/clearout laser). These lasers have proved to offer more reliable day-to-day operation than the earlier laser designs. A monolithic, temperature-controlled 844 nm doubling cavity was also made to replace an earlier design. The new cavity is expected to significantly improve the ease of running the cooling laser.

The two-step resonant method for clean, efficient, and controlled photoionisation loading of strontium was implemented using diode-laser-based systems. This replaced the previously used electron-bombardment loading method, with the aim of reducing the flux of Sr and electrons towards the trap, thereby improving both trapping stability over time, and reducing ion-heating rates. The two-step photoionisation process proceeds via the $5s^2\ {}^1S_0$—$5s5p\ {}^1P_1$ dipole transition ($\lambda = 461$ nm), and is immediately followed by direct excitation to the $(4d^2{+}5p^2)\ {}^1D_2$ autoionising state ($\lambda = 405$ nm). Once an ion is created, near resonant and far-detuned Doppler-cooling beams ($\lambda = 422$ nm) facilitate rapid cooling to the Doppler limit. Using this photoionisation method, the atomic flux required to load the trap is $\sim10^4$ times less than when using electron bombardment ionisation. The photoionisation loading method also substantially reduces the variation of charge on insulating surfaces during the experiment: the day-to-day fluctuations of micromotion-compensation voltages are reduced by a factor of $\sim$10. Additionally, using a clean trap which has only been loaded by photoionisation allowed a low ion-heating rate to be obtained.

A single trapped $^{88}\mathrm{Sr}^{+}$ ion has been cooled to the ground state of its axial motion using resolved-sideband cooling on an optical quadrupole transition. Ground-state cooling is a prerequisite of many trapped-ion QIP procedures. Realising a low heating rate is also essential for preserving motional coherence during quantum gate operations. Cooling to the ground state was achieved by first Doppler cooling the ion to the Lamb-Dicke regime, and then implementing sideband cooling on the lower axial motional sideband of the 5s $^{2}\mathrm{S}_{1/2}$—4d $^{2}\mathrm{D}_{5/2}$ transition. A laser at 1033 nm, resonant with the 4d $^{2}\mathrm{D}_{5/2}$—5p $^{2}\mathrm{P}_{3/2}$ transition, shortened the $^{2}\mathrm{D}_{5/2}$ state lifetime in order to allow an appreciable cooling rate. The ion was measured to have a mean axial phonon number of $\bar{n}_{\mathrm{z}} = 0.03(1)$, 0.9 ms after cooling ended. It is estimated that this corresponds to a value of $\bar{n}_{\mathrm{z}} = 0.014(8)$ immediately after cooling, corresponding to a ground-state occupation probability of 98.6(8)%. The heating rate of the trapped ion has been measured to be $\dot{\bar{n}} = 0.054(4)$ quanta/ms. Assuming that the source of this heating is fluctuating electric-field noise, this yields an inferred spectral density of the electric-field noise comparable to the values reported by other groups using different traps and atomic species. This low heating rate was only achieved after constructing a trap that was exclusively loaded by photoionisation, and hence was exposed to minimal atomic flux.

A novel, monolithic linear RF ion trap design has been proposed. The three-dimensional trap structure, to be microfabricated on a chip using silica-on-silicon processing techniques, is of significant interest for implementations of QIP using trapped ions. The design provides a number of adjacent trapping zones, between which ions can be shuttled, and may form the basis of a scalable trapped-ion quantum-computing architecture. The trap electrodes are formed by gold-coated SiO_2, and are spaced by highly-doped silicon. The electrostatics of such a structure were modelled using FEMLAB, MATLAB and SIMION. Simple lumped-element models were also developed to investigate the effect of RF heating on the substrate. Under practical operating conditions, the trap design is calculated to provide deep potentials with motional frequencies of several MHz, exhibit a deep potential well, a high trap efficiency, and a low RF loss. These features contrast with some of the other microfabricated traps reported in the literature. These differences will contribute to an increased understanding of ion trap materials and structures for QIP applications.

Progress has been made towards fabrication of the ion-trap design described, working with the Centre for Integrated Photonics. A fabrication process to achieve the desired structure has been proposed. This process consists of lithographic patterning, anisotropic etching of SiO_2, isotropic etching of silicon, and metallic evaporation and electroplating. Each individual step of this process has been demonstrated separately, although there have been difficulties associated with performing the entire sequence; notably with regards achieving an acceptable under-etch, and removing the SU8 photoresist. An intermediate design has been proposed which should provide a reasonable trapping potential, and allow initial tests of trap performance while the full fabrication process is being refined.

8.2 Further work

There remain several outstanding actions required for the realisation of the proposed trap structure. While each individual step of the fabrication process has been demonstrated, a single wafer has yet to be taken through the full process from beginning to end, to produce the trap design originally specified. Further process development is required to achieve this. In the first instance it is expected that an intermediate trap design will be used to perform initial testing of mounting and loading methods, though such traps are expected to have low motional frequencies and high heating rates. In preparation for the full trap design, there are several further upgrades which must be made to the existing apparatus.

The coherent evolution of the S—D transition can be manipulated by applying various probe-laser pulse sequences [41]. Using the present system, only simple pulse sequences are possible. The agility of the frequency and phase switching of the probe-laser system must be improved, so that arbitrary pulse sequences can be applied. Currently the imaging optics can detect only the number of fluorescence counts. The imaging system must be improved to allow the spatial resolution of a string of ions. It may also be necessary to improve the 461 nm laser linewidth and stability to allow selective loading of isotopically pure strings of $^{88}\text{Sr}^+$ ions.

Once the full trap designs have been fabricated, it is intended to use these to demonstrate ground-state cooling of a one-dimensional ion string, shuttling of ions, and ultimately quantum-enhanced spectroscopy, where the measurement noise is reduced by entangling of the ions' electronic states. In addition to the work on the existing fabrication run of traps, NPL is part of a European Union collaboration, which will provide further advances in the silica-on-silicon fabrication methods developed to date, and extend them to traps with cross junctions.

In future, silica-on-silicon technology should provide a platform which is scalable to more complex devices, and which could be integrated with other technologies such as optical fibres, on-chip waveguides and MEMS optical components. Furthermore, as with photonics components, construction of hybrid devices which integrate electronics components onto the silica-on-silicon trap chip are feasible. Planar silica-on-silicon technology therefore has the potential to form the basis for large-scale ion trap quantum processors.

8.3 Journal publications

The work described in this thesis has given rise to a number of journal publications. Namely:

> *Controlled photoionization loading of* $^{88}Sr^{+}$ *for precision ion-trap experiments*, M. Brownnutt, V. Letchumanan, G. Wilpers, R.C. Thompson, P. Gill, A.G. Sinclair, Appl. Phys. B 87 (2007) 411–415.
>
> *Zero-point cooling and heating-rate measurements of a single* $^{88}Sr^{+}$ *ion*, V. Letchumanan, G. Wilpers, M. Brownnutt, P. Gill, A.G. Sinclair, Phys. Rev. A 75 (2007) 063425–063428.
>
> *Monolithic microfabricated ion trap chip design for scaleable quantum processors* M. Brownnutt, G. Wilpers, P. Gill, R.C. Thompson, A.G. Sinclair, New J. Phys. 8 (2006) 232–249.

APPENDIX A

Proposed fabrication process

Chapter 7 describes the progress made towards the fabrication of a monolithic, linear RF ion-trap chip. Section 7.3 outlines the planned fabrication method which was originally envisioned, and the steps for this method are sketched in figure 7.1. This appendix illustrates the steps in more detail. Each step is shown in figure A.1, and explained in the text.

1) The process begins with commercially bought, double-sided-polished n-doped silicon wafers. For the first development run, three thicknesses were used: 500 μm, 250 μm, and 150 μm.

2) The wafers are thermally oxidised for 24 days, resulting in a 15 μm thick layer of SiO_2 on both surfaces of the silicon wafer. The growth of the SiO_2 slightly reduces the thickness of the silicon, so that the final thickness of silicon in the oxidised wafers is around 15 m less than that of the unoxidised wafers. This effect is of little importance for the wafer thicknesses being used here.

3) A mask is applied for "windows" to be etched through the SiO_2 to the

silicon. Figure A.1.3 shows one corner of the trap chip. The mask is similar at the other three corners.

4) An inductively coupled plasma (ICP) reactive ion etch (RIE) is used to etch through the SiO_2 to produce windows at the corners of each chip to the silicon. These allow metal pads on the silicon for grounding purposes. It should be noted that these pads must be electrically isolated from the rest of the gold during the gold electroplating process (step 22 below), as the silicon is conductive, and so can also become plated.

5) A mask is applied for the electrode pattern. Figure A.1.5 shows the central portion of the chip, where the trapping region will be.

6) 50 nm of titanium is evaporated onto the SiO_2 as a base layer to ensure the gold adheres to the chip surface. 500 nm of gold is then evaporated into this base layer, resulting in the electrode pattern.

7) A 150 nm thick nickel mask is laid down on top of the gold to protect it during step 19.

8) Photolithographic mask layer is removed, to leave the electrode structure, with a nickel mask.

9) An SU8 mask is applied to protect the electrodes during the SiO_2 etch. The mask covers both the metal electrodes, and the SiO_2 between the electrodes on the RF-side of the trap, leaving exposed SiO_2 in the region where the volume of free space is required for the trap, and be-

tween the DC fingers. SU8 is a standard photoresist used in photonics manufacturing.

10) ICP RIE etch of SiO_2 to expose the silicon where the volume of free space is required for the trap, and to create individual segmented DC electrodes.

11) Remove the SU8 mask.

12) Apply a fresh SU8 mask, leaving the silicon exposed where the free space is required for the trap.

13) Isotropic SF_6 RIE etch of silicon to create the clear aperture through the structure and the free-space undercut between the two parallel SiO_2 layers.

14) Shadow evaporation of titanium and then gold to coat the edges and surface of the SiO_2 in the undercut. Titanium (and subsequently gold) are evaporated from the direction indicated by the arrow in figure A.1.14. This creates a continuous surface of gold from the outside of the electrodes to the underside. The back of the undercut, where it is required that there is electrical connection between the gold and the conducting, grounded silicon, is masked from the evaporation source as it is in the shadow of the electrode above.

15) Shadow evaporation is repeated from four diffent directions, to coat the inside surfaces of all four electrodes. It may be noted that the process also coats the SU8 with a layer of metal; indeed the geometry of the

situation means that the metal layer coating the SU8 is twice as thick as the metal layer in the undercut.

16) Shadow evaporate a nickel layer to protect the gold during step 19. As with shadow evaporation of the titanium and gold, this requires that the process is carried out from four different directions.

17) Removal of SU8. Figure A.1.17 shows a cross section through the DC electrode fingers, taken along the length of the trap, in the yz plane (*c.f.* figure 6.3). The position of this cross section is shown by the dotted line in figure A.1.16.

18) Removal of the SU8 leaves the titanium and gold between the DC fingers exposed.

19) A wet etch removes the metal between the DC fingers, while the metal on the electrodes themselves is masked by the nickel.

20) The nickel is removed to ensure there are gaps between the DC fingers, and that the chip is free of (magnetic) nickel.

21) The electrodes are plated with 5 μm, giving a surface roughness of < 10 nm RMS.

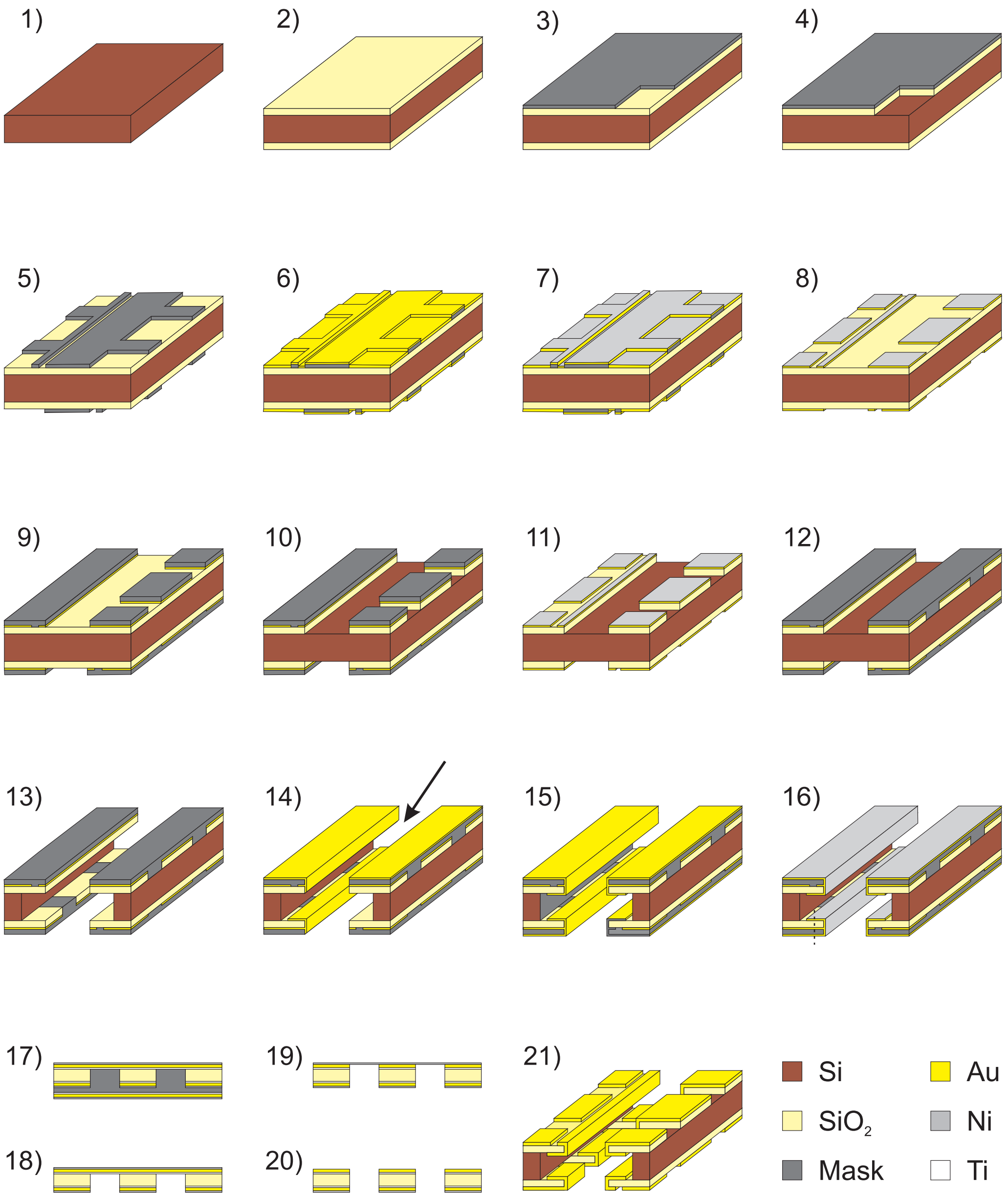

Figure A.1: Details of planned trap fabrication method. See text for explanation.

References

[1] R. P. Feynman, Simulating physics with computers, Int. J. Th. Phys. 21 (1982) 467–488.

[2] P. W. Shor, Algorithms for quantum computation: discrete logarithms and factoring, in: IEEE Symposium on the Foundation of Computer Science, 1994, pp. 124–134.

[3] R. L. Rivest, A. Shamir, L. Adleman, A method for obtaining digital signatures and public-key cryptosystems, Communications of the ACM 21 (1978) 120–126.

[4] D. Deutsch, Quantum theory, the Church-Turing principle and the universal quantum computer, Proc. R. Soc. Lond. A 400 (1985) 97–117.

[5] D. Deutsch, R. Jozsa, Rapid solution of problems by quantum computation, Proc. Mat. Phys. Sci. 439 (1992) 553–558.

[6] L. K. Grover, Quantum mechanics helps in searching for a needle in a haystack, Phys. Rev. Lett. 79 (1997) 325–328.

[7] A. R. Calderbank, P. W. Shor, Good quantum error-correcting codes exist, Phys. Rev. A 54 (1996) 1098–1105.

[8] A. Steane, Multiple particle interference and quantum error correction, Proc. Mat. Phys. Eng. Sci. 452 (1996) 2551–2577.

[9] C. H. Bennett, G. Brassard, C. Crépeau, R. Jozsa, A. Peres, W. K. Wootters, Teleporting an unknown quantum state via dual classical and Einstein-Podolsky-Rosen channels, Phys. Rev. Lett. 70 (1993) 1895–1899.

[10] C. H. Bennett, G. Brassard, Public key distribution and coin tossing, in: Proc. IEEE Inter. Conf. on Computers, Systems and Signal Processing, Bangalore, 1984, pp. 175–179.

[11] D. J. Wineland, D. Leibfried, M. D. Barrett, A. Ben-Kish, J. C. Bergquist, R. B. Blakestad, J. J. Bollinger, J. Britton, J. Chiaverini, B. DeMarco, D. Hume, W. M. Itano, M. Jensen, J. D. Jost, E. Knill, J. Koeleemeij, C. Langer, W. Oskay, R. Ozeri, R. Reichle, T. Rosenband, T. Schaetz, P. O. Schmidt, S. Seidelin, Quantum control, quantum information processing, and quantum-limited metrology with trapped ions, in: Proceedings of XVII International Conference on Laser Spectroscopy (Aviemore, Scotland), World Scientific, Singapore, 2005, pp. 393–402, preprint: quant-ph/0508025.

[12] L. M. K. Vandersypen, M. Steffen, G. Breyta, C. S. Yannoni, M. H. Sherwood, I. L. Chuang, Experimental realisation of Shor's quan-

tum factoring algorithm using nuclear magnetic resonance, Nature 414 (2001) 883–887.

[13] J. A. Jones, NMR quantum computation: a critical evaluation, Fortschr. Phys. 48 (2000) 909–924.

[14] Special edition: Experimental proposals for quantum computation, Fortschr. Phys. 48 (2000) 769–1138, editors: S. Braunstein and Hoi-Kwong Lo.

[15] D. J. Wineland, C. Monroe, W. M. Itano, D. Leibfried, B. E. King, D. M. Meekhof, Experimental issues in coherent quantum-state manipulation of trapped atomic ions, J. Res. Natl. Inst. Stand. Technol. 103 (1998) 259–328.

[16] M. Šašura, V. Bužek, Cold trapped ions as quantum information processors, J. Mod. Opt. 49 (2002) 1593–1647.

[17] D. Leibfreid, R. Blatt, C. Monroe, D. Wineland, Quantum dynamics of single trapped ions, Rev. Mod. Phys. 75 (2003) 281–324.

[18] A. Ekert, R. Jozsa, Quantum computation and Shor's factoring algorithm, Rev. Mod. Phys. 68 (1996) 733–753.

[19] J. Chiaverini, J. Britton, D. Leibfried, E. Knill, M. D. Barrett, R. B. Blakestad, W. M. Itano, J. D. Jost, C. Langer, R. Ozeri, T. Schaetz, D. J. Wineland, Implementation of the semiclassical quantum Fourier transform in a scalable system, Science 308 (2005) 997–1000.

[20] S. Gulde, M. Riebe, G. P. T. Lancaster, C. Becher, J. Eschner, H. Häffner, F. Schmidt-Kaler, I. L. Chuang, R. Blatt, Implementation of the Deutsch-Jozsa algorithm on an ion-trap quantum computer, Nature 421 (2003) 48–50.

[21] K.-A. Brickman, P. C. Haljan, P. J. Lee, M. Acton, L. Deslauriers, C. Monroe, Implementation of Grover's quantum search algorithm in a scalable system, Phys. Rev. A 72 (2005) 050306–050309(R).

[22] J. Chiaverini, D. Leibfried, T. Schaetz, M. D. Barrett, R. B. Blakestad, J. Britton, W. M. Itano, J. D. Jost, E. Knill, C. Langer, R. Ozeri, D. J. Wineland, Realization of quantum error correction, Nature 432 (2004) 602–605.

[23] M. Riebe, H. Häffner, C. F. Roos, W. Hänsel, J. Benhelm, G. P. T. Lancaster, T. W. Körber, C. Becher, F. Schmidt-Kaler, D. F. V. James, R. Blatt, Deterministic quantum teleportation with atoms, Nature 429 (2004) 734–737.

[24] M. D. Barrett, J. Chiaverini, T. Schaetz, J. Britton, W. M. Itano, J. D. Jost, E. Knill, C. Langer, D. Leibfried, R. Ozeri, D. J. Wineland, Deterministic quantum teleportation of atomic qubits, Nature 429 (2004) 737–739.

[25] D. Leibfried, B. DeMarco, V. Meyer, M. Rowe, A. Ben-Kish, J. Britton, W. M. Itano, B. Jelenković, C. Langer, T. Rosenband, D. J. Wineland, Trapped-ion quantum simulator: experimental application to nonlinear interferometers, Phys. Rev. Lett. 89 (2002) 247901–247904.

[26] V. Meyer, M. A. Rowe, D. Kielpinski, C. A. Sackett, W. M. Itano, C. Monroe, D. J. Wineland, Experimental demonstration of entanglement-enhanced rotation angle estimation using trapped ions, Phys. Rev. Lett. 86 (2001) 5870–5873.

[27] D. Leibfried, M. D. Barrett, T. Schaetz, J. Britton, J. Chiaverini, W. M. Itano, J. D. Jost, C. Langer, D. J. Wineland, Toward Heisenberg-limited spectroscopy with multiparticle entangled states, Science 304 (2004) 1476–1478.

[28] D. Leibfried, E. Knill, S. Seidelin, J. Britton, R. B. Blakestad, J. Chiaverini, D. B. Hume, W. M. Itano, J. D. Jost, C. Langer, R. Ozeri, R. Reichle, D. J. Wineland, Creation of a six-atom 'Schrödinger cat' state, Nature 438 (2005) 639–642.

[29] H. Häffner, W. Hänsel, C. F. Roos, J. Benhelm, D. Chek-al-kar, M. Chwalla, T. Körber, U. D. Rapol, M. Riebe, P. O. Schmidt, C. Becher, O. Gühne, W. Dür, R. Blatt, Scalable multiparticle entanglement of trapped ions, Nature 438 (2005) 643–646.

[30] D. P. DiVincenzo, The physical implementation of quantum computation, Fortschr. Phys. 48 (2000) 771–783.

[31] V. Letchumanan, M. A. Wilson, P. Gill, A. G. Sinclair, Lifetime measurement of the metastable 4d $^2D_{5/2}$ state in $^{88}Sr^+$ using a single trapped ion, Phys. Rev. A 72 (2005) 012509–012516.

[32] H. C. Nägerl, C. Roos, D. Leibfried, H. Rohde, G. Thalhammer, J. Eschner, F. Schmidt-Kaler, R. Blatt, Investigating a qubit candidate:

spectroscopy on the $S_{1/2}$ to $D_{5/2}$ transition of a trapped calcium ion in a linear Paul trap, Phys. Rev. A 61 (2000) 023405–023413.

[33] F. Schmidt-Kaler, S. Gulde, M. Riebe, T. Deuschle, A. Kreuter, G. Lancaster, C. Becher, J. Eschner, H. Häffner, R. Blatt, The coherence of qubits based on single Ca^+ ions, J. Phys. B 36 (2003) 623–636.

[34] D. Kielpinski, C. Monroe, D. J. Wineland, Architecture for a large-scale ion-trap quantum computer, Nature 417 (2002) 709–711.

[35] J. I. Cirac, P. Zoller, A scalable quantum computer with ions in an array of microtraps, Nature 404 (2000) 579–581.

[36] A. Steane, D. M. Lucas, Quantum computing with trapped ions, atoms and light, Fortschr. Phys. 48 (2000) 839–858.

[37] D. L. Moehring, M. J. Madsen, K. C. Younge, R. N. Kohn, Jr., P. Maunz, L.-M. Duan, C. Monroe, B. B. Blinov, Quantum networking with photons and trapped atoms, J. Opt. Soc. Am. B 24 (2007) 300–315.

[38] B. B. Blinov, D. L. Moehring, L.-M. Duan, C. Monroe, Observation of entanglement between a single trapped atom and a single photon, Nature 428 (2004) 153–157.

[39] L. Tian, R. Blatt, P. Zoller, Scalable ion trap quantum computing without moving ions, Eur. Phys. J. D 32 (2005) 201–208.

[40] D. Leibfried, B. DeMarco, V. Meyer, D. Lucas, M. Barrett, J. Britton, W. M. Itano, B. Jelenković, C. Langer, T. Rosenband, D. J. Wineland,

Experimental demonstration of a robust, high-fidelity geometric two ion-qubit phase gate, Nature 422 (2003) 412–415.

[41] F. Schmidt-Kaler, H. Häffner, S. Gulde, M. Riebe, G. P. T. Lancaster, T. Deuschle, C. Becher, W. Hänsel, J. Eschner, C. F. Roos, R. Blatt, How to realize a universal quantum gate with trapped ions, Appl. Phys. B 77 (2003) 789–796.

[42] D. P. DiVincenzo, Two-bit gates are universal for quantum computation, Phys. Rev. A 51 (1995) 1015–1022.

[43] A. Barenco, C. H. Bennett, R. Cleve, D. P. DiVincenzo, N. Margolus, P. Shor, T. Sleator, J. A. Smolin, H. Weinfurter, Elementary gates for quantum computation, Phys. Rev. A 52 (1995) 3457–3467.

[44] J. I. Cirac, P. Zoller, Quantum computations with cold trapped ions, Phys. Rev. Lett. 74 (1995) 4091–4094.

[45] F. Schmidt-Kaler, H. Häffner, M. Riebe, S. Gulde, G. P. T. Lancaster, T. Deuschle, C. Becher, C. F. Roos, J. Eschner, R. Blatt, Realization of the Cirac-Zoller controlled-NOT quantum gate, Nature 422 (2003) 408–411.

[46] H. Dehmelt, Proposed $10^{14}\delta\nu < \nu$ laser fluorescence spectroscopy on Tl^+ mono-ion oscillator II (spontaneous quantum jumps), Bull. Am. Phys. Soc. 20 (1975) 60.

[47] W. Nagourney, N. Sandberg, H. Dehmelt, Shelved optical electron am-

plifier: observation of quantum jumps, Phys. Rev. Lett. 56 (1986) 2797–2799.

[48] M. Acton, K.-A. Brickman, P. C. Haljan, P. J. Lee, L. Deslauriers, C. Monroe, Near-perfect simultaneous measurement of a qubit register, Quant. Inf. Comp. 6 (2006) 465–482.

[49] H. C. Nägerl, D. Leibfried, H. Rohde, G. Thalhammer, J. Eschner, F. Schmidt-Kaler, R. Blatt, Laser addressing of individual ions in a linear ion trap, Phys. Rev. A 60 (1999) 145–148.

[50] M. A. Rowe, A. Ben-Kish, B. DeMarco, D. Leibfried, V. Meyer, J. Beall, J. Britton, J. Hughes, W. M. Itano, B. Jelenković, C. Langer, T. Rosenband, D. J. Wineland, Transport of quantum states and separation of ions in a dual RF ion trap, Quant. Inf. Comp. 2 (2002) 257–271.

[51] C. E. Moore, Atomic energy levels, Vol. 2, U.S. Government Printing Office, Washington, 1952.

[52] T. P. Dinneen, K. R. Vogel, E. Arimondo, J. L. Hall, A. Gallagher, Cold collisions of Sr*-Sr in a magneto-optical trap, Phys. Rev. A 59 (1999) 1216–1222.

[53] M. A. Baig, M. Yaseen, R. Ali, A. Nadeem, S. A. Bhatti, Near-threshold photoionization spectra of strontium, Chem. Phys. Lett. 296 (1998) 403–407.

[54] A. Gallagher, Oscillator strengths of Ca II, Sr II, and Ba II, Phys. Rev. 157 (1967) 24–30.

[55] H. S. Margolis, G. Huang, G. P. Barwood, S. N. Lea, H. A. Klein, W. R. C. Rowley, P. Gill, R. S. Windeler, Absolute frequency measurement of the 674-nm ^{88}Sr^{+} clock transition using a femtosecond optical frequency comb, Phys. Rev. A 67 (2003) 032501–032505.

[56] Sami-ul-Haq, S. Mahmood, N. Amin, Y. Jamil, R. Ali, M. A. Baig, Measurements of photoionization cross sections from the 5s5p ^{1}P$_{1}$ and 5s6s ^{1}S$_{0}$ excited states of strontium, J. Phys. B 39 (2006) 1587–1596.

[57] I. Marzoli, J. I. Cirac, R. Blatt, P. Zoller, Laser cooling of trapped three-level ions: designing two-level systems for sideband cooling, Phys. Rev. A 49 (1994) 2771–2779.

[58] V. Letchumanan, P. Gill, E. Riis, A. G. Sinclair, Optical Ramsey spectroscopy of a single trapped ^{88}Sr^{+} ion, Phys. Rev. A 70 (2004) 033419–033427.

[59] H. Dehmelt, Radiofrequency spectroscopy of stored ions I: storage, Adv. At. Mol. Phys. 3 (1967) 53–72.

[60] W. Paul, Electromagnetic traps for charged and neutral particles, Rev. Mod. Phys. 62 (1990) 531–540.

[61] P. J. Blythe, S. A. Webster, K. Hosaka, P. Gill, Systematic frequency shifts of the 467 nm electric octupole transition in ^{171}Yb^{+}, J. Phys. B 36 (2003) 981–989.

[62] N. Yu, W. Nagourney, H. Dehmelt, Demonstration of new Paul-Straubel trap for trapping single ions, J. Appl. Phys 69 (1991) 3779–3781.

[63] R. G. Brewer, R. G. DeVoe, R. Kallenbach, Planar ion microtraps, Phys. Rev. A 46 (1992) 6781–6784(R).

[64] C. A. Schrama, E. Peik, W. W. Smith, H. Walther, Novel miniature ion traps, Opt. Commun. 101 (1993) 32–36.

[65] S. R. Jefferts, C. Monroe, E. W. Bell, D. J. Wineland, A coaxial-resonator-driven rf (Paul) trap for strong confinement, Phys. Rev. A 51 (1995) 3112–3116.

[66] L. Deslauriers, S. Olmschenk, D. Stick, W. K. Hensinger, J. Sterk, C. Monroe, Scaling and suppression of anomalous heating in ion traps, Phys. Rev. Lett. 97 (2006) 103007–103010.

[67] A. Steane, The ion trap quantum information processor, Appl. Phys. B 64 (1997) 623–642.

[68] H. C. Nägerl, W. Bechter, J. Eschner, F. Schmidt-Kaler, R. Blatt, Ion strings for quantum gates, Appl. Phys. B 66 (1998) 603–608.

[69] D. J. Berkeland, Linear Paul trap for strontium ions, Rev. Sci. Inst. 73 (2002) 2856–2860.

[70] M. J. Madsen, W. K. Hensinger, D. Stick, J. A. Rabchuck, C. Monroe, Planar ion trap geometry for microfabrication, Appl. Phys. B 78 (2004) 639–651.

[71] D. Stick, W. K. Hensinger, S. Olmschenk, M. J. Madsen, K. Schwab, C. Monroe, Ion trap in a semiconductor chip, Nature Physics 2 (2006) 36–39.

[72] L. Deslauriers, P. C. Haljan, P. J. Lee, K.-A. Brickman, B. B. Blinov, M. J. Madsen, C. Monroe, Zero-point cooling and low heating of trapped $^{111}\mathrm{Cd}^{+}$ ions, Phys. Rev. A 70 (2004) 043408–043412.

[73] W. K. Hensinger, S. Olmschenk, D. Stick, D. Hucul, M. Yeo, M. Acton, L. Deslauriers, C. Monroe, J. Rabchuk, T-junction ion trap array for two-dimensional ion shuttling, storage, and manipulation, Appl. Phys. Lett. 88 (2006) 034101–034103.

[74] J. P. Home, A. M. Steane, Electrode configurations for fast separation of trapped ions, Quant. Inf. Comp. 6 (2006) 289–325.

[75] D. Hucul, M. Yeo, S. Olmschenk, C. Monroe, W. K. Hensinger, J. Rabchuk, On the transport of atomic ions in linear and multidimensional ion trap arrays, Preprint quant-ph/0702175 v2 (2007).

[76] J. Chiaverini, R. B. Blakestad, J. Britton, J. D. Jost, C. Langer, D. Leibfried, R. Ozeri, D. J. Wineland, Surface-electrode architecture for ion-trap quantum information processing, Quant. Inf. Comp. 5 (2005) 419–439.

[77] S. Seidelin, J. Chiaverini, R. Reichle, J. J. Bollinger, D. Leibfried, J. Britton, J. H. Wesenberg, R. B. Blakestad, R. J. Epstein, D. B. Hume, W. M. Itano, J. D. Jost, C. Langer, R. Ozeri, N. Shiga, D. J.

Wineland, Microfabricated surface-electrode ion trap for scalable quantum information processing, Phys. Rev. Lett. 96 (2006) 253003–253006.

[78] A. Steane, C. F. Roos, D. Stevens, A. Mundt, D. Leibfried, F. Schmidt-Kaler, R. Blatt, Speed of ion-trap quantum-information processors, Phys. Rev. A. 62 (2000) 042305–042313.

[79] M. Drewsen, A. Brøner, Harmonic linear Paul trap: stability diagram and effective potentials, Phys. Rev. A 62 (2000) 045401–045404.

[80] R. Alheit, C. Hennig, R. Morgenstern, F. Vedel, G. Werth, Observation of instabilities in a Paul trap with higher-order anharmonicities, Appl. Phys. B. 61 (1995) 277–283.

[81] D. J. Berkeland, J. D. Miller, J. C. Bergquist, W. M. Itano, D. J. Wineland, Minimization of ion micromotion in a Paul trap, J. Appl. Phys. 83 (1998) 5025–5033.

[82] A. G. Sinclair, M. A. Wilson, P. Gill, Improved three-dimensional control of a single strontium ion in an endcap trap, Opt. Commun. 190 (2001) 193–203.

[83] J. P. Schiffer, Phase transitions in anisotropically confined ionic crystals, Phys. Rev. Lett. 70 (1993) 818–821.

[84] R. G. DeVoe, J. Hoffnagle, R. G. Brewer, Role of laser damping in trapped ion crystals, Phys. Rev. A 39 (1989) 4362–4365.

[85] D. J. Wineland, R. E. Drullinger, F. L. Walls, Radiation-pressure cooling of bound resonant absorbers, Phys. Rev. Lett. 40 (1978) 1639–1642.

[86] D. J. Wineland, W. M. Itano, Laser cooling of atoms, Phys. Rev. A 20 (1979) 1521–1540.

[87] W. M. Itano, D. J. Wineland, Laser cooling of ions stored in harmonic and Penning traps, Phys. Rev. A 25 (1982) 35–54.

[88] R. Blatt, G. Lafyatis, W. D. Phillips, S. Stenholm, D. J. Wineland, Cooling in traps, Physica Scripta T22 (1988) 216–223.

[89] D. J. Wineland, H. Dehmelt, Proposed $10^{14}\delta\nu < \nu$ laser fluorescence spectroscopy on Tl^+ mono-ion oscillator III (side band cooling), Bull. Am. Phys. Soc. 20 (1975) 637–637.

[90] D. J. Wineland, W. M. Itano, J. C. Bergquist, R. G. Hulet, Laser-cooling limits and single-ion spectroscopy, Phys. Rev. A 36 (1987) 2220–2232.

[91] D. J. Heinzen, D. J. Wineland, Quantum-limited cooling and detection of radio-frequency oscillations by laser-cooled ions, Phys. Rev. A 42 (1990) 2977–2994.

[92] R. H. Dicke, The effect of collisions upon the Doppler width of spectral lines, Phys. Rev. 89 (1953) 472–473.

[93] M. Brownnutt, V. Letchumanan, G. Wilpers, R. C. Thompson, P. Gill, A. G. Sinclair, Controlled photoionization loading of $^{88}\mathrm{Sr}^+$ for precision ion-trap experiments, Appl. Phys. B 87 (2007) 411–415.

[94] V. Letchumanan, G. Wilpers, M. Brownnutt, P. Gill, A. G. Sinclair,

Zero-point cooling and heating-rate measurements of a single $^{88}\mathrm{Sr}^{+}$ ion, Phys. Rev. A 75 (2007) 063425–063428.

[95] M. Brownnutt, G. Wilpers, P. Gill, R. C. Thompson, A. G. Sinclair, Monolithic microfabricated ion trap chip design for scaleable quantum processors, New J. Phys. 8 (2006) 232–249.

[96] J. B. Camp, T. W. Darling, R. E. Brown, Macroscopic variations of surface potentials of conductors, J. Appl. Phys. 69 (1991) 7126–7129.

[97] R. G. DeVoe, C. Kurtsiefer, Experimental study of anomalous heating and trap instabilities in a microscopic $^{137}\mathrm{Ba}$ ion trap, Phys. Rev. A 65 (2002) 063407–063414.

[98] W. W. Macalpine, R. O. Schildknecht, Coaxial resonators with helical inner conductor, Proc. IRE (1959) 2099–2105.

[99] P. McNichol, H. J. Metcalf, Synchronous cavity mode and feedback wavelength scanning in dye laser oscillators with gratings, Appl. Opt. 24 (1985) 2757–2761.

[100] L. Nilse, H. J. Davies, C. S. Adams, Synchronous tuning of extended cavity diode lasers: the case for the optimum pivot point, Appl. Opt. 38 (1999) 548–553.

[101] G. Boyd, D. Kleinman, Parametric interaction of focussed gaussian light beams, J. Appl. Phys. 39 (1968) 3597–3639.

[102] E. S. Polzik, H. J. Kimble, Frequency doubling with $\mathrm{KNbO_3}$ in an external cavity, Opt. Lett. 16 (1991) 1400–1402.

[103] I. Biaggio, P. Kerkoc, L.-S. Wu, P. Günther, B. Zysset, Refractive indices of orthorhombic $KNbO_3$ II. Phase-matching configurations for non-linear-optical interactions, J. Opt. Soc. Am. B 9 (1992) 507–517.

[104] B. Zysset, I. Biaggio, P. Günter, Refractive indices of orthorhombic $KNbO_3$ I. Dispersion and temperature dependence, J. Opt. Soc. Am. B 9 (1992) 380–386.

[105] T. W. Hänsch, B. Couillaud, Laser frequency stabilisation by polarization spectroscopy of a reflecting reference cavity, Opt. Commun. 35 (1980) 441–444.

[106] A. A. Madej, L. Marmet, J. E. Bernard, Rb atomic absorption line reference for single Sr^+ laser cooling systems, Appl. Phys. B 67 (1998) 229–234.

[107] R. W. P. Drever, J. L. Hall, F. V. Kowalski, J. Hough, G. M. Ford, A. J. Munley, H. Ward, Laser phase and frequency stabilization using an optical resonator, Appl. Phys. B 31 (1983) 97.

[108] A. A. Madej, J. D. Sankey, Single, trapped Sr^+ atom: laser cooling and quantum jumps by means of the $4d^2D_{5/2}$–$5s^2S_{1/2}$ transition, Opt. Lett. 15 (1990) 634–636.

[109] D. J. Berkeland, M. G. Boshier, Destabilisation of dark states and optical spectroscopy in Zeeman-degenerate atomic systems, Phys. Rev. A 65 (2002) 033413–033425.

[110] Q. A. Turchette, D. Kielpinski, B. E. King, D. Leibfried, D. M.

Meekhof, C. J. Myatt, M. A. Rowe, C. A. Sackett, C. S. Wood, W. M. Itano, C. Monroe, D. J. Wineland, Heating of trapped ions from the quantum ground state, Phys. Rev. A 61 (2000) 063418–063425.

[111] N. Kjærgaard, L. Hornekær, A. M. Thommesen, Z. Videsen, M. Drewsen, Isotope selective loading of an ion trap using resonance-enhanced two-photon ionization, Appl. Phys. B 71 (2000) 207–210.

[112] S. Gulde, D. Rotter, P. Barton, F. Schmidt-Kaler, R. Blatt, W. Hogervorst, Simple and efficient photo-ionization loading of ions for precision ion-trapping experiments, Appl. Phys. B 73 (2001) 861–863.

[113] D. M. Lucas, A. Ramos, J. P. Home, M. J. McDonnell, S. Nakayama, J.-P. Stacey, S. C. Webster, D. N. Stacey, A. M. Steane, Isotope-selective photoionization for calcium ion trapping, Phys. Rev. A 69 (2004) 012711–012723.

[114] L. Deslauriers, M. Acton, B. B. Blinov, K.-A. Brickman, P. C. Haljan, W. K. Hensinger, D. Hucul, S. Katnik, R. N. Kohn, Jr., P. J. Lee, M. J. Madsen, P. Maunz, S. Olmschenk, D. L. Moehring, D. Stick, J. Sterk, M. Yeo, K. C. Younge, C. Monroe, Efficient photoionization loading of trapped ions with ultrafast pulses, Phys. Rev. A 74 (2006) 063421–063431.

[115] K. Vant, J. Chiaverini, W. Lybarger, D. J. Berkeland, Photoionization of strontium for trapped-ion quantum information processing, Preprint quant-ph/0607055 v1 (2006).

[116] F. Diedrich, J. C. Bergquist, W. M. Itano, D. J. Wineland, Laser cooling to the zero-point energy of motion, Phys. Rev. Lett. 62 (1989) 403–406.

[117] C. Roos, T. Zeiger, H. Rohde, H. C. Nägerl, J. Eschner, D. Leibfried, F. Schmidt-Kaler, R. Blatt, Quantum state engineering on an optical transition and decoherence in a Paul trap, Phys. Rev. Lett. 83 (1999) 4713–4716.

[118] K. Mølmer, A. Sørensen, Multiparticle entanglement of hot trapped ions, Phys. Rev. Lett. 82 (1999) 1835–1838.

[119] W. H. Parkinson, E. Reeves, F. S. Tomkins, Neutral calcium, strontium and barium: determination of f values of the principal series by the hook method., J. Phys. B 9 (1976) 157–165.

[120] W. Mende, K. Bartschat, M. Kock, Near-threshold photoionization from the Sr I (5s5p) $^1\mathrm{P}^0_1$ state, J. Phys. B 28 (1995) 2385–2393.

[121] C. J. Dai, S. F. Hu, J. Lu, Multistep excitation of autoionizing states of neutral strontium, J. Quant. Spectrosc. Radiat. Transfer 56 (1996) 255–262.

[122] B. A. Bushaw, B. D. Cannon, Diode laser based resonance ionisation mass spectrometric measurements of strontium-90, Spectrochimica Acta B 52 (1997) 1839–1854.

[123] B. Bushaw, W. Nöterhuser, Resonance ionisation spectroscopy of stable

strontium isotopes and ^{90}Sr via $5s^2\ {}^1S_0 \rightarrow 5s5p\ {}^1P_1 \rightarrow 5s5d\ {}^1D_2 \rightarrow 5s11f\ {}^1F_3 \rightarrow Sr^+$, Spectrochim. Acta. B 55 (2000) 1679–1692.

[124] V. Philipsen, J. Bastiaansen, G. Verschoren, P. Lievens, E. Vandeweert, R. E. Silverans, H. H. Telle, Double-resonant photoionization spectroscopy of Sr I, Spectrochimica Acta B 55 (2000) 1539–1550.

[125] H. G. C. Werij, C. H. Greene, C. E. Theodosiou, A. Gallagher, Oscillator strengths and radiative branching ratios in atomic Sr, Phys. Rev. A 46 (1992) 1248–1260.

[126] P. Esherick, Bound, even-parity J=0 and J=2 spectra of Sr, Phys. Rev. A 15 (1977) 1920–1936.

[127] M. Aymar, E. Luc-Koenig, S. Watanabe, R-matrix calculation of eigenchannel multichannel quantum defect parameters for strontium, J. Phys. B 20 (1987) 4325–4345.

[128] M. Madine, H. W. van der Hart, Single- and two-photon ionization of Sr, J. Phys. B 38 (2005) 1895–1905.

[129] S. Sayama, M. Ohtsu, Tunable UV CW generation by frequency tripling of a Ti:Sapphire laser, Opt. Commun. 137 (1997) 295–298.

[130] H. Schnitzler, U. Fröhlich, T. K. W. Boley, A. E. M. Clemen, J. Mlynek, A. Peters, S. Schiller, All-solid-state tunable continuous-wave ultraviolet source with high spectral purity and frequency stability, Appl. Opt. 41 (2002) 7000–7005.

[131] S. Sayama, M. Ohtsu, Tunable UV CW generation at 276 nm wavelength by frequency conversion of laser diodes, Opt. Commun. 145 (1998) 95–97.

[132] J. Franzke, R. W. Fox, L. Hollberg, Tunable UV generation at 283 nm by frequency doubling and sum frequency mixing of two semiconductor lasers for the detection of Pb, Spectrochimica Acta B 53 (1998) 1951–1955.

[133] M. L. Boas, Mathematical methods in the physical sciences, 2nd Edition, John Wiley & Sons, New York, 1983.

[134] A. N. Nesmeyanov, Vapour pressure of the elements, Infosearch, London, 1963, trans. J. I. Carasso.

[135] H. Rohde, S. T. Gulde, C. F. Roos, P. A. Barton, D. Leibfried, J. Eschner, F. Schmidt-Kaler, R. Blatt, Sympathetic ground-state cooling and coherent manipulation with two-ion crystals, J. Opt. B 3 (2001) S34–S41.

[136] B. B. Blinov, D. Leibfried, C. Monroe, D. J. Wineland, Quantum computing with trapped ion hyperfine qubits, Quant. Inf. Proc. 3 (2004) 45–59.

[137] A. Mortensen, J. J. T. Lindballe, I. S. Jensen, P. Staanum, D. Voigt, M. Drewsen, Isotope shifts of the $4s^2\ {}^1S_0 \rightarrow 4s5p\ {}^1P_1$ transition and hyperfine splitting of the $4s5p\ {}^1P_1$ state in calcium, Phys. Rev. A 69 (2004) 042502–042507.

[138] J. Ye, JILA, University of ColoradoPersonal Communication.

[139] X. Xu, T. H. Loftus, J. L. Hall, A. Gallagher, J. Ye, Cooling and trapping of atomic strontium, J. Opt. Soc. Am. B 20 (2003) 968–976.

[140] D. J. Wineland, Ion trap approaches to quantum information processing and quantum computing: a quantum information science and technology roadmapV 2.0 http://qist.lanl.gov/pdfs/ion_trap.pdf (2004).

[141] E. Peik, J. Abel, T. Becker, J. von Zanthier, H. Walther, Sideband cooling of ions in radio-frequency traps, Phys. Rev. A 60 (1999) 439–449.

[142] C. Monroe, D. M. Meekhof, B. E. King, S. R. Jefferts, W. M. Itano, D. J. Wineland, P. Gould, Resolved-sideband Raman cooling of a bound atom to the 3D zero-point energy, Phys. Rev. Lett. 75 (1995) 4011–4014.

[143] C. F. Roos, D. Leibfried, A. Mundt, F. Schmidt-Kaler, J. Eschner, R. Blatt, Experimental demonstration of ground state laser cooling with electromagnetically induced transparency, Phys. Rev. Lett. 85 (2000) 5547–5550.

[144] B. E. King, C. S. Wood, C. J. Myatt, Q. A. Turchette, D. Leibfried, W. M. Itano, C. Monroe, D. J. Wineland, Cooling the collective motion of trapped ions to initialize a quantum register, Phys. Rev. Lett. 81 (1998) 1525–1528.

[145] D. F. V. James, Quantum dynamics of cold trapped ions with application to quantum computation, Appl. Phys. B 66 (1998) 181–190.

[146] G. P. Barwood, C. S. Edwards, P. Gill, H. A. Klein, W. R. C. Rowley, Observation of the 5s $^2S_{1/2}$–4d $^2D_{5/2}$ transition in a single laser-cooled trapped Sr^+ ion by using an all-solid-state system of lasers, Opt. Lett. 18 (1993) 732–734.

[147] I. I. Rabi, S. Millman, P. Kusch, J. R. Zacharias, The molecular beam resonance method for measuring nuclear magnetic moments, Phys. Rev. 55 (1939) 526–535.

[148] R. J. Hughes, D. F. V. James, E. H. Knill, R. Laflamme, A. G. Petschek, Decoherence bounds on quantum computation with trapped ions, Phys. Rev. Lett. 77 (1996) 3240–3243.

[149] D. Leibfried, E. Knill, C. Ospelkaus, D. J. Wineland, Transport quantum logic gates for trapped ions, Preprint quant-ph/0707.3646 v2 (2007).

[150] D. Wineland, C. Monroe, R. Blatt, A. Steane, Specifications for a "test ion trap" for ion qubit manipulationhttp:// www.nbc.gov/ acquisition/ fort_h/ documents/ pdfs/ trap_specifications_v3.pdf (2004).

[151] B. Brkić, S. Taylor, J. F. Ralph, N. France, High-fidelity simulations of ion trajectories in miniature ion traps using the boundary-element method, Phys. Rev. A 73 (2006) 012326–012331.

[152] F. Splatt, University of Innsbruck.Personal Communication.

[153] R. Reichle, University of Ulm.Personal Communication.

[154] R. Reichle, D. Leibfried, R. B. Blakestad, J. Britton, J. D. Jost, E. Knill, C. Langer, R. Ozeri, S. Seidelin, D. J. Wineland, Transport dynamics of single ions in segmented microstructured Paul trap arrays, Fortschr. Phys 54 (2006) 666–685.

[155] T. Schaetz, M. D. Barrett, D. Leibfried, J. Chiaverini, J. Britton, W. M. Itano, J. D. Jost, C. Langer, D. J. Wineland, Quantum dense coding with atomic qubits, Phys. Rev. Lett. 93 (2004) 040505–040508.

[156] W. K. Hensinger, D. Stick, J. Sterk, M. Madsen, W. Noonan, M. Pedersen, S. Gross, M. Huff, C. Monroe, MEMS fabrication of silicon ion trap arrays, in: Workshop on Trapped Ion Quantum Computing, Boulder, 2006, http://tf.nist.gov/ion/workshop2006/t11.pdf.

[157] S. Pau, C. S. Pai, Y. L. Low, J. Moxom, P. T. A. Reilly, W. B. Whitten, J. M. Ramsey, Microfabricated quadrupole ion trap for mass spectrometer applications, Phys. Rev. Lett. 96 (2006) 120801–120804.

[158] G. W. C. Kaye, T. H. Laby, Tables of Physical and Chemical Constants, Longman, Harlow, 1995.

[159] H. C. Miller, Surface flashover of insulators, IEEE Trans. Electr. Insul. 24 (1989) 765–786.

[160] A. M. Blackburn, D. G. Hasko, H. Ahmed, D. A. Williams, Tungsten pedestal structure for nanotriode devices, J. Vac. Sci. Technol. B 22 (2004) 1298–1302.

[161] A. Gerhard, M. Kurz, J. Brutscher, H. Klein, A. Schempp, RF sparking experiments at 108.5 and 216 MHz, IEEE Trans. Electr. Insul. 24 (1989) 1033–1036.

[162] S. Timoshenko, Vibration Problems in Engineering, 3rd Edition, D. Van Nostrand Co. Inc., New York, 1955.

[163] R. Lifshitz, M. L. Roukes, Thermoelastic damping in micro- and nanomechanical systems, Phys. Rev. B 61 (2000) 5600–5609.

[164] S. Timoshenko, Strength of Materials : Part I, 3rd Edition, D. Van Nostrand Co. Inc., New York, 1955.

[165] R. Slusher, Scalable planar trapology, in: Workshop on Trapped Ion Quantum Computing, Boulder, 2006, http://tf.nist.gov/ion/workshop2006/slusher1.pdf.

[166] M. G. Blain, L. S. Riter, D. Cruz, D. E. Austin, G. Wu, W. R. Plass, R. G. Cooks, Towards the hand-held mass spectrometer: design considerations, simulation, and fabrication of micrometer-scaled cylindrical ion traps, Int. J. Mass Spec. 236 (2004) 91–104.

[167] D. Cruz, J. P. Chang, M. G. Blain, Field emission characteristics of a tungsten microelectromechanical system device, Appl. Phys. Lett. 86 (2005) 153502–153504.

[168] M. G. Blain, C. P. Tigges, B. Jokiel, D. J. Berkeland, M. Boshier, MEMS-based ion trap chips: microfabrication and packaging consider-

ations, in: Workshop on Trapped Ion Quantum Computing, Boulder, 2006, http://tf.nist.gov/ion/workshop2006/blain.pdf.

[169] G. T. A. Kovacs, N. I. Maluf, K. E. Petersen, Bulk micromachining of silicon, Proceedings of the IEEE (86) 1536–1555.

[170] M. J. Madou, Fundamentals of Microfabrication: the science of miniaturization, 2nd Edition, CRC Press, Boca Raton, FL, 2002.

[171] D. C. Flanders, X-ray lithography at ∼100 angstrom linewidths using x-ray masks fabricated by shadowing techniques, J. Vac. Sci. Technol. 16 (1979) 1615–1619.

[172] Z. Yu, S. Y. Chou, Triangular profile imprint molds in nanograting fabrication, Nano Letters 4 (2004) 341–344.

[173] K. Robbie, J. C. Sit, M. J. Brett, Advanced techniques for glancing angle deposition, J. Vac. Sci. Technol. B 16 (1998) 1115–1122.

[174] R. B. Bosch GmbhUS Pat. 4855017, US Pat. 4784720 and Germany Pat. 4241045C1, 1994.